Fiber-Optic Distributed Sensing: From Advancing Turbulent Flow Measurement through Experimental and Numerical Simulation to Applications in Forest Micrometeorology

DISSERTATION

for the attainment of the academic degree of
Doctor of Natural Sciences (Dr. rer. nat.)
at the Bayreuth Graduate School of Mathematical and Natural Sciences (BayNAT)
of the University of Bayreuth

submitted by

Mohammad Abdoli

from *Ardebil, Iran*

Bayreuth, 2025

This doctoral thesis was prepared at the department of Micrometeorology at the University of Bayreuth from 01/2020 until 12/2025 and was supervised by Prof. Dr. Christoph K. Thomas. This doctoral thesis was conducted as part of the DarkMix project and was funded by the European Research Council (ERC) under the European Union's Horizon 2020 Research and Innovation Programme (Grant Agreement No. 724629).

This is a full reprint of the thesis submitted to obtain the academic degree of Doctor of Natural Sciences (Dr. rer. nat.) and approved by the Bayreuth Graduate School of Mathematical and Natural Sciences (BayNAT) of the University of Bayreuth.

Form of the Dissertation: Cumulative dissertation

Dissertation submitted on: 05.12.2025

Approval by the executive committee: 10.12.2025

Scientific colloquium: 20.04.2026

Acting director: Prof. Dr. Jürgen Senker

Doctoral committee:

Prof. Dr. Christoph Thomas (reviewer)

Prof. Dr. Efstathios Diamantopoulos (reviewer)

Prof. Dr. Cyrus Samimi (chair)

JProf. Dr. Lisa Hülsmann

Acknowledgements

- First and foremost, I would like to express my deepest gratitude to Prof. Dr. Christoph Thomas for his invaluable support, guidance, and mentorship throughout my doctoral journey. His influence helped me transition from an engineering mindset to a more critical and scientific way of thinking. I am especially thankful for the rich scientific and technical knowledge he shared with me in the fields of Micrometeorology and Boundary Layer Meteorology. Beyond the academic sphere, his unwavering support for both me and my family. I would also like to extend my heartfelt thanks to Gesa Thomas, whose kindness and practical support upon our arrival in Germany greatly helped us settle in. Her assistance around the time of our daughter's birth was especially meaningful and deeply appreciated.

- To my wife, Solmaz, thank you for your constant encouragement, patience, and unwavering belief in me throughout this journey. Your love and support have been my anchor. To my daughter, Ana, your smiles and presence have brought joy and motivation to every step of this path.

- I am equally grateful to my parents, who, despite the physical distance and the limitations on travel, have provided constant emotional support. Their belief in me has been a source of strength.

- My sincere thanks also go to my colleagues and friends Dr. Wolfgang Babel, Johann Schneider, Johannes Olesch, Elena Nizler, and Dr. Karl Lapo, for their scientific and technical support, as well as their help during field experiments.

Table of Contents

List of Publications

This is a list of all publications related to my Ph.D. work.

Already published:

- **Abdoli, M**., Lapo, K., Schneider, J., Olesch, J., Thomas, C.K., 2023. Toward quantifying turbulent vertical airflow and sensible heat flux in tall forest canopies using fiber-optic distributed temperature sensing. Atmospheric Meas. Tech. 16, 809–824.

- **Abdoli, M**., Pirkhoshghiyafeh, R., & Thomas, C. K. (2025). Improving turbulent airflow direction measurements for fiber-optic distributed sensing using numerical simulations. Atmospheric Measurement Techniques, 18(21), 6417-6433.

Submitted (under review):

- **Abdoli, M**., Lapo, K., & Thomas, C. K. (2025). Dynamic stability and canopy structure drive Spatio-Temporal Variability of Greenhouse Gases in the sub-canopy of a Temperate Spruce Forest. Submitted to Agricultural and Forest Meteorology (manuscript number: AGRFORMET-D-25-02734).

Summary

Turbulence is the principal mechanism governing the exchange and mixing of energy and matter in the atmospheric boundary layer (ABL), with implications ranging from leaf-scale processes to continental-scale interactions. While turbulence under strong winds and significant radiative forcing is well characterized, conditions under weak winds and stable stratification remain poorly understood, as they deviate from established theories such as Monin–Obukhov similarity, the Kolmogorov energy cascade, and Taylor's frozen turbulence hypothesis. Weak-wind regimes, which are particularly prevalent in forested environments, require high-resolution spatial data to resolve the underlying physical processes. This PhD research addresses these gaps by advancing fiber-optic distributed sensing (FODS) techniques through a combination of experimental, numerical, and machine learning approaches. The work contributes to the conceptual and methodological advancement of boundary-layer meteorology by investigating the weak and intermittent turbulence, ultimately improving our understanding of energy and matter exchange under weak-wind and stable conditions.

In the first part of this study, a novel FODS measurement technique (microstructure approach) was extended to enable the quantification of vertical turbulent wind and sensible heat flux. This approach uses directional temperature differences in a pair of fiber-optic (FO) cables with printed cone-shaped microstructures on them to determine wind direction and speed along the fiber. A key experimental innovation involved the use of cylindrical shrouds surrounding heated fiber-optic cables to suppress dominant horizontal wind speed fluctuations while preserving vertical turbulent signals. Among the tested configurations, a white cylindrical shroud with a 0.6 m diameter and rigid support structure exhibited optimal performance, reducing horizontal wind speed standard deviation by 35% without substantially attenuating vertical turbulence. Following optimization at ecological botanical garden (EBG) of the Bayreuth University, the method was deployed in the sub-canopy of a temperate forest to evaluate its effectiveness under natural weak-wind conditions. These measurements revealed coherent structures with clearly defined sweep and ejection phases, allowing for the detection of vertical turbulent airflow in over 60% of the data, increasing to 71% with conditional sampling. Importantly, this setup enabled the first direct estimation of sensible heat fluxes using FODS measurements, a methodological and computational advancement.

The results of the first part of the thesis showed potential for improving and optimizing the microstructure approach. The second part of the thesis focuses on optimizing the microstructure geometry of FO cables to improve directional sensitivity and thermal response in turbulent flow measurements. Through extensive numerical simulations using COMSOL Multiphysics 6.0, a wider range of filled and hollow coned microstructures were evaluated for their impact on temperature differences (ΔT) generated by electrically heated FO cables exposed to turbulent airflows. The hollow-cone design with a radius and height of 24 mm and 15 mm spacing was identified as the optimal configuration, outperforming filled cones by sustaining larger ΔT values (>2 K) across varying wind speeds and turbulence intensities. Notably, this design maintained ΔT of approximately 0.8 K even at 60° wind attack angles, underscoring its robustness for directional sensing. The findings highlight significant potential for improving FO cable design in atmospheric boundary layer research, enabling more accurate measurements of wind direction, vertical wind speed perturbations, and spatially distributed

turbulent heat fluxes using FODS. Future work shall validate the findings under field conditions to assess the robustness and real-world applicability of the optimized design.

The third part of the research integrates FODS measurement technology into micrometeorological and biogeochemical studies of forests, focusing on the spatial and temporal variability of greenhouse gas mixing ratios (CO_2, CH_4, and H_2O) in the sub-canopy. This is achieved by combining dense, high-resolution FODS arrays with complementary gas sampling network. To this end, we characterized wind regimes by sub- and above-canopy turbulence metrics. These metrics were used to differentiate between weak- and strong-wind conditions, which distinctly affect scalar gas variability. Using Random Forest modeling, turbulence-related variables including turbulent kinetic energy, vertical wind fluctuations, and dynamic stability were identified as primary drivers of scalar variability during strong-wind regimes, while temperature dominated the spatial variabilities under weak-wind conditions. CO_2 variability under strong-wind conditions correlated strongly with vertical wind and dynamic stability, whereas CH_4 was influenced by temperature consistently. H_2O spatial variability was tightly coupled to temperature across regimes, reflecting effect of evapotranspiration dynamics in forest. Clustering of vertical potential temperature profiles from FODS using k-means algorithms classified thermal stratification regimes, showing unstable profiles enhance mixing and reduce scalar gradients, while stable stratification suppresses mixing and intensifies gradients. The potential temperature profile thus effectively integrated the influence of both turbulence and radiative processes on scalar mixing.

Overall, this PhD research delivers a comprehensive advancement in fiber-optic distributed sensing technology and its application to forest sub-canopy micrometeorology. By combining experimental innovations, rigorous numerical modeling, and machine learning analyses, it enhances the capability to observe fine-scale turbulence, heat fluxes, and scalar gas dynamics with unprecedented spatial and temporal resolution. These contributions provide new tools and insights for atmospheric science, ecosystem monitoring, and climate research.

Zusammenfassung

Turbulenz ist der zentrale Mechanismus für den Austausch und die Durchmischung von Energie und Materie in der atmosphärischen Grenzschicht (Atmospheric Boundary Layer, ABL) und beeinflusst Prozesse von der Blatt- bis zur Kontinentalebene. Während Turbulenz unter starkem Wind und ausgeprägtem Strahlungsantrieb gut beschrieben ist, bleiben Situationen mit schwachem Wind und stabiler Schichtung weitgehend unzureichend verstanden, da sie von etablierten Theorien wie der Monin–Obukhov-Ähnlichkeitstheorie, der Kolmogorow-Energiekaskade und Taylors Hypothese gefrorener Turbulenz abweichen. Schwachwindregime, die insbesondere in Waldökosystemen häufig auftreten, erfordern hochaufgelöste räumliche Messdaten, um die zugrunde liegenden physikalischen Prozesse zu erfassen. Diese Dissertation adressiert diese Forschungslücken durch die Weiterentwicklung faseroptischer, verteilter Messtechniken (Fiber-Optic Distributed Sensing, FODS) mittels experimenteller, numerischer und datengetriebener Ansätze einschließlich maschinellen Lernens. Die Arbeit leistet einen konzeptionellen und methodischen Beitrag zur Meteorologie der Grenzschicht, indem sie schwache und intermittierende Turbulenz charakterisiert und so das Verständnis von Energie- und Stoffaustausch unter stabilen Schwachwindbedingungen verbessert.

Im ersten Teil dieser Arbeit wurde ein neuartiger FODS-Ansatz (Microstructure Approach) erweitert, um die Quantifizierung vertikaler turbulenter Wind- und fühlbarer Wärmeflüsse zu ermöglichen. Dabei werden gerichtete Temperaturdifferenzen zwischen einem Paar faseroptischer (FO) Kabel mit aufgedruckten, kegelförmigen Mikrostrukturen genutzt, um Windrichtung und -geschwindigkeit entlang der Faser zu bestimmen. Eine zentrale experimentelle Innovation war der Einsatz zylindrischer Ummantelungen um beheizte FO-Kabel, um dominante horizontale Windgeschwindigkeitsschwankungen zu dämpfen und gleichzeitig vertikale Turbulenzsignale zu erhalten. Unter den getesteten Konfigurationen zeigte sich eine weiße zylindrische Ummantelung mit 0,6 m Durchmesser und starrer Halterung als optimal: Sie reduzierte die Standardabweichung der horizontalen Windgeschwindigkeit um 35 %, ohne die vertikale Turbulenzsignatur wesentlich zu beeinflussen. Nach erfolgreicher Optimierung im Ökologisch-Botanischen Garten (EBG) der Universität Bayreuth wurde die Methode im Unterwuchs eines Nadelwaldes getestet, um ihre Eignung unter natürlichen Schwachwindbedingungen zu evaluieren. Die Messungen zeigten kohärente Strukturen mit klar ausgeprägten Sweep- und Ejektionsphasen. Vertikale turbulente Luftbewegungen konnten in über 60 % der Daten detektiert werden – mit bedingtem Sampling sogar in 71 %. Besonders hervorzuheben ist, dass mit diesem Aufbau erstmals eine direkte Bestimmung fühlbarer Wärmeflüsse aus FODS-Messungen möglich war, was einen methodischen und rechnerischen Fortschritt darstellt.

Die Ergebnisse des ersten Teils verdeutlichen das Potenzial zur weiteren Verbesserung des Microstructure Approach. Der zweite Teil der Arbeit konzentriert sich auf die Optimierung der Mikrostrukturgeometrie von FO-Kabeln, um deren Richtungsempfindlichkeit und thermisches Ansprechverhalten in turbulenten Strömungen zu verbessern. Umfangreiche numerische Simulationen mit COMSOL Multiphysics 6.0 wurden durchgeführt, um verschiedene gefüllte und hohle Kegeldesigns hinsichtlich der erzeugten Temperaturdifferenzen (ΔT) zu analysieren, die durch elektrisch beheizte Kabel im turbulenten Luftstrom entstehen. Die hohle Kegelkonstruktion mit einem Radius und Höhe von 24 mm und einem Abstand von 15 mm erwies sich als optimal, da sie über ein breites Spektrum an Windgeschwindigkeiten und Turbulenzintensitäten hinweg ΔT-Werte von über 2 K aufrechterhielt. Auch bei Anströmwinkeln bis zu 60° zeigte diese Konfiguration stabile Temperaturdifferenzen von etwa 0,8 K und damit eine hohe Robustheit für

Richtungsmessungen. Diese Ergebnisse verdeutlichen das große Potenzial zur Verbesserung faseroptischer Messsysteme in der Grenzschichtmeteorologie, insbesondere für präzisere Erfassungen von Windrichtung, vertikalen Windfluktuationen und turbulenten Wärmeflüssen mit FODS. Zukünftige Arbeiten sollten diese optimierte Geometrie unter Feldbedingungen validieren, um ihre Anwendbarkeit und Robustheit zu überprüfen.

Der dritte Teil der Dissertation integriert die FODS-Messtechnik in mikrometeorologische und biogeochemische Untersuchungen von Wäldern und konzentriert sich auf die räumliche und zeitliche Variabilität der Mischungsverhältnisse von Treibhausgasen (CO_2, CH_4 und H_2O) im Unterwuchs. Hierzu wurden dichte, hochaufgelöste FODS-Arrays mit einem ergänzenden Gasprobennetzwerk kombiniert. Zur Charakterisierung der atmosphärischen Bedingungen wurden Windregime anhand turbulenter Kennwerte ober- und unterhalb des Kronendachs definiert. Diese Metriken dienten zur Unterscheidung zwischen Schwach- und Starkwindbedingungen, die sich deutlich auf die Variabilität der Skalarkonzentrationen auswirken. Mithilfe von Random-Forest-Modellen wurden turbulenzbezogene Variablen wie turbulente kinetische Energie, vertikale Windfluktuationen und dynamische Stabilität als Haupttreiber der Skalarvariabilität unter Starkwindbedingungen identifiziert, während bei Schwachwindbedingungen die Temperatur dominierte. Die CO_2-Variabilität korrelierte unter stark turbulenten Bedingungen stark mit der vertikalen Windgeschwindigkeit und dynamische Stabilität, während CH_4 überwiegend durch die Temperatur beeinflusst wurde. Die H_2O-Variabilität war in allen Regimen eng mit der Temperatur gekoppelt, was den Einfluss der Evapotranspiration widerspiegelt. Durch Clustering vertikaler Temperaturprofile aus den FODS-Daten mittels k-means-Algorithmus konnten atmosphärische Stratifizierungsregime identifiziert werden: Instabile Profile förderten die Durchmischung und reduzierten Skalargradienten, während stabile Schichtung die Durchmischung hemmte und Gradienten verstärkte. Das vertikale Temperaturprofil erwies sich somit als integraler Indikator für das Zusammenspiel von Turbulenz und Strahlungsprozessen bei der Skalarmischung.

Insgesamt liefert diese Dissertation einen umfassenden Beitrag zur Weiterentwicklung der FODS-Technologie und ihrer Anwendung in der Mikrometeorologie bewaldeter Grenzschichten. Durch die Kombination experimenteller Innovationen, numerischer Modellierung und datengetriebener Analysen mittels maschinellen Lernens werden neue Möglichkeiten geschaffen, Turbulenz, Wärmeflüsse und Skalarkonzentrationen mit bisher unerreichter räumlicher und zeitlicher Auflösung zu erfassen. Diese Erkenntnisse liefern wertvolle Grundlagen für die Atmosphärenwissenschaft, das Ökosystemmonitoring und die Klimaforschung.

Chapter One

Synopsis

1.1 General Introduction

From a micrometeorological perspective, turbulence refers to the irregular, fluctuating component of air motion, superimposed on the mean flow, that serves as the dominant mechanism for mixing energy and matter in the atmosphere and plays a central role in regulating vertical exchange processes of momentum, heat, moisture, and trace gases between the Earth's surface and the atmosphere (Burgers, 1948; Stull, 1988; Tennekes and Lumley, 1972). Representation of the atmospheric boundary layer (ABL) is crucial for the reliability of weather and climate models, as it encompasses key processes such as the transport and mixing of radiation, sensible and latent heat, water vapor, carbon dioxide, and nutrients that directly influence ecosystem functioning and the well-being of plants, animals, and humans (Holtslag et al., 2013; Ren et al., 2025). While the dynamics of turbulent transport near the surface under sufficiently strong wind conditions and significant solar heating or radiative cooling are relatively well captured by existing theoretical frameworks (Mahrt, 2014; Van de Wiel et al., 2012), including Monin-Obukhov Similarity Theory (Monin and Obukhov, 1954), the Kolmogorov energy spectrum (Frisch and Kolmogorov, 1995), and Taylor's hypothesis of frozen turbulence (Taylor, 1938), these assumptions often break down under stably stratified and weak-wind conditions, posing substantial challenges for both theoretical understanding and numerical modeling (Chowdhuri et al., 2025; Grachev et al., 2013; LeMone et al., 2019; Mahrt et al., 2013; Sun et al., 2012; Van de Wiel et al., 2012).

1.1.1 Challenges in Weak-Wind and Stably Stratified Boundary Layers (SBL)

Stably stratified boundary layers play a crucial role in both atmospheric research and practical applications. They frequently coincide with long-lasting air pollution events and remain a persistent source of error in numerical weather prediction (NWP) systems, especially when forecasting fog, icing, or similar boundary-layer phenomena. Yet, despite their importance, SBLs continue to challenge theoretical understanding, observational methods, and numerical modelling (Sandu et al., 2013). Such strongly stable regimes give rise to a wide variety of realizations that defy simple classification (Stiperski et al., 2025). Under stably stratified weak-wind conditions, turbulence is not solely governed by dynamic stability or buoyancy forcing but is also influenced by a complex interplay of non-stationary processes, sub-mesoscale motions, local shear, and flow instabilities

(Liang et al., 2014; Mahrt et al., 2013). These conditions often give rise to intermittent turbulence, which challenges the validity of fundamental assumptions underlying micrometeorological theories and statistical approaches. For instance, the translation of temporal into spatial scales through Taylor's hypothesis of frozen turbulence becomes questionable, as does the assumption of ergodicity i.e., the convergence of time and spatial averages under stationary and horizontally homogeneous conditions (Engelmann and Bernhofer, 2016; Sun et al., 2012; Thomas, 2011). The complex non-linear interactions between the mean flow, sub-mesoscale motions, and turbulence in the SBL make it necessary to consider not only turbulence itself but also other small-scale processes, including radiation, advection, surface heterogeneity and associated transport, fog formation, and gravity waves. A deeper understanding and improved modeling of these processes, along with their non-linear interactions, are essential for capturing the full dynamics of the SBL.
In such regimes, single-point measurements fail to capture the spatial heterogeneity and transient structures inherent to intermittent flows (Mahrt and Vickers, 2003; Poulos and Burns, 2003). Several studies have attempted to address these challenges by employing sensor networks to investigate phenomena such as meandering flows and within-canopy transport of momentum and heat (Anfossi et al., 2005; Thomas, 2011). Nonetheless, despite notable progress, a lack of sufficiently dense spatial observations continues to limit our ability to resolve the relevant process scales and develop a comprehensive physical understanding of the stable boundary layer (Mahrt, 2010). Spatio-temporally continuous observational techniques, such as Distributed Temperature Sensing (DTS), provide a powerful tool to resolve these processes across scales and offer new opportunities to advance both theory and parameterization in numerical models (Thomas et al., 2012).

1.1.2 Transformative Potential of Fiber-Optic Distributed Sensing (FODS)

Fiber-Optic Distributed Sensing (FODS), particularly in the form of DTS has emerged in recent years as a transformative geophysical technique for overcoming the limitation of single point measurements by capturing the spatiotemporal dynamics of atmospheric and surface temperatures. DTS is a type of fiber-optic (FO) sensor that measures temperature continuously along defined sections of FO cables. It works by sending a laser pulse through the fiber, where most of the light is elastically scattered, while a small fraction undergoes inelastic Raman scattering. The resulting

backscatter consists of two components: Stokes, which is nearly temperature-independent, and Anti-Stokes, whose amplitude varies with temperature. By measuring the logarithmic ratio of Stokes to Anti-Stokes signals over defined cable sections using range-gating, DTS can spatially resolve temperature along the fiber (Thomas and Selker, 2021; Ukil et al., 2012). Since its development in the 1980s, DTS technology has advanced considerably, enabling continuous temperature measurements with resolutions as fine as 0.01°C and spatial resolutions down to a few meters or even decimeters. DTS has been applied across a wide range of fields, including structural health monitoring of dams (Bado, 2021), pipelines and tunnels (Ishii et al., 1997), offshore oil and gas installations, and mining (Silva et al., 2022).

In research contexts, DTS has been used for hydrological studies (Bense et al., 2016; Selker et al., 2006; Tyler et al., 2009), soil moisture measurements (Steele-Dunne et al., 2010), and atmospheric observations (de Jong et al., 2015; des Tombe et al., 2020; Fritz et al., 2021; Higgins et al., 2018; Kalantari et al., 2021; Keller et al., 2011; Thomas et al., 2012), typically for resolving temperature variations with height or along specific spatial dimensions in the atmospheric boundary layer. By converting standard telecommunication-grade FO cables into dense arrays of temperature sensors, DTS enables measurements with temporal resolutions of a few seconds and spatial resolutions on the order of tens of centimeters, along cable lengths extending up to 20 kilometers (Pfister et al., 2021a; Thomas et al., 2012).

Recent studies have highlighted the central role of FODS in advancing boundary-layer research. For example, Zeeman et al. (2015) used FODS to detect sharp temperature gradients and intermittent layering in the nocturnal boundary layer, while Pfister et al. (2021a, 2021b) identified semi-stationary thermal submesofronts using horizontal FODS configurations, and Mack et al. (2025) demonstrated the technique's robustness during airborne deployments under extreme Arctic conditions. FODS has proven to be a valuable tool during the morning transition period, as it is capable of capturing complex thermal and turbulent structures during the breakdown of nocturnal inversions (Fritz et al., 2021; Higgins et al., 2018). FODS has also been applied to quantify near-surface stratification and mixing in urban environments, including coastal cities (Karttunen et al., 2022). Recent work has also extended FODS-based observations to test and refine theoretical frameworks, such as the Monin–Obukhov Similarity Theory (MOST), particularly in the roughness sublayer where traditional formulations often break down (Boekee et al., 2024). Innovations in

high-resolution DTS instrumentation have made it possible to probe near-surface temperature profiles with millimeter-scale vertical resolution, offering new tools for evaluating surface flux gradients and turbulence closure schemes (ter Horst et al., 2025). In polar boundary-layer research, FODS has provided unprecedented detail on thermal stratification and turbulence regimes (Zeller et al., 2021), while Huss and Thomas, (2024) combined FODS with sonic anemometry to quantify vertical heat transport and surface–atmosphere coupling under strong stable stratification. FODS has also enabled new insights into weak-wind stable boundary-layer processes (Lapo et al., 2022) and the vertical structure of the stable boundary layer within forested canopies as a prone environment to weak-wind regimes (Peltola et al., 2022).

The development of wind speed measurement methods using FODS has significantly expanded the range of applications for this technology beyond temperature sensing. Notably, studies by Sayde et al. (2015) and van Ramshorst et al. (2020) demonstrated the feasibility of using FODS to continuously measure wind speed based on convective heat loss from actively heated FO cables. These advancements suggest that FODS can be used not only for scalar measurements but also to spatially resolve turbulent wind structures. Building on this foundation, the Darkmix project, initiated in 2019, aimed to develop a three-dimensional Large Eddy Observation (LEO) technique using DTS to investigate weak-wind and stable boundary-layer dynamics across diverse land uses, including grassland, forest, and urban areas (Lapo et al., 2022). Within the project, Lapo et al. (2020) introduced an innovative "microstructure approach" which combines Computational Fluid Dynamics (CFD) simulations with wind tunnel experiments to retrieve wind direction and speed from actively heated fibers equipped with imprinted filled-cone microstructures. The technique relies on convective heat loss: wind flowing along the orientation of the cones induces a different heat dissipation pattern than wind flowing against it, allowing the determination of flow direction. This method was successfully validated in a field experiment by Freundorfer et al. (2021), demonstrating wind direction measurements with an accuracy of ≤ 15.

Despite recent progress toward the development of fully three-dimensional, spatially resolving atmospheric flow sensors using FODS, significant limitations persist particularly in the measurement of vertical wind components. While horizontal wind direction and speed have been successfully retrieved, capturing the vertical wind component using heated coned FO cables remains challenging. Vertical wind fluctuations are generally of lower magnitude than the

horizontal mean flow, and in the current coned FO configuration, lateral wind effects dominate the heat loss signal. This results in a diminished temperature difference of the coned FO pairs, rendering the detection of vertical wind speed and direction ineffective. To address this limitation, we conducted a two-part study comprising both experimental and numerical approaches. In the first part (Abdoli et al., 2023), a series of field experiments were carried out to evaluate cylindrical shrouds with varying geometrical and physical properties such as aspect ratio, porosity, and rigidity in order to identify configurations capable of attenuating horizontal wind disturbances while preserving vertical flow structures. The optimal shroud design was subsequently applied in a forest sub-canopy environment, where coherent structures and mixing-layer dynamics are associated with relatively strong vertical motions. This setup was used to evaluate whether shrouded, heated coned FO cables could resolve vertical wind speed and direction and enable estimation of sensible heat fluxes based solely on FODS measurements. In the second part (Abdoli et al., 2025b), we complemented the fieldwork with a numerical investigation to optimize the microstructure geometry of the FO cable assembly. Using conjugate heat transfer simulations, we examined a range of filled- and hollow-coned configurations varying in radius, height, and spacing. The objective was to increase sensitivity to vertical airflow by enhancing the differential heat loss between upstream and downstream fiber orientations. These simulations aimed to improve the reliability and robustness of vertical wind measurements with FODS, particularly under weak-wind conditions typical of forest sub-canopy environments.

1.1.3 Forest Micrometeorology and FODS

Forest micrometeorology is the study of the physical processes governing the exchange of energy, mass, and momentum between forest ecosystems and the atmosphere (Baldocchi, 2020). Unlike open terrain, forested landscapes form a highly structured and vertically complex environment composed of the canopy crown, trunk space, and sub-canopy layers (Kaimal and Finnigan, 1994). These layers shape microclimatic conditions by altering radiative transfer, aerodynamic roughness, and turbulent mixing. Understanding these processes is essential for quantifying ecosystem functions such as evapotranspiration, heat flux partitioning, and ecosystem respiration, and for accurately representing the role of forests in the global carbon balance (Bonan, 2008; Luyssaert et al., 2007). Forests store nearly half of terrestrial carbon and regulate boundary-layer development,

making forest micrometeorology a key component of climate–ecosystem interactions and predictive Earth-system modeling (Pan et al., 2011).

The forest sub-canopy is of particular importance because it represents the interface where soil, vegetation, and atmospheric processes converge. Here, scalar exchange becomes highly sensitive to flow regime, thermal stratification, and canopy structure (Finnigan, 2000; Thomas, 2011). Flow within the sub-canopy diverges strongly from classical atmospheric boundary-layer behavior where the turbulence is suppressed by dense vegetation, local shear production is weak, and radiative cooling at night often produces strong static stability (Mahrt et al., 2015; Sun et al., 2012). Under these weak-wind, SBL conditions, many foundational assumptions such as Monin–Obukhov similarity theory, the Kolmogorov cascade, and Taylor's frozen-turbulence hypothesis frequently fail (Belcher et al., 2008; Mahrt et al., 2015). As a result, subcanopies experience intermittent turbulence, CO_2 accumulation, decoupled flow layers, and strong horizontal and vertical heterogeneity in scalar distributions (Feigenwinter et al., 2010). This complexity contributes to persistent uncertainties in energy-balance closure, nighttime carbon-dioxide fluxes, and the interpretation of eddy-covariance measurements in forest environments (Aubinet et al., 2010; Wilson and Meyers, 2001).

Recent advances in observational methods particularly FODS have provided a transformative approach to resolving these processes. FODS offers spatially continuous temperature measurements at centimeter-scale resolution, enabling the detection of fine thermal gradients, intermittent mixing events, canopy waves, and stability transitions that remain undetected by traditional point sensors (Selker et al., 2006; Tyler et al., 2009). Several studies have demonstrated the value of FODS for characterizing canopy–atmosphere interactions. Abdoli et al. (2023) showed how FODS resolves coherent structures in forest sub-canopy. Peltola et al. (2021) demonstrated the effectiveness of the FODS in monitoring atmospheric mixing profiles, highlighting its ability to capture continuous profiles of both turbulent fluctuations and mean air temperature values along the mast, thus offering valuable insights into mixing processes. Schilperoort et al. (2020) focused on capturing small-scale mixing variability and emphasized the potential of FODS to investigate dynamic thermal regimes within forest sub-canopies. Despite these advances, a significant knowledge gap persists. While FODS has enhanced our understanding of temperature structure and mixing dynamics, the relationship between observed spatial temperature gradients and the transport

and spatiotemporal variability of key scalar gases such as CO_2, CH_4, and H_2O within forest sub-canopies remains unclear. Since temperature influences density, buoyancy, and turbulence, there is a strong coupling with scalar fields (Thomas, 2011). However, this relationship has seldom been investigated through integrated canopy-scale observations.

The third paper in this dissertation addresses this gap by combining FODS-based temperature measurements with a distributed scalar-gas sampling network and machine-learning approaches. This integrated methodology enables a detailed assessment of how thermal stratification, mixing processes, and local flow regimes jointly influence the variability and transport of greenhouse gases in the forest sub-canopy. By linking high-resolution thermal structure with multi-scalar dynamics, this work advances forest micrometeorology and provides critical insights for improving ecosystem-flux interpretation and carbon-cycle modeling.

1.2 Materials and methods

This section provides a brief overview of the experimental setup, instrumentation, data acquisition techniques and analytical methods used in the three main phases of the study: the Shroud Optimization Experiment, the LOEWE20 Field Campaign, and numerical modeling.

1.2.1 Study Sites and Experimental Setup

The research was conducted at two distinct field sites: the Ecological Botanical Garden (EBG) for preliminary testing and the Waldstein forest for the main LOEWE20 campaign. The first phase of the study, conducted at EBG from April to June 2020, focused on optimizing the design of a cylindrical shroud aimed at isolating vertical wind component. The EBG, located at the University of Bayreuth, is characterized by short grass (5–15 cm) surrounded by mixed trees approximately 15 meters in height. For this phase, two sensor sets were deployed at a height of 1.5 meters one inside the shroud and one outside. Different cylindrical shrouds with variable diameters, lengths, colors, mesh sizes and levels of rigidity were tested to determine which would be the most promising to implement in the second part of the study. The second phase of the study, conducted at the Waldstein-Weidenbrunnen long-term ecosystem flux site (DE-Bay) as part of the LOEWE20 campaign, focused on assessing the effectiveness of the optimized shroud in preserving the vertical

wind speed and thus the temperature difference of coned FO cables within a forest environment. The shroud was installed at the main tower at the height of 3-6 m, encompassing a quartet FO array composed of two pairs of parallel coned and unconed FO cables extending from the ground to the canopy top at a height of 34 meters. Additionally, a sensor package was positioned outside the shroud, near the center of the cylinder as a reference. The LOEWE20 campaign took place from 10 September to 5 October 2020 in a Norway spruce forest with a canopy height of approximately 27 meters, an environment characterized by highly variable flow regimes. Figure 1 provides a graphical overview of the instrumentation and research site of LOEWE20 campaign.

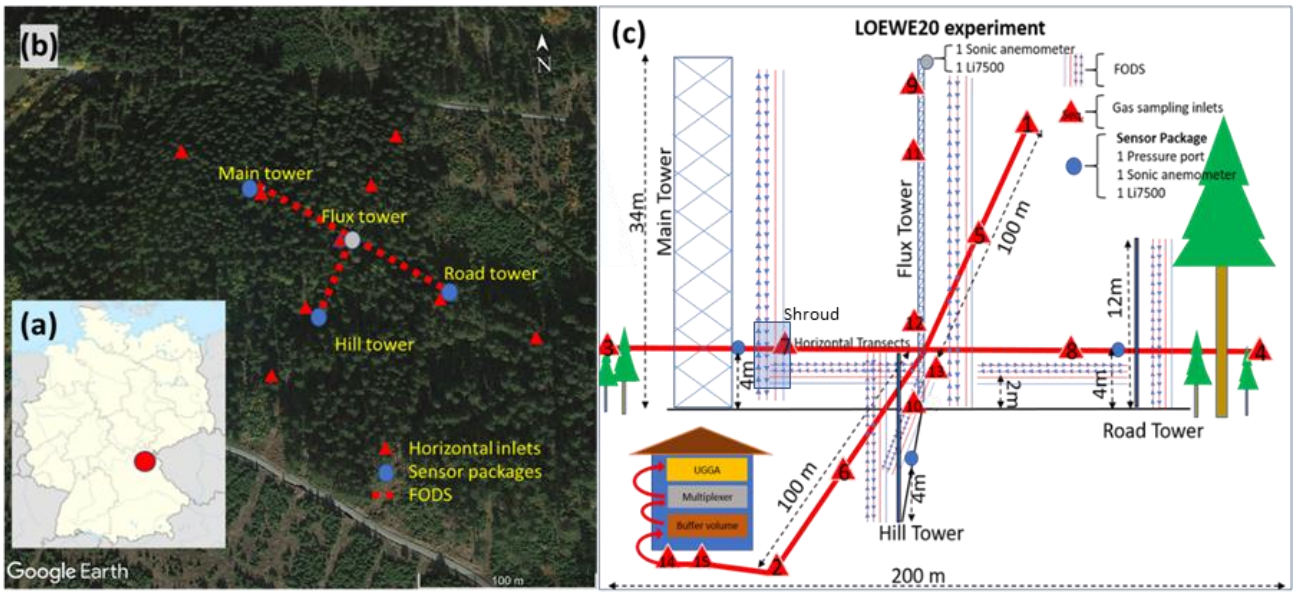

Figure 1. (a) Location of the LOEWE20 experiment marked with a red dot on the map of Germany. (b) Layout of the measurement network showing the FODS arrays as dashed red lines, the horizontal inlets of the Gas Mixing ratio Sampling Network (GCSN) as red triangles labelled S1–S8 and S12, and four vertical measurement towers with sensor packages indicated by blue solid points. (c) Detailed schematic of the experimental setup illustrating the vertical and horizontal FODS arrays, including two unconed fibers (one of which is heated) and two heated coned fibers, and the GCSN inlets in both vertical and horizontal configurations, along with the sensor packages placed at three positions at 4 m and one at 36 m height. UGGA refers to ultra-portable close-path greenhouse gas analyser. This figure is adopted from Abdoli et al. (2025a) .

Other than the shroud experiment, the experiment employed a comprehensive sensor network covering a 200 m × 200 m plot. Four sensor packages were deployed at different heights: one at the canopy top (36 meters) and three at sub-canopy levels (4 meters). Each package was equipped with a sonic anemometer (CSAT3, Campbell Scientific Inc.), a quad disk static pressure transducer

(Model 745-16B, Paroscientific, Inc.), and an open-path infrared CO_2/H_2O gas analyzer (Licor 7500). Data were sampled at 10 Hz (at 36 meters) and 20 Hz (at 4 meters), with turbulent fluxes computed using a standardized Eddy Covariance (EC) routine (Thomas et al., 2009) and a 10-minute perturbation and averaging timescale.

The FODS technique played a pivotal role in the LOEWE20 campaign, providing high-resolution, distributed measurements of temperature, wind speed, and wind direction. The FODS setup involved deploying a quartet FO array, consisting of two pairs of parallel coned and unconed FO cables that extended from the ground to the canopy top (34 m). One unconed and both coned fibers were actively heated at a power of 4 Wm-1. A high-resolution DTS instrument (Model 5 km Ultima, Silixa) was used, providing spatial resolution of 0.127 m and temporal resolution of 6 s. Calibration of the FODS system was carried out using a double-ended configuration via the pyfocs code (Lapo et al., 2020). In addition, the LOEWE20 campaign incorporated a Gas Concentration Sampling Network (GCSN) designed to measure scalar gas mixing ratios (CH_4, CO_2, H_2O) across the canopy. An ultra-portable close-path greenhouse gas analyzer (UGGA, Los Gatos Research Inc.) sampled air from 13 vertical and horizontal ambient air inlets via a multiplexer, with a 2.5-liter buffer volume. Each sampling sequence for the 13 inlets lasted 7 minutes, and the data were averaged over 10-minute intervals after discarding the first 15 seconds of each sequence to prevent cross-contamination. More detailed information about the instrumental setup can be found in the 'Materials and Methods' sections of Papers I and III, which are attached to this dissertation (chapter two).

1.2.2 Methods

This study employed several advanced methods to investigate canopy flow dynamics and scalar gas variability, as detailed in Papers I to III (chapter two). The microstructure approach used cone-shaped microstructures printed on FO cables to exploit directional differences in convective heat loss. Additionally, Quadrant Analysis with a hyperbolic threshold was applied to 20 Hz sonic anemometer data to compare FODS vertical wind signals with observational data. To analyze the spatial variability of scalar gases and their most important driving variables, the study also applied Random Forest (RF) modeling. This algorithm determined the importance of micrometeorological predictors (CO_2, CH_4, and H_2O variability) from the GCSN data. Separate models were trained for

different wind regimes and tower locations, with feature importance assessed using permutation methods. Furthermore, the k-means clustering algorithm was used to classify thermal stratification regimes based on FODS temperature profiles, helping to examine the influence of thermal stratification on scalar gas variability. Temperature data were adjusted to potential temperature to account for pressure effects, ensuring a more accurate representation of temperature gradients and their impact on gas mixing. Detailed explanations of these methods can be found in the 'Materials and Methods' sections of Papers I and III in chapter two.

1.2.3 Numerical Modeling

This study has also used COMSOL Multiphysics 6.0 to simulate and optimize the design of microstructures for FODS. The stationary simulation focused on Fluid Flow and Heat Transfer in Solids and Fluids, with the K-ε Turbulence Model selected for its computational efficiency in simulating turbulence. The computational domain was defined to house six microstructures, and initial test runs optimized their dimensions. Solid copper represented the FO cable core, while polyvinyl chloride (PVC) simulated the microstructures material. Ambient air and FO cable temperatures were set to 20 °C and 45 °C, respectively, creating a 25 K difference. Wind speed varied from 0 to 4.0 ms-1, with a turbulence intensity of 0.05.

The simulation proceeded in two stages: first, a 2D modeling phase tested 64 geometric combinations for both filled-coned and hollow-coned microstructures. This stage analyzed the temperature difference (ΔT) between forward- and backward-coned fibers, helping identify the best configurations based on maximum ΔT. In the second stage, the best performing configurations of both filled-coned and hollow-coned were tested for different turbulent intensities. Finally, 3D modeling of the optimized designs was performed, introducing an attacking angle to evaluate sensor performance in different wind attacking angles. Figure 2 shows the schematic of modeled FO cable. The simulation was validated with a mesh independence study, confirming minimal standard deviation in FO cable temperatures, ensuring the solution's reliability and accuracy for the extensive parametric sweep required to optimize the microstructure geometry. Paper II provides more details on the model configuration.

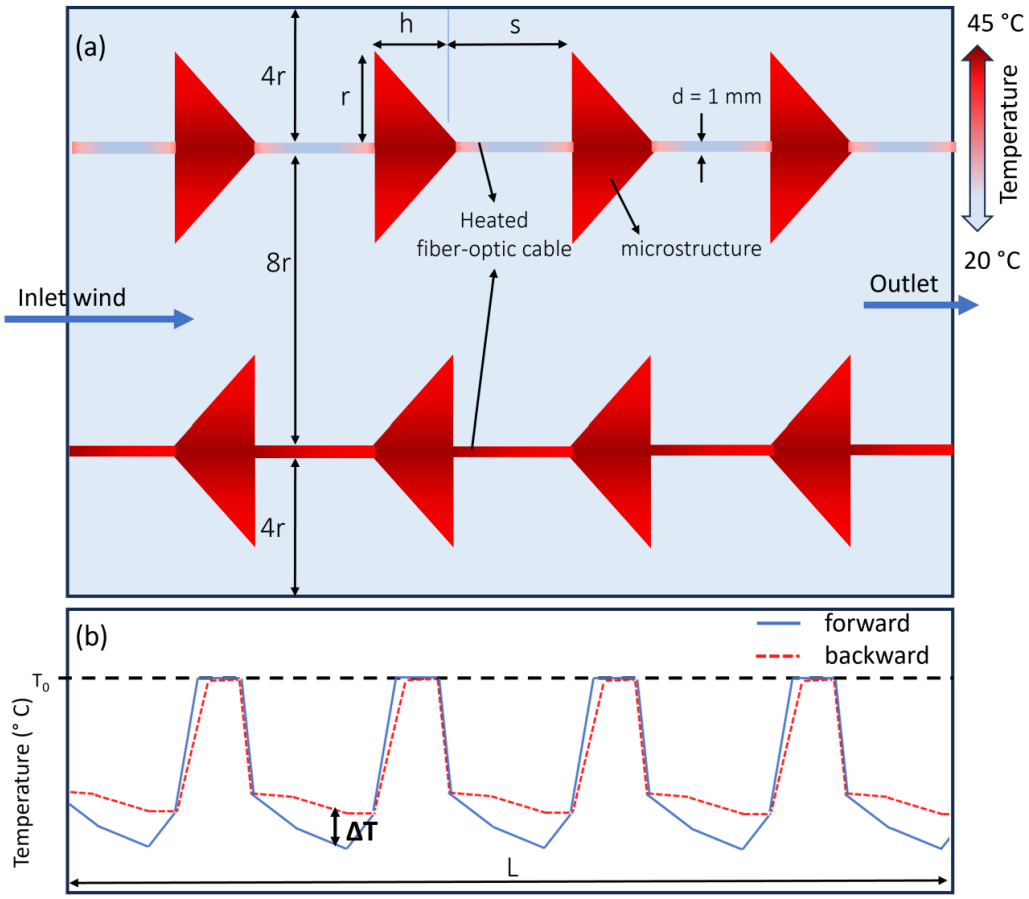

Figure 2. Schematic representing the modeled fiber optic cables featuring filled-coned microstructures. Panel (a) illustrates the surface temperature, ambient air temperature, and geometric parameters, while panel (b) depicts the conceptual temperature difference between the forward and backward fibers. Here, T_0 represents the temperature at the interface between the microstructure and the fiber optic cable. This schematic is adopted from Abdoli et al. (2025b) .

1.3 Synthesis of the Results

1.3.1 Advancing FODS Measurements in Micrometeorology

Turbulent exchange between the land surface and the atmosphere is a central process in micrometeorology, yet our understanding of these exchanges remains incomplete in weak-wind and stable conditions, where classical assumptions such as stationarity, homogeneity, and similarity theory often fail. New measurement approaches are therefore needed to resolve the intermittent, spatially variable motions that dominate these regimes. FODS offers the unique ability to capture temperature fields at high spatial resolution, and recent developments using heated and

microstructure-attached fibers have suggested that wind speed and direction can be inferred from the convective cooling of the cable. Extending this concept to detect vertical wind motions would represent a major step toward spatially distributed, three-dimensional turbulence measurements. With this motivation, we conducted a two-stage study: first, to identify whether a tubular shroud could adequately suppress horizontal wind while preserving vertical motions; and second, to test whether heated coned fibers could detect vertical wind signatures inside such a shroud within a forest subcanopy.

Our grassland experiment provided encouraging first evidence that shroud geometry can selectively attenuate parts of the horizontal wind while maintaining the essential behavior of the vertical turbulent component. Several shroud designs of varying diameter and porosity were evaluated using pairs of sonic anemometers inside and outside the shroud. The temporal evolution of vertical wind standard deviation showed a strong correspondence across all setups, indicating that the natural diurnal courses of convective and stable periods was retained even inside the shrouds. Setup 3, a 60-cm-diameter, white shroud with rigid supporting mesh, yielded the strongest agreement, with linear relationships between inside and outside standard deviation of vertical wind speed (σw) approaching highest correlation and smallest RMSE values among different setups. This shroud reduced horizontal wind magnitude by 35% while having minimal effect on vertical wind speed. Spectral analyses deepened this understanding: while energy in the largest eddies was reduced inside the shroud and the smallest high-frequency motions were strongly dampened, the inertial subrange remained preserved, retaining the $-5/3$ slope expected of isotropic turbulence. Change-point detection revealed that eddies with a duration shorter than roughly two to six seconds experienced the strongest attenuation.

Encouraged by these results, we transferred the optimized shroud concept to a structurally complex forest subcanopy during the LOEWE20 field campaign. Because the FODS sampling resolution imposes a minimum detectable temporal scale of approximately 30 seconds, we doubled the shroud length from 1.5 m to 3 m to ensure that sufficiently large and long-lived eddies could interact with the heated fiber. In the forest, we expected stronger, more coherent vertical motions due to persistent sweep-ejection cycles generated by canopy–mean flow interactions. However, once the experimental setup in forest was deployed, the shrouded heated coned fiber failed to reveal meaningful relationship between the temperature difference along the fiber and the sonic-measured

vertical wind speed. It became apparent that the flow inside the longer forest shroud behaved differently from that in the shorter grassland version. First, the increased length likely distorted or weakened vertical eddies before they reached the heated fiber. Second, even inside the shroud, horizontal wind speed did not consistently fall below the threshold required for vertical signatures to dominate the cooling pattern. Third, coherent structures weaken considerably below about 0.7 times canopy height, and at shroud height (approximately 3–6 m) the vertical motions were likely too weak to imprint a clear cooling pattern on the fiber. Thus, although the shroud performed well in the simpler grassland environment, it proved incompatible with the more complex flow conditions of a forest subcanopy.

Yet this setback unexpectedly led to the most important result of the study. In the unshrouded sections of the heated coned fibers where horizontal wind speeds naturally reached very low values (less than 0.2 ms-1), the temperature signals revealed remarkably clear signatures of coherent structures. Without any modification of the flow, the ΔT field showed alternating patterns corresponding to ejections and sweeps, aligning strongly with the vertical motions measured by the sonic anemometers. Correlations between ΔT and vertical wind reached moderate values across the entire deployment and rose significantly during periods of strong coupling, with rolling correlations exceeding 0.8. Under these favorable conditions, the coned fibers correctly identified the sign of vertical wind in over 60% of all samples.

Building on this insight, we established empirical relationships between ΔT and vertical wind using both linear and quadratic models. The latter was particularly well grounded in the physics of convective heat loss from a heated cylinder object and provided the best performance. These relationships allowed us to reconstruct spatially distributed vertical wind fields entirely from the FODS data. From these reconstructed fields, we computed sensible heat fluxes solely based on FODS measurements. The resulting flux estimates captured both the magnitude and temporal evolution of the sonic-derived sensible heat fluxes. This constitutes the first demonstration that FODS, even without mechanical flow modification, can independently provide spatially distributed estimates of sensible heat flux in a forest canopy.

Altogether, the study showed both the promise and limitations of using heated coned fibers to detect vertical wind motions. While shrouds helped simplifying the flow in open environments, they were not suitable for deployment in complex canopy flows. More importantly, the unexpected success

of the unshrouded fibers suggests a different path forward: instead of attempting to eliminate horizontal wind effects artificially, it may be more effective to optimize the microstructures. Earlier work introduced the microstructure approach (Lapo et al., 2020), where asymmetric conical structures printed onto paired heated fibers creating directional differences in cooling, enabling retrieval of wind direction and, under favorable weak-wind conditions, wind speed. In a follow-up study, we tested different geometrical configurations to optimize the microstructure approach. This study expanded on the original concept by systematically testing a much broader range of microstructure geometries, including cone radius, height and spacing, as well as whether the cones were hollow or filled, in order to improve directional heat loss, maximize the forward–backward temperature contrast and minimize undesirable sensitivity to cross-flow. To this end, we used COMSOL Multiphysics software to model the conjugate heat transfer in coned FO cables.

Numerical modeling in COMSOL provided detailed insight into the thermal and turbulent flow fields around the fiber. The simulations confirmed the core physical principle of the method: forward-facing cones always cool faster due to enhanced turbulent mixing, while backward-facing cones remain systematically warmer. For both filled and hollow cones, the backward fiber consistently maintained higher temperatures, but the hollow designs introduced an important improvement. Because only part of each hollow cone is attached to the fiber, more of the glass core is directly exposed to airflow. This reduces internal heat storage in the PVC material, shortens the thermal response time, and allows the temperature signal to be governed primarily by the external convection process rather than by the microstructure's own heat capacity.

Across 64 geometric combinations, the temperature difference (ΔT) between forward and backward fibers decreased non-linearly with increasing wind speed, consistent with earlier wind tunnel experiments. Yet the magnitude of ΔT depended strongly on microstructure geometry. Hollow-cone configurations produced ΔT values exceeding 7 K at 0.5 m s^{-1} substantially larger than any design previously tested while the best filled-cone geometries produced more moderate but still improved differences of 3–4 K. The optimal filled-cone combination (radius 18 mm, height 24 mm, spacing 20 mm) achieved a temperature contrast of 2.61 K between 0.5 and 4 m s^{-1} input wind speed and consistently outperformed the original designs of Lapo et al. (2020). For hollow cones, a geometry with radius and height both 24 mm and spacing of 15 mm showed the strongest performance, yielding ΔT values of 7.25 K at low wind speeds and 4.78 K across the 0.5–4 m s^{-1}

range. These signals are far above the measurement uncertainty of standard FODS systems and therefore provide a robust foundation for directional wind sensing.

The flow fields around the fibers revealed how the different geometries modify the turbulence itself. Filled-cone structures produced strong local reductions in turbulent kinetic energy and wind speed due to the thicker PVC material surrounding the fiber, whereas hollow structures allowed more direct interaction between the airflow and the heated core, resulting in smaller but more dynamically consistent perturbations in turbulent kinetic energy and wind speed. The highest temperature differences were not necessarily associated with the strongest turbulence distortions, particularly for filled cones, where heat conduction through the PVC still played a large role. These findings led to an important realization: cone aspect ratio alone is not a meaningful predictor of performance. Instead, total cone volume, coverage on the fiber, and the degree to which the microstructure regulates internal versus external heat transfer all strongly influence ΔT.

The most promising configurations were then tested across a range of turbulence intensities (TI), reflecting the highly variable and intermittent conditions in the atmospheric boundary layer. The filled-cone design maintained $\Delta T > 1$ K for TIs up to 0.2 and for wind speeds up to 2 m s^{-1} already sufficient for FODS detection and relevant for stable boundary layer conditions. However, the hollow-cone design performed substantially better, maintaining $\Delta T > 2$ K across all tested turbulence intensities and for wind speeds up to 4 m s^{-1}. Importantly, the sensitivity of ΔT to TI was much smaller for hollow cones, suggesting that this design offers more stable and reliable thermal signatures under realistic, fluctuating flow. The turbulence-induced variations in turbulent kinetic energy difference (ΔK) were also smaller for hollow cones, reinforcing the idea that hollow structures promote a more consistent convective heat-loss environment across a range of atmospheric conditions.

A final test examined the effect of wind attack angle, acknowledging that real wind rarely aligns perfectly with the cable. In full 3D simulations, the selected hollow-cone configuration retained a measurable ΔT even when winds struck the fiber obliquely. At attack angles up to 60°, the ΔT still reached ~0.8 K small but non-negligible and following a predictable decay pattern. This is a major improvement compared with earlier filled-cone designs, which lost directional sensitivity almost entirely under lateral winds. The hollow microstructures therefore fulfill a key requirement for

practical turbulence sensing: they reduce cross-flow distortion without eliminating the directional signal.

Together, these results show that microstructure geometry exerts far more influence over FODS directional sensing than previously recognized. By tuning cone volume, exposure length, spacing, and hollow versus filled design, it was possible to dramatically increase the magnitude, stability, and wind-speed range of the thermal signal used to infer airflow direction and speed. The best-performing hollow cones not only generate high ΔT across a wide range of flow conditions but also remain functional under cross winds and variable turbulence intensities. These improvements substantially strengthen the prospect of using FODS-based microstructure sensing for distributed wind direction and speed retrieval and, ultimately, for estimating turbulent heat fluxes across extended fiber networks in the stable boundary layer. The method now appears considerably more robust than the initial proof-of-concept and is well positioned for real-world deployment in weak-wind environments. The modeling presented here already indicates that appropriately optimized microstructure geometries can transform the capability of fiber-optic systems to map turbulent flows, offering a practical path toward distributed 3D turbulence sensing in atmospheric research.

However, the outcomes and optimized designs for FODS-based wind direction and wind speed measurement developed in the first two papers (Paper I and Paper II in chapter two) could not be tested in real-world condition due to time limitations of the project. Nevertheless, the extensive spatiotemporal FODS dataset collected during the LOEWE20 campaign combined with the greenhouse gas measurement network and the eddy-covariance stations provided a unique opportunity to pursue both measurement-technology improvements and implications of FODS for open research questions within the forest micrometeorology research. Building on these complementary datasets, we used the distributed FODS temperature measurements together with the greenhouse gas monitoring network to investigate the variability of scalar gases and to explore the potential of FODS for resolving their controlling micrometeorological processes.

1.3.2 FODS Implications in Forest Micrometeorology

Forests play a central role in land–atmosphere exchange by absorbing carbon dioxide (CO_2) through photosynthesis. Although they cover only about 30% of the Earth’s surface, forests store nearly half of terrestrial carbon and contribute substantially to global net primary production

(Bonan, 2008). Their structural complexity including heterogeneous canopies, clearings, and variations in vegetation density creates a highly variable flow environment that strongly influences turbulence patterns, scalar transport, and the exchange of mass, momentum, and heat between the forest and the atmosphere. Understanding these processes within the sub-canopy is particularly challenging under weak-wind conditions, which are prevalent at night when stable stratification suppresses turbulence and classical turbulence theories often break down. Despite numerous studies on sub-canopy CO_2 transport, the combined spatiotemporal variability of CO_2, methane (CH_4), and water vapor (H_2O) under contrasting wind regimes remains poorly understood. To address this gap, part of this dissertation (Paper III in chapter two) integrated high-resolution fiber-optic distributed sensing for temperature and wind speed, a dense gas concentration sampling network, and multiple eddy-covariance systems. This observational framework allowed for detailed analysis of vertical and horizontal scalar variability, the influence of thermal stratification, and the identification of key micrometeorological drivers across both strong- and weak-wind regimes in a temperate spruce forest sub-canopy.

During the LOEWE20 experiment, the forest sub-canopy and above-canopy environment displayed complex microclimatic behavior that strongly influenced the distribution and dynamics of scalar gases. Air temperatures varied between 3.2 °C and 26.3 °C, with medians ranging from 13.7 °C to 14.2 °C, showing similar variability above and below the canopy. Scalar wind speeds were significantly reduced within the sub-canopy (0.68–0.76 m s^{-1}) compared to above-canopy conditions (~3 m s^{-1}). The hill tower, located near the southwestern forest edge, experienced higher wind speeds and a different distribution due to its more open canopy, highlighting the spatial heterogeneity of wind dynamics within the forest. TKE was consistently lower in the sub-canopy (median 0.23–0.46 m^2 s^{-2}) than above the canopy (0.96 m^2 s^{-2}). Wind directions were predominantly south-easterly at both heights, with secondary contributions varying by level—north and north-east sub-canopy versus westerly above the canopy. The weak- and strong-wind regime analysis revealed that strong winds prevailed during the daytime, particularly between 09:00 and 16:00, whereas nocturnal periods were dominated by weak winds, often leading to stable stratification near the forest floor and suppressed vertical mixing. The vertical structure of temperature measured by FODS revealed pronounced stratification effects. Under strong-wind conditions, the maximum potential temperature was observed at 22 m height, consistent with

previous studies, and the lower canopy remained stably stratified. Weak-wind regimes led to a stronger stable stratification with vertical temperature differences reaching 2.4 K. Wind speed profiles indicated a sharp decrease from above-canopy to sub-canopy levels due to momentum absorption by leaves and branches, with notable local maxima at ~3 m and minima at ~11 m, reflecting complex drag and turbulence interactions within the canopy.

Measurements of sub-canopy scalar gas mixing ratios revealed clear vertical gradients and diurnal dynamics for CO_2, CH_4, and H_2O. CO_2 accumulated near the forest floor during night-time weak-wind periods due to soil respiration under stable stratification, whereas vertical mixing during daytime convection reduced ground-level concentrations. Horizontal variability was minimal except in locations with more open canopy, where local differences in radiation and turbulence allowed stronger lateral heterogeneity. CH_4 exhibited an inverse vertical gradient, with lowest concentrations at the soil surface, consistent with forest soils acting as a methane sink. Vertical spatial variability of CH_4 was largely driven by mechanical shear and turbulence, whereas horizontal variability depended on advection and local wind dynamics. Water vapor mixing ratios mirrored ET dynamics, with vertical accumulation near the ground under stable stratification and daytime peaks driven by solar radiation and enhanced ET. Horizontal H_2O variability was most pronounced in regions with open canopy or structural heterogeneity, where localized ET rates amplified lateral differences in moisture content.

The spatiotemporal variability of scalar gases was closely linked to wind regime and turbulence intensity. Weak-wind conditions suppressed vertical mixing and enhanced both CO_2 and CH_4 variability, while strong-wind daytime convection promoted more uniform vertical distributions. H_2O variability, however, was largely independent of wind strength and instead strongly tied to daytime radiation and ET, reflecting the direct influence of energy availability and plant physiological activity. Statistical analyses using random forest modeling highlighted that vertical turbulence metrics, including TKE, vertical velocity fluctuations, and stability parameters, were the primary drivers of CO_2 variability under strong-wind conditions, while temperature dominated during weak-wind periods. For CH_4, temperature consistently influenced vertical mixing, with horizontal variability additionally affected by wind shear and advection. H_2O variability was dominated by temperature and energy-driven ET dynamics across all regimes, underscoring its dependence on radiation and physiological processes rather than turbulence alone.

FODS-derived potential temperature profiles provided further insight into the mechanisms controlling scalar gas variability. Clustering analyses revealed distinct stratification regimes, including unstable daytime profiles that promote mixing, stable nocturnal profiles that suppress vertical exchange, and near-neutral conditions during transition periods. These profiles explained the vertical and horizontal variability of CO_2 and CH_4, with unstable or near-neutral conditions reducing spatial gradients and stable stratification enhancing scalar accumulation, particularly near the forest floor and canopy top. For H_2O, vertical and horizontal variability was influenced by both stratification and heterogeneous ET sources, including differences in ground versus canopy transpiration, soil moisture, and local canopy structure. Transition periods were particularly important, as residual ET persisted under weakly stratified conditions, creating localized enhancements in spatial heterogeneity.

Overall, the results emphasize the critical role of forest microclimate in shaping scalar gas transport and distribution. Vertical variability was consistently higher than horizontal variability, reflecting the dominant influence of canopy-driven stratification and turbulence suppression. The interplay between thermal stratification, turbulence intensity, and canopy structural heterogeneity determines the accumulation, dispersion, and mixing of CO_2, CH_4, and H_2O within the forest sub-canopy. High-resolution measurements from dense sensor networks like GCSN and FODS proved essential for capturing these fine-scale spatiotemporal patterns, providing valuable data for understanding forest-atmosphere interactions and improving ecosystem-scale gas flux modeling. These findings have important implications for forest management, carbon budgeting, and climate mitigation strategies, as they quantify the mechanisms controlling trace gas exchange under varying micrometeorological conditions, highlighting the need to incorporate detailed microclimatic processes into predictive models. By integrating observational data with statistical modeling, the study demonstrated a comprehensive framework for assessing scalar variability, revealing the sensitivity of forest sub-canopy processes to wind regime, temperature, and canopy structure, and providing a foundation for further research into the drivers of greenhouse gas dynamics in complex forest environments.

1.4 Recommendations and Future Perspectives

Building on the combined findings of the three studies including: microstructure optimization, vertical-wind detection experiments, and sub-canopy scalar variability analysis a number of strategic research directions emerge to advance the use of FODS in micrometeorology, particularly under weak-wind conditions and within structurally complex environments such as forest canopies.

I. Perform comprehensive experimental validation of the optimized hollow-coned fiber designs across multiple ecosystems and turbulence regimes. The numerical results demonstrated that hollow-coned microstructures dramatically enhance the thermal contrast (ΔT) between forward- and backward-facing fibers while maintaining performance under varying turbulence intensities and oblique wind angles. To transition from simulation to operational deployment, these designs should be tested in wind tunnels, open fields, forest canopies, and heterogeneous sub-canopy terrains. Validation should include steady and unsteady atmospheric conditions, diurnal transitions, and intermittent turbulence characteristic of stable boundary layers.

II. Integrate next-generation fiber-optic cables, once commercially available, that offer higher thermal sensitivity and shorter thermal response times. The usefulness of FODS in turbulence studies is fundamentally limited by the thermal inertia of current fibers. Faster response times will allow detection of higher-frequency eddies and wind perturbations. When combined with optimized hollow-cone microstructures, these cables would enable true high-frequency, distributed wind sensing and could markedly improve the retrieval of vertical wind speed and direction and eventually the sensible heat flux from FODS alone.

III. Combine FODS-based wind and temperature retrievals with data-driven models to characterize three-dimensional turbulence in canopy environments. Random forest models used in the scalar-variability study revealed strong nonlinear relationships between stability parameters, turbulence metrics, and spatial patterns of CO_2, CH_4, and H_2O. Integrating these machine-learning approaches with spatially continuous FODS temperature fields and future FODS-derived wind and flux estimates would allow reconstruction of 3D turbulence fields at unprecedented resolution. Hybrid physics–ML models could identify key drivers of

scalar transport, detect coherence events, and map regions of efficient or suppressed mixing within canopies.

IV. Use FODS to study weak-wind regimes in forests as natural laboratories for testing new turbulence theories. Weak-wind conditions challenge nearly all classical turbulence frameworks, including Monin–Obukhov similarity theory, Reynolds averaging assumptions, and inertial-subrange scaling. Dense FODS arrays can serve as a spatial benchmark for testing alternative frameworks such as mixing-layer analogies, non-local turbulence production, or sub-mesoscale-driven variability. Targeting transition periods (evening/morning) and topographically influenced flows will be particularly valuable.

V. Pursue multi-scale modeling that couples LES (Large Eddy Simulation) and RANS (Reynolds-Averaged Navier-Stokes), and FODS-derived observations. While LES provides detailed turbulence fields, it struggles with realistic canopies and weak-wind stability. FODS can fill this observational gap. Coupling LES with FODS-derived temperature and wind fields especially using optimized microstructures would help constrain canopy drag formulations, improve scalar mixing parameterizations, and reduce model biases under stable conditions.

VI. Explore fully distributed flux estimation using only FODS-derived variables. The unshrouded fiber experiments demonstrated that ΔT signals can correlate strongly with vertical wind under favorable conditions, enabling the first spatially distributed sensible heat flux estimates derived solely from FODS. Extending this approach by (a) incorporating hollow-cone microstructures, (b) deploying multiple vertically stacked fibers, and (c) combining retrieved wind with scalar gradients (e.g., H_2O from Raman FODS) could make it possible to compute distributed fluxes of heat, moisture, and potentially CO_2 at the sub-canopy scale.

1.5 References

Abdoli, M., Lapo, K., Schneider, J., Olesch, J., Thomas, C.K., 2023. Toward quantifying turbulent vertical airflow and sensible heat flux in tall forest canopies using fiber-optic distributed temperature sensing. Atmospheric Meas. Tech. 16, 809–824. https://doi.org/10.5194/amt-16-809-2023

Abdoli, M., Lapo, K., Thomas, C.K., 2025a. Dynamic stability and canopy structure drive Spatio-Temporal Variability of Greenhouse Gases in the sub-canopy of a Temperate Spruce Forest. https://doi.org/10.2139/ssrn.5681842, [preprint]

Abdoli, M., Pirkhoshghiyafeh, R., Thomas, C.K., 2025b. Improving turbulent airflow direction measurements for fiber-optic distributed sensing using numerical simulations. Atmospheric Meas. Tech. 18, 6417–6433. https://doi.org/10.5194/amt-18-6417-2025

Anfossi, D., Oettl, D., Degrazia, G., Goulart, A., 2005. An Analysis Of Sonic Anemometer Observations In Low Wind Speed Conditions. Bound.-Layer Meteorol. 114, 179–203. https://doi.org/10.1007/s10546-004-1984-4

Aubinet, M., Feigenwinter, C., Heinesch, B., Bernhofer, C., Canepa, E., Lindroth, A., Montagnani, L., Rebmann, C., Sedlak, P., Van Gorsel, E., 2010. Direct advection measurements do not help to solve the night-time CO2 closure problem: Evidence from three different forests. Agric. For. Meteorol., Special Issue on Advection: ADVEX and Other Direct Advection Measurement Campaigns 150, 655–664. https://doi.org/10.1016/j.agrformet.2010.01.016

Bado, M.F., 2021. Distributed Sensing for Serviceability Analysis of Reinforced Concrete Structures. Httpstalpyklaelabaltelaba-Fedoraobjectselaba101474296datastreamsMAINcontent.

Baldocchi, D.D., 2020. How eddy covariance flux measurements have contributed to our understanding of Global Change Biology. Glob. Change Biol. 26, 242–260. https://doi.org/10.1111/gcb.14807

Belcher, S., Finnigan, J., Harman, I., 2008. Flows through forest canopies in complex terrain. Ecol. Appl. 18, 1436–1453.

Bense, V.F., Read, T., Verhoef, A., 2016. Using distributed temperature sensing to monitor field scale dynamics of ground surface temperature and related substrate heat flux. Agric. For. Meteorol. 220, 207–215. https://doi.org/10.1016/j.agrformet.2016.01.138

Boekee, J., van der Linden, S.J.A., ten Veldhuis, M.-C., Verouden, I.E.A., Nollen, P.J., Dai, Y., Jongen, H.J., van de Wiel, B.J.H., 2024. Rethinking the Roughness Height: An Improved Description of Temperature Profiles over Short Vegetation. Bound.-Layer Meteorol. 190, 31. https://doi.org/10.1007/s10546-024-00871-z

Bonan, G.B., 2008. Forests and climate change: forcings, feedbacks, and the climate benefits of forests. science 320, 1444–1449.

Burgers, J.M., 1948. A Mathematical Model Illustrating the Theory of Turbulence. Adv. Appl. Mech. 1, 171–199. https://doi.org/10.1016/S0065-2156(08)70100-5

Chowdhuri, S., Mammarella, I., Peltola, O., 2025. Validity of Taylor's Frozen Turbulence Hypothesis Within a Forest Clearing. Presented at the 25th Symposium on Boundary Layers and Turbulence, AMS.

de Jong, S. a. P., Slingerland, J.D., van de Giesen, N.C., 2015. Fiber optic distributed temperature sensing for the determination of air temperature. Atmospheric Meas. Tech. 8, 335–339. https://doi.org/10.5194/amt-8-335-2015

des Tombe, B., Schilperoort, B., Bakker, M., 2020. Estimation of Temperature and Associated Uncertainty from Fiber-Optic Raman-Spectrum Distributed Temperature Sensing. Sensors 20, 2235. https://doi.org/10.3390/s20082235

Engelmann, C., Bernhofer, C., 2016. Exploring Eddy-Covariance Measurements Using a Spatial Approach: The Eddy Matrix. Bound.-Layer Meteorol. 161, 1–17. https://doi.org/10.1007/s10546-016-0161-x

Feigenwinter, C., Mölder, M., Lindroth, A., Aubinet, M., 2010. Spatiotemporal evolution of CO2 concentration, temperature, and wind field during stable nights at the Norunda forest site. Agric. For. Meteorol. 150, 692–701.

Finnigan, J., 2000. Turbulence in Plant Canopies. Annu. Rev. Fluid Mech. 32, 519–571. https://doi.org/10.1146/annurev.fluid.32.1.519

Freundorfer, A., Lapo, K., Schneider, J., Thomas, C.K., 2021. Distributed sensing of wind direction using fiber-optic cables. J. Atmospheric Ocean. Technol. 38, 1871–1883.

Frisch, U., Kolmogorov, A.N., 1995. Turbulence: The Legacy of A. N. Kolmogorov. Cambridge University Press.

Fritz, A.M., Lapo, K., Freundorfer, A., Linhardt, T., Thomas, C.K., 2021. Revealing the Morning Transition in the Mountain Boundary Layer Using Fiber-Optic Distributed Temperature Sensing. Geophys. Res. Lett. 48, e2020GL092238. https://doi.org/10.1029/2020GL092238

Grachev, A.A., Andreas, E.L., Fairall, C.W., Guest, P.S., Persson, P.O.G., 2013. The critical Richardson number and limits of applicability of local similarity theory in the stable boundary layer. Bound. Layer Meteorol 147, 51–82.

Higgins, C.W., Wing, M.G., Kelley, J., Sayde, C., Burnett, J., Holmes, H.A., 2018. A high resolution measurement of the morning ABL transition using distributed temperature sensing and an unmanned aircraft system. Environ. Fluid Mech. 18, 683–693. https://doi.org/10.1007/s10652-017-9569-1

Holtslag, A. a. M., Svensson, G., Baas, P., Basu, S., Beare, B., Beljaars, A.C.M., Bosveld, F.C., Cuxart, J., Lindvall, J., Steeneveld, G.J., Tjernström, M., Wiel, B.J.H.V.D., 2013. Stable Atmospheric Boundary Layers and Diurnal Cycles: Challenges for Weather and Climate Models. https://doi.org/10.1175/BAMS-D-11-00187.1

Huss, J.-M., Thomas, C.K., 2024. The Impact of Turbulent Transport Efficiency on Surface Vertical Heat Fluxes in the Arctic Stable Boundary Layer Predicted from Similarity Theory and Machine Learning. https://doi.org/10.1175/JAS-D-24-0063.1

Ishii, H., Kawamura, K., Ono, T., Megumi, H., Kikkawa, A., 1997. A fire detection system using optical fibres for utility tunnels. Fire Saf. J. 29, 87–98. https://doi.org/10.1016/S0379-7112(96)00065-3

Kaimal, J.C., Finnigan, J.J., 1994. Atmospheric Boundary Layer Flows: Their Structure and Measurement. Oxford University Press.

Kalantari, H., Ghoreishi-Madiseh, S.A., Kurnia, J.C., Sasmito, A.P., 2021. An analytical correlation for conjugate heat transfer in fin and tube heat exchangers. Int. J. Therm. Sci. 164, 106915. https://doi.org/10.1016/j.ijthermalsci.2021.106915

Karttunen, S., O'Connor, E., Peltola, O., Järvi, L., 2022. Quantifying the coastal urban surface layer structure using distributed temperature sensing in Helsinki, Finland. Atmospheric Meas. Tech. 15, 2417–2432. https://doi.org/10.5194/amt-15-2417-2022

Keller, C.A., Huwald, H., Vollmer, M.K., Wenger, A., Hill, M., Parlange, M.B., Reimann, S., 2011. Fiber optic distributed temperature sensing for the determination of the nocturnal atmospheric boundary layer height. Atmospheric Meas. Tech. 4, 143–149. https://doi.org/10.5194/amt-4-143-2011

Lapo, K., Freundorfer, A., Fritz, A., Schneider, J., Olesch, J., Babel, W., Thomas, C.K., 2022. The Large eddy Observatory, Voitsumra Experiment 2019 (LOVE19) with high-resolution, spatially distributed observations of air temperature, wind speed, and wind direction from fiber-optic distributed sensing, towers, and ground-based remote sensing. Earth Syst. Sci. Data 14, 885–906. https://doi.org/10.5194/essd-14-885-2022

Lapo, K., Freundorfer, A., Pfister, L., Schneider, J., Selker, J., Thomas, C., 2020. Distributed observations of wind direction using microstructures attached to actively heated fiber-optic cables. Atmospheric Meas. Tech. 13, 1563–1573. https://doi.org/10.5194/amt-13-1563-2020

LeMone, M.A., Angevine, W.M., Bretherton, C.S., Chen, F., Dudhia, J., Fedorovich, E., Katsaros, K.B., Lenschow, D.H., Mahrt, L., Patton, E.G., Sun, J., Tjernström, M., Weil, J., 2019. 100 Years of Progress in Boundary Layer Meteorology. https://doi.org/10.1175/AMSMONOGRAPHS-D-18-0013.1

Liang, J., Zhang, L., Wang, Y., Cao, X., Zhang, Q., Wang, H., Zhang, B., 2014. Turbulence regimes and the validity of similarity theory in the stable boundary layer over complex terrain of the Loess Plateau, China. J Geophys Res 119, 6009–6021.

Luyssaert, S., Inglima, I., Jung, M., Richardson, A.D., Reichstein, M., Papale, D., Piao, S.L., Schulze, E.-D., Wingate, L., Matteucci, G., Aragao, L., Aubinet, M., Beer, C., Bernhofer, C., Black, K.G., Bonal, D., Bonnefond, J.-M., Chambers, J., Ciais, P., Cook, B., Davis, K.J., Dolman, A.J., Gielen, B., Goulden, M., Grace, J., Granier, A., Grelle, A., Griffis, T., Grünwald, T., Guidolotti, G., Hanson, P.J., Harding, R., Hollinger, D.Y., Hutyra, L.R., Kolari, P., Kruijt, B., Kutsch, W., Lagergren, F., Laurila, T., Law, B.E., Le Maire, G., Lindroth, A., Loustau, D., Malhi, Y., Mateus, J., Migliavacca, M., Misson, L., Montagnani, L., Moncrieff, J., Moors, E., Munger, J.W., Nikinmaa, E., Ollinger, S.V., Pita, G., Rebmann, C., Roupsard, O., Saigusa, N., Sanz, M.J., Seufert, G., Sierra, C., Smith, M.-L., Tang, J., Valentini, R., Vesala, T., Janssens, I.A., 2007. CO2 balance of boreal, temperate, and tropical forests derived from a global database. Glob. Change Biol. 13, 2509–2537. https://doi.org/10.1111/j.1365-2486.2007.01439.x

Mack, L., Kähnert, M., Rauschenbach, Q., Frank, L., Hasenburg, F.H., Huss, J.-M., Jonassen, M.O., Malpas, M., Batrak, Y., Remes, T., Pirk, N., Thomas, C.K., 2025. Stable Boundary

Layers in an Arctic Fjord-Valley System: Evaluation of Temperature Profiles Observed From Fiber-Optic Distributed Sensing and Comparison to Numerical Weather Prediction Systems at Different Resolutions. J. Geophys. Res. Atmospheres 130, e2024JD042825. https://doi.org/10.1029/2024JD042825

Mahrt, L., 2014. Stably Stratified Atmospheric Boundary Layers. Annu. Rev. Fluid Mech. 46, 23–45. https://doi.org/10.1146/annurev-fluid-010313-141354

Mahrt, L., 2010. Variability and Maintenance of Turbulence in the Very Stable Boundary Layer. Bound.-Layer Meteorol. 135, 1–18. https://doi.org/10.1007/s10546-009-9463-6

Mahrt, L., Sun, J., Stauffer, D., 2015. Dependence of Turbulent Velocities on Wind Speed and Stratification. Bound.-Layer Meteorol. 155, 55–71. https://doi.org/10.1007/s10546-014-9992-5

Mahrt, L., Thomas, C., Richardson, S., Seaman, N., Stauffer, D., Zeeman, M., 2013. Non-stationary Generation of Weak Turbulence for Very Stable and Weak-Wind Conditions. Bound.-Layer Meteorol. 147, 179–199. https://doi.org/10.1007/s10546-012-9782-x

Mahrt, L., Vickers, D., 2003. Formulation of Turbulent Fluxes in the Stable Boundary Layer.

Monin, A.S., Obukhov, A.M., 1954. Basic laws of turbulent mixing in the surface layer of the atmosphere.

Pan, Y., Birdsey, R.A., Fang, J., Houghton, R., Kauppi, P.E., Kurz, W.A., Phillips, O.L., Shvidenko, A., Lewis, S.L., Canadell, J.G., Ciais, P., Jackson, R.B., Pacala, S.W., McGuire, A.D., Piao, S., Rautiainen, A., Sitch, S., Hayes, D., 2011. A Large and Persistent Carbon Sink in the World's Forests. Science 333, 988–993. https://doi.org/10.1126/science.1201609

Peltola, O., Aurela, M., Launiainen, S., Katul, G., 2022. Probing eddy size and its effective mixing length in stably stratified roughness sublayer flows. Q. J. R. Meteorol. Soc. 148, 3756–3773. https://doi.org/10.1002/qj.4386

Peltola, O., Lapo, K., Martinkauppi, I., O'Connor, E., Thomas, C.K., Vesala, T., 2021. Suitability of fibre-optic distributed temperature sensing for revealing mixing processes and higher-order moments at the forest–air interface. Atmospheric Meas. Tech. 14, 2409–2427.

Pfister, L., Lapo, K., Mahrt, L., Thomas, C.K., 2021a. Thermal Submeso Motions in the Nocturnal Stable Boundary Layer. Part 2: Generating Mechanisms and Implications. Bound.-Layer Meteorol. 180, 203–224. https://doi.org/10.1007/s10546-021-00619-z

Pfister, L., Lapo, K., Mahrt, L., Thomas, C.K., 2021b. Thermal Submeso Motions in the Nocturnal Stable Boundary Layer. Part 2: Generating Mechanisms and Implications. Bound.-Layer Meteorol. 180, 203–224. https://doi.org/10.1007/s10546-021-00619-z

Poulos, G.S., Burns, S.P., 2003. An Evaluation of Bulk Ri-Based Surface Layer Flux Formulas for Stable and Very Stable Conditions with Intermittent Turbulence.

Ren, Y., Zhang, H., Zhang, X., Cai, X., Song, Y., Liang, J., Zhang, L., Zhu, T., Huang, J., 2025. Research progress and current application of weak turbulence and turbulence intermittency in stable boundary layers. Earth-Sci. Rev. 262, 105062. https://doi.org/10.1016/j.earscirev.2025.105062

Sandu, I., Beljaars, A., Bechtold, P., Mauritsen, T., Balsamo, G., 2013. Why is it so difficult to represent stably stratified conditions in numerical weather prediction (NWP) models? J. Adv. Model. Earth Syst. 5, 117–133. https://doi.org/10.1002/jame.20013

Sayde, C., Thomas, C.K., Wagner, J., Selker, J., 2015. High-resolution wind speed measurements using actively heated fiber optics. Geophys. Res. Lett. 42, 10,064-10,073. https://doi.org/10.1002/2015GL066729

Schilperoort, B., Coenders-Gerrits, M., Jiménez Rodríguez, C., van der Tol, C., Van De Wiel, B., Savenije, H., 2020. Decoupling of a Douglas fir canopy: a look into the subcanopy with continuous vertical temperature profiles. Biogeosciences Discuss. 2020, 1–25.

Selker, J.S., Thévenaz, L., Huwald, H., Mallet, A., Luxemburg, W., Van De Giesen, N., Stejskal, M., Zeman, J., Westhoff, M., Parlange, M.B., 2006. Distributed fiber-optic temperature sensing for hydrologic systems. Water Resour. Res. 42, 2006WR005326. https://doi.org/10.1029/2006WR005326

Silva, L.C.B., Segatto, M.E.V., Castellani, C.E.S., 2022. Raman scattering-based distributed temperature sensors: A comprehensive literature review over the past 37 years and towards new avenues. Opt. Fiber Technol. 74, 103091. https://doi.org/10.1016/j.yofte.2022.103091

Steele-Dunne, S.C., Rutten, M.M., Krzeminska, D.M., Hausner, M., Tyler, S.W., Selker, J., Bogaard, T.A., van de Giesen, N.C., 2010. Feasibility of soil moisture estimation using passive distributed temperature sensing. Water Resour. Res. 46. https://doi.org/10.1029/2009WR008272

Stiperski, I., Rotach, M.W., Ansorge, C., Baklanov, A., Belušić, D., Bou-Zeid, E., Brun, C., Christen, A., Dias, N.L., Dörnbrack, A., Foken, T., Grachev, A., Holtslag, A.A.M., Kelly, M., Klein, P., Kosović, B., Meneveau, C., Mortarini, L., Patton, E.G., Steeneveld, G.-J., Thomas, C., Trini Castelli, S., Zardi, D., 2025. Open questions in atmospheric turbulence: A synthesis from the centenary workshop "100 years of turbulence: Innsbruck 1922 - 2022." J. Eur. Meteorol. Soc. 3, 100022. https://doi.org/10.1016/j.jemets.2025.100022

Stull, R.B., 1988. Turbulence Kinetic Energy, Stability and Scaling, in: Stull, R.B. (Ed.), An Introduction to Boundary Layer Meteorology. Springer Netherlands, Dordrecht, pp. 151–195. https://doi.org/10.1007/978-94-009-3027-8_5

Sun, J., Mahrt, L., Banta, R.M., Pichugina, Y.L., 2012. Turbulence Regimes and Turbulence Intermittency in the Stable Boundary Layer during CASES-99. https://doi.org/10.1175/JAS-D-11-082.1

Taylor, G.I., 1938. The Spectrum of Turbulence. Proc. R. Soc. Lond. Ser. - Math. Phys. Sci. 164, 476–490. https://doi.org/10.1098/rspa.1938.0032

Tennekes, H., Lumley, J.L., 1972. A First Course in Turbulence. MIT Press.

ter Horst, C.G.B., Vis, G.A., Jongen-Boekee, J., ten Veldhuis, M.-C., Hut, R.W., van de Wiel, B.J.H., 2025. An Adaptable DTS-based Parametric Method to Probe Near-surface Vertical Temperature Profiles at Millimeter Resolution. EGUsphere 1–25. https://doi.org/10.5194/egusphere-2025-1397

Thomas, C.K., 2011. Variability of sub-canopy flow, temperature, and horizontal advection in moderately complex terrain. Bound.-Layer Meteorol. 139, 61–81.

Thomas, C.K., Kennedy, A.M., Selker, J.S., Moretti, A., Schroth, M.H., Smoot, A.R., Tufillaro, N.B., Zeeman, M.J., 2012. High-Resolution Fibre-Optic Temperature Sensing: A New Tool to Study the Two-Dimensional Structure of Atmospheric Surface-Layer Flow. Bound.-Layer Meteorol. 142, 177–192. https://doi.org/10.1007/s10546-011-9672-7

Thomas, C.K., Law, B.E., Irvine, J., Martin, J.G., Pettijohn, J.C., Davis, K.J., 2009. Seasonal hydrology explains interannual and seasonal variation in carbon and water exchange in a semiarid mature ponderosa pine forest in central Oregon. J. Geophys. Res. Biogeosciences 114.

Thomas, C.K., Selker, J., 2021. Optical Fiber-Based Distributed Sensing Methods, in: Foken, T. (Ed.), Springer Handbook of Atmospheric Measurements. Springer International Publishing, Cham, pp. 609–631. https://doi.org/10.1007/978-3-030-52171-4_20

Tyler, S.W., Selker, J.S., Hausner, M.B., Hatch, C.E., Torgersen, T., Thodal, C.E., Schladow, S.G., 2009. Environmental temperature sensing using Raman spectra DTS fiber-optic methods. Water Resour. Res. 45. https://doi.org/10.1029/2008WR007052

Ukil, A., Braendle, H., Krippner, P., 2012. Distributed Temperature Sensing: Review of Technology and Applications. IEEE Sens. J. 12, 885–892. https://doi.org/10.1109/JSEN.2011.2162060

Van de Wiel, B.J.H., Moene, A.F., Jonker, H.J.J., Baas, P., Basu, S., Donda, J.M.M., Sun, J., Holtslag, A.A.M., 2012. The minimum wind speed for sustainable turbulence in the nocturnal boundary layer. J Atmos Sci 69, 3116–3127.

van Ramshorst, J.G.V., Coenders-Gerrits, M., Schilperoort, B., van de Wiel, B.J.H., Izett, J.G., Selker, J.S., Higgins, C.W., Savenije, H.H.G., van de Giesen, N.C., 2020. Revisiting wind speed measurements using actively heated fiber optics: a wind tunnel study. Atmospheric Meas. Tech. 13, 5423–5439. https://doi.org/10.5194/amt-13-5423-2020

Wilson, K.B., Meyers, T.P., 2001. The spatial variability of energy and carbon dioxide fluxes at the floor of a deciduous forest. Bound.-Layer Meteorol. 98, 443–473.

Zeeman, M.J., Selker, J.S., Thomas, C.K., 2015. Near-Surface Motion in the Nocturnal, Stable Boundary Layer Observed with Fibre-Optic Distributed Temperature Sensing. Bound.-Layer Meteorol. 154, 189–205. https://doi.org/10.1007/s10546-014-9972-9

Zeller, M.-L., Huss, J.-M., Pfister, L., Lapo, K.E., Littmann, D., Schneider, J., Schulz, A., Thomas, C.K., 2021. The NY-Ålesund TurbulencE Fiber Optic eXperiment (NYTEFOX): investigating the Arctic boundary layer, Svalbard. Earth Syst. Sci. Data 13, 3439–3452. https://doi.org/10.5194/essd-13-3439-2021

Chapter Two
Publications

Paper I

Toward quantifying turbulent vertical airflow and sensible heat flux in tall forest canopies using fiber-optic distributed temperature sensing

Status: Published (2023)
Journal: Atmospheric Measurement Techniques Discussions
doi: https://doi.org/10.5194/amt-16-809-2023

Atmos. Meas. Tech., 16, 809–824, 2023
https://doi.org/10.5194/amt-16-809-2023

Atmospheric Measurement Techniques
Open Access
EGU

Toward quantifying turbulent vertical airflow and sensible heat flux in tall forest canopies using fiber-optic distributed temperature sensing

Mohammad Abdoli[1], **Karl Lapo**[1,2], **Johann Schneider**[1], **Johannes Olesch**[1], **and Christoph K. Thomas**[1,2]

[1]Department of Micrometeorology, University of Bayreuth, Bayreuth, Germany
[2]Bayreuth Center of Ecology and Environmental Research, Bayreuth, Germany

Correspondence: Mohammad Abdoli (mohammad.abdoli@uni-bayreuth.de)

Received: 11 July 2022 – Discussion started: 24 August 2022
Revised: 22 December 2022 – Accepted: 25 January 2023 – Published: 14 February 2023

Abstract. The paper presents a set of fiber-optic distributed temperature sensing (FODS) experiments to expand the existing microstructure approach for horizontal turbulent wind direction by adding measurements of turbulent vertical component, as well as turbulent sensible heat flux. We address the observational challenge to isolate and quantify the weaker vertical turbulent motions from the much stronger mean advective horizontal flow signals. In the first part of this study, we test the ability of a cylindrical shroud to reduce the horizontal wind speed while keeping the vertical wind speed unaltered. A white shroud with a rigid support structure and 0.6 m diameter was identified as the most promising setup in which the correlation of flow properties between shrouded and reference systems is maximized. The optimum shroud setup reduces the horizontal wind standard deviation by 35 %, has a coefficient of determination of 0.972 for vertical wind standard deviations, and a RMSE of less than 0.018 ms^{-1} when compared to the reference. Spectral analysis showed a fixed ratio of spectral energy reduction in the low frequencies, e.g., <0.5 Hz, for temperature and wind components, momentum, and sensible heat flux. Unlike low frequencies, the ratios decrease exponentially in the high frequencies, which means the shroud dampens the high-frequency eddies with a timescale <6 s, considering both spectra and cospectra together. In the second part, the optimum shroud configuration was installed around a heated fiber-optic cable with attached microstructures in a forest to validate our findings. While this setup failed to isolate the magnitude and sign of the vertical wind perturbations from FODS in the shrouded portion, concurrent observations from an unshrouded part of the FODS sensor in the weak-wind subcanopy of the forest (12–17 m above ground level) yielded physically meaningful measurements of the vertical motions associated with coherent structures. These organized turbulent motions have distinct sweep and ejection phases. These strong flow signals allow for detecting the turbulent vertical airflow at least 60 % of the time and 71 % when conditional sampling was applied. Comparison of the vertical wind perturbations against those from sonic anemometry yielded correlation coefficients of 0.35 and 0.36, which increased to 0.53 and 0.62 for conditional sampling. This setup enabled computation of eddy covariance-based direct sensible heat flux estimates solely from FODS, which are reported here as a methodological and computational novelty. Comparing them against those from eddy covariance using sonic anemometry yielded an encouraging agreement in both magnitude and temporal variability for selected periods.

1 Introduction

Most fluids at sufficiently high Reynolds numbers feature general flow patterns combined with random motions called "turbulence" (Corrsin, 1961). From a micrometeorological point of view, turbulence is the primary mechanism for mixing energy and matter in the air, and its strength controls the coupling between the atmosphere and the earth surface (Burgers, 1948; Tennekes et al., 1972). Understanding the nature of turbulent flow is essential for many applications, such as the transfer and mixing of light, heat, water vapor,

Published by Copernicus Publications on behalf of the European Geosciences Union.

carbon dioxide, nutrients, and other substances, directly affecting humans, animals, and plants' quality of life. Although current theories describe the transport and turbulent mixing near the surface for sufficiently strong winds well (Van de Wiel et al., 2012), under stable regimes, the atmospheric boundary layer (ABL) turbulence does not obey well-known concepts, including the Monin–Obukhov similarity theory, the Kolmogorov spectrum, and Taylor's hypothesis of frozen turbulence (Sun et al., 2012; Grachev et al., 2013; Cheng et al., 2017).

For weak-wind conditions, turbulence is not exclusively governed by dynamic stability but is driven by a combination of non-stationary processes, sub-mesoscale motions, local shear, and flow instabilities (Sun et al., 2012; Mahrt et al., 2013; Liang et al., 2014). Intermittent turbulence or non-stationary conditions often violate assumptions made for scaling laws and statistical approaches used in micrometeorology, including translation of temporal scales into length scales through applying the assumption of Taylor's frozen turbulence. Also, the ergodicity assumption cannot be applied to the single-point measurements in these conditions. The ergodicity assumption states that the time and space averages converge under stationary, horizontally homogeneous conditions (Engelmann and Bernhofer, 2016). Several efforts have been made to analyze observations from networks of sensors to elucidate intermittent processes such as meandering and within-canopy flow and heat transport (Anfossi et al., 2005; Thomas, 2011). Despite some progress in the mentioned studies, the lack of spatial information sufficiently dense to resolve the process scales has hindered advancing the stable boundary layer's current physical interpretation.

Fiber-optic distributed temperature sensing (FODS) has been introduced as a powerful geophysical technique in the last few years. This technique measures the temperature along a fiber-optic cable at a time resolution of a few seconds and spatial resolution of tens of centimeters up to 20 km in total length (Thomas and Selker, 2021). It is capable of observing atmospheric flows under physically poorly understood sub-meso motions (Thomas et al., 2012; Pfister et al., 2021). The distributed temperature sensing (DTS) technique's utility in atmospheric measurement is not limited to measuring the distributed temperature of the air, water, ice, snow, soil, and plant, but various applications such as measurement of evapotranspiration, soil moisture, humidity, shortwave radiation, and wind speed have been tested successfully (Predosa, 2016; Schilperoort et al., 2020; Thomas and Selker, 2021).

Among the most recent development of this technique, Lapo et al. (2020) introduced an approach using an FO cable with a cone-shaped microstructure printed on it, which causes directional differences in the convective heat loss from the FO cable to the air. When heated coned fibers are placed in the main flow direction, the fibers on which the cones are aligned with the flow cool more than those with opposing alignment, enabling computation of wind direction. The before-mentioned study was conducted in idealized wind tunnel experiments. Very recently, Freundorfer et al. (2021) deployed this approach for the first time during actual field observation. They presented three different methods of calculating turbulent horizontal wind directions from the FODS measurements, indicating the potential of this approach to reveal the wind direction's spatial structures at scales of meters and tens of seconds. The last two studies aimed at building a fully three-dimensional, spatially resolving atmospheric flow sensor as an important step toward a spatially distributed flux sensor using the eddy covariance technique. Although measuring the horizontal wind component was successful, the vertical wind component could not be measured with existing approaches to complete the three-dimensional sensor functionality to date. Measuring the vertical wind component with the heated coned fiber approach is challenging as (i) the magnitude of the vertical wind fluctuations is smaller than the combined signals of horizontal mean and turbulent flows, and (ii) the duration of the vertical events are too short, which leads to vanishing sensitivity in the vertical direction because of the finite response time of the FODS sensor. Isolating the vertical wind signal by filtering the horizontal wind is essential to capture the signals induced by the air's vertical movement. Having truly three-dimensional spatially resolved observations would create a possibility to compute the momentum and sensible heat fluxes independently of the fundamental assumptions of ergodicity, stationarity, and homogeneity, since the observations are taken simultaneously in both time and space domains. For example, it could be used to reveal the generating mechanism of the weak and intermittent turbulence where the conventional observation assumptions fail. A three-dimensional spatially resolved observation could also explain the long-standing problem of counter-gradient flux caused by a poor choice of height in the measurement and perturbation timescale (Vickers and Thomas, 2014; Fritz et al., 2021).

We aimed to overcome these conceptual and observational challenges by conducting a series of experiments. The first part of this study was conducted above an open grassland and used only classic sonic anemometry without FODS to identify an optimal experimental configuration for subsequent testing in the second part with the use of FODS. We diminished the horizontal wind speed using different cylindrical shrouds and compared the flow characteristics inside and outside the shroud by placing a sonic anemometer inside and outside the shroud to investigate (i) which are the optimal physical properties of the shroud (aspect ratio, shape, porosity, rigidity, and color) to diminish the horizontal wind disturbances adequately while leaving the vertical wind perturbations largely unaffected. And (ii) how is the spectra of turbulent fluctuations affected by shroud in high and low frequencies compared to an unshrouded setup? In the second part of this study, a forest environment was used to investigate the applicability of the fiber-optic approach to measuring vertical wind components. We considered forests an ideal test environment, since the mixing-layer-type flow character-

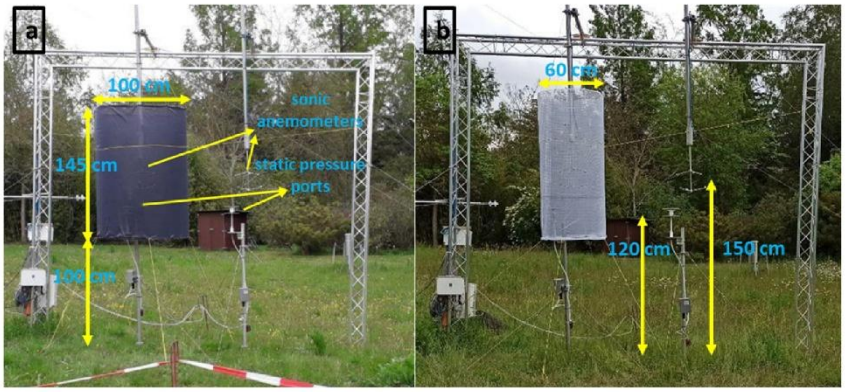

Figure 1. Two examples of a shroud experiment setup containing two upside-down sonic anemometers and two high-precision pressure transducers with the quad disk to measure static pressure. **(a)** A 1 m diameter cylindrical shroud with fine-porosity gray color texture. **(b)** A 60 cm cylindrical shroud with a white insect screen.

ized by coherent structures with strong vertical motions and the sweep and ejection phases in the subcanopy allow for sustained stronger vertical wind speed compared to horizontal wind speed (Brunet, 2020). We deployed a shroud based on the results of the first part around heated coned FO cables in the forest area to see (iii) whether vertical wind direction and wind speed can be resolved by affixing a shroud around actively heated coned FO cables and if this setup can be used to compute the sensible heat flux purely based on FODS. If yes, how is the quality of the derived component based on point measurement?

2 Material and methods

2.1 Part 1: shroud experiment over grassland

The first part of the measurements was conducted between April 2020 and June 2020 at the Ecological Botanical Garden (EBG) at the University of Bayreuth. The experimental area was covered with short grass (5–15 cm) surrounded by mixed types of trees with an approximate height of 15 m from north, northeast, and southeast and a small artificial pond on the west side. Based on the synoptic weather station data close to the experiment location from 2014 to 2018, the dominant wind direction for spring and summer is westerly and southwesterly, with a maximum wind speed of 8–12 ms^{-1}. Two upside-down sonic anemometers (Model USA-1, METEK GmbH, Elmshorn, Germany) at a 1.5 m height (middle of the shroud) and two quad disk pressure ports attached to a nano-resolution digital barometer (Model 745-16B, Paroscientific, Inc.) at 1.2 m above ground were set up. One set of sensors was placed inside the cylindrical shroud (Fig. 1). The spacing between two sets of sensors was 1.5 m to reduce the potential airflow distortion of the shrouded setup on the unshrouded setup. White and gray insect screens with a mesh size of approximately 0.5 and 0.1 mm, respectively, are used. The supporting structures of the shroud and sonic anemometers are oriented along the north-west direction, perpendicular to dominant wind speed, to reduce the structure-induced systematic disturbances. A metal wire mesh with a 10 mm × 10 mm grid size is used underneath the shroud to enhance its rigidity against distortion during stronger winds.

We iterated multiple shroud configurations in different diameters (1 and 0.6 m), gray and white colors, small and large pore sizes, and with and without supporting the metal mesh underneath the shroud. The reasoning for each selection is as follows:

- *Diameter*. The task was to design a shroud to eliminate the horizontal flow while keeping the vertical flow perturbation intact. We hypothesized increasing the shroud diameter could increase the horizontal flow disturbances inside the shroud, since it offers a larger pathway for airflow. On the other hand, decreasing the shroud diameter and placing it close to the sonic anemometer could cause systematic turbulence created with the shroud itself.
- *Length*. We determined the length of the shroud over the grass to be long enough to accommodate the typical length scales of the vertical turbulent flow, keep the sensors away from shroud structure-induced flow disturbances, and be feasible to install, given the available hardware and facilities.
- *Color*. We used the gray shroud first. Initial results showed substantial heating of the shroud material

during daytime conditions, inducing strong upward-directed (free) convective heat transfer and thus distorting flow statistics inside the shroud. In response, we changed the shroud's color to white to avoid possible radiative heating errors, together with increasing the pore size of the shroud.

- *Mesh size*. The initial mesh size was selected based on the previous experiments and then improved based on the initial results.
- *Rigidity*. The very first setup of the shroud was designed without supporting mesh and was just a tensioned shroud with two rings at the top and bottom. We observed that the shroud became very unstable during wind gusts and induced uninvited turbulence. We decided to make the shroud rigid enough to avoid this problem.

The sonic anemometer and static pressure data recorded at sampling frequencies of 20 Hz and perturbation and averaging timescales of 10 min were used to compute sensible heat and momentum fluxes and compare wind components inside and outside the shroud. In this part of the study, no FODS techniques were used, and the primary objective was to determine the best configuration of the shroud to meet the study's objectives. Three sets of shroud experiments at EBG were compared in this study with setup 1 standing for a gray, dense 1 m diameter shroud, setup 2 for a gray, dense 60 cm diameter shroud, and setup 3 for a white, not dense 60 cm diameter shroud.

2.2 Part 2: shroud experiment in a forest

The second part of the study evaluated the utility of the shroud approach at the Waldstein–Weidenbrunnen long-term ecosystem flux site between October and November 2020 as part of the Large-eddy ObsErvatory Waldstein Experiment 2020 (LOEWE20) experiment. The Waldstein is a forested site in the Fichtelgebirge Mountains located within the Lehstenbach catchment. This forest was mainly covered by Norway spruce (*Picea abies*), characterized by variable tree heights and densities. Subcanopy vegetation is moderately dense with a cumulative plant area index of $0.7\,m^2\,m^{-2}$, featuring shrubs with a height of ≤ 1 m. The plant area index (PAI) is $5.6 \pm 2.1\,m^2\,m^{-2}$ for the overstory trees and $3.5\,m^2\,m^{-2}$ for the understory trees. In the Waldstein site, westerly and southeasterly wind with a wind speed range of 2 to $5\,ms^{-1}$ dominate in the overstory; in the subcanopy, it is northerly and southwesterly with a range of 1 to $2\,ms^{-1}$ (Foken et al., 2017). The experiment period was mostly dominated by anticyclonic conditions in both 500 and 950 hPa isobaric levels, with southwesterly winds being partly wet and partly dry. The shroud was installed at the main tower around a quartet FO array containing two pairs of parallel coned and unconed FO cables extending from the ground to the top canopy at a 34 m height (Fig. 2). The center of the shroud was placed at 4 m above ground, having the same diameter as the first part of the study, but its lower boundary was located 2.75 m above ground. Two high-resolution DTS instruments (Model 5 km ULTIMA, Silixa, London, UK) were used to observe the continuous temperature with a spatial resolution of 0.127 m averaged over 3 s. The DTS device was connected to one of four 50 µm multimode bend-insensitive cores inside a high-resistance stainless steel sheath filled with gel (inner tube diameter = 1.06 mm, outer diameter = 1.32 mm; Model C-Tube, Solifos AG, Switzerland; resistance $= 1.8\Omega\,m^{-1}$). The cones are made from polyethylene with a diameter and height of 12 mm, spaced at 2 cm along the fiber-optic cable (Lapo et al., 2020). Two warm and cold solid-phase calibration baths with a constant temperature developed by Thomas et al. (2022) were deployed at the beginning and end of FO arrays to be used as a calibration reference (Fig. 2). A sensor package was set outside the shroud close to the center of the cylinder with a sonic anemometer (Model CSAT3, Campbell Scientific Inc., Logan, UT, USA), a quad disk static pressure transducer (Model 745-16B, Paroscientific, Inc.), and an open-path infrared CO_2 / H_2O gas analyzer (Licor 7500, LI-COR Biosciences, USA). For comparison reasons, the eddy covariance data with a sampling frequency of 10 Hz at a 36 m height and the FODS data of quartet array from the turbulence tower located approximately 70 m away from the main tower were used. See Foken et al. (2021) for more details on the turbulence tower specification. The quartet fiber configuration at the turbulence tower is the same as the main tower extending from the ground to a 34 m height. It should be noted that all of the eddy covariance data in this study were sampled at 20 Hz, with the exception of the permanent eddy covariance station at the turbulence tower, which was sampled at 10 Hz. All of the eddy covariance systems in this study use the same eddy covariance data processing and flux computation routine described in Thomas et al. (2009; see Appendix A).

2.3 Change point detection using Pettitt test

In time series analysis, change point detection is a technique for detecting abrupt changes in data. We applied this test to determine the change point of the ratio of the spectral energy in the shrouded setup to the unshrouded setup. The deployed test was proposed by Pettitt (1979) and is a non-parametric test for evaluating single abrupt changes. The change point is computed as follows.

The first step is to calculate U_K statistics using the following Eq. (1):

$$U_k = 2\sum_{i=0}^{n} m_i - k(n+1), \tag{1}$$

where m_i represents the rank of the ith one-dimensional data when the values are arranged in ascending order; and k takes values from $1, 2, \ldots, n$; and in the second step, the statistical

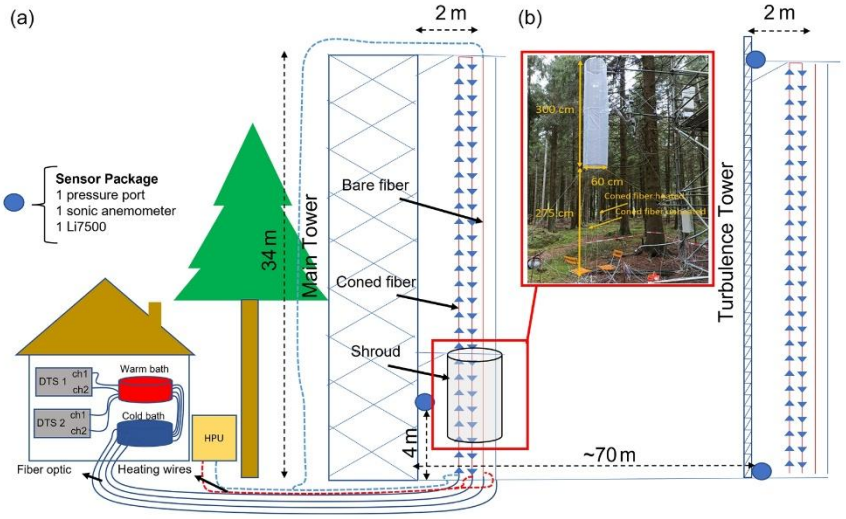

Figure 2. (a) Shroud experiment schematic at Waldstein forest including a quartet of a vertical FO array and affixing a shroud at a 4 m height at the main tower close to the sensor package, including a static pressure port, a sonic anemometer, and an open-path infrared gas analyzer. Each coned and unconed fiber is connected to separate DTS devices. For DTS data calibration purposes, warm and cold baths were deployed at the start and end of each fiber-optic loop. Three FO arrays out of four are heated using a heat pulse unit (HPU). The FO arrays at the turbulence tower wiring are similar to the main tower, which is eliminated due to the simplicity of the schematic. **(b)** Photograph showing the subcanopy shroud experiment and the same vertical quartet FO array at the turbulence tower having the two sensor packages as the main tower at 0.1 and 36 m above ground level.

change point test defines as Eq. (2)

$$K = \max_{1 \le k < n} |U_k|. \tag{2}$$

A change point occurs in a series when U_k reaches its maximum value of K. To test the significance of the detected change points, the critical value (K_a) is obtained with Eq. (3):

$$K_a = \left[\frac{-1n\alpha(n^3 + n^2)}{6} \right]^{\frac{1}{2}}, \tag{3}$$

where n represents the number of observations, and α is the significance level determining the critical value (Zarenistanak et al., 2014).

2.4 FODS calibration

DTS measurements were done in a double-ended configuration fashion using two channels of each DTS device (Van de Giesen et al., 2012). The start and end of each fiber were connected to two different channels, recording the temperature of the fiber by alternating every 3 s between two channels. Each channel was saved separately and aggregated to a single dataset with a time resolution of 6 s during the data post-processing. The coned fibers were heated electrically using the Heat Pulse Unit (HPU) system (Model Heat Pulse System, Silixa, London, UK) and applied a constant electric current of 4 Wm^{-1} to the stainless steel sheath. Observed Stokes and anti-Stokes intensities were converted into fiber temperature using the pyfocs code by Lapo and Freundorfer (2020). This code uses the matrix inversion method using constant temperature sections wrapped around warm and cold solid-state reference baths. The user adjusts the bath's temperature to be set in differentiable cold and warm temperatures based on the ambient temperature range. The reference sections with a length of at least 1.8 m equal to 14 individual measurement points along the fiber were used. Finally, the artifact-free calibrated FODS temperature was used for the further analysis in this study. FODS data usually contain artifacts related to the heat exchange between the FO cable and heat sinks or sources other than air, such as precipitation, solar radiation, holders, and support structures.

2.5 Shroud–microstructure approach for determining wind direction using actively heated coned FO cables inside a cylindrical shroud

Actively heating the FO cables and maintaining them warmer than the atmosphere makes them subject to cooling through convective heat flux based on wind speed magnitude and turbulent kinetic energy. Cone-shaped microstructures printed on FO cables cause directional differences in the convective heat loss from the FO cable to the air (shown in Fig. 3, right).

When heated coned fibers are placed in the main flow direction, the fibers in which the cones are aligned with wind flow cool more than in opposite alignment (Fig. 3 left). The microstructure approach uses these directional temperature differences to determine the wind direction. This method was developed and tested in the wind tunnel with Lapo et al. (2020). Subsequently, Freundorfer et al. (2021) successfully deployed this method for measuring horizontal wind direction in their field experiment. This study used the same method to measure the wind direction but in a vertical direction using a cylindrical shroud around coned fibers.

2.6 Coherent structure detection using the quadrant analysis method

Coherent structures in tree canopies are defined as spatially coherent motions generated with vertical wind shear, typically associated with strong vertical motions. Every coherent structure event can be divided into upward and downward motions called ejection and sweep phases (Thomas et al., 2017). This study uses coherent structure events to compare the FODS vertical wind signals against observation. The quadrant analysis method, in combination with hyperbolic thresholding, was used to determine the coherent structures. This method uses a scatterplot of two variables (as horizontal (u') and vertical (w') wind speed perturbation) in a two-dimensional plane in which the coordinate of each flow variable determines the quadrant defined as $Q1(u'>0,\ w'>0)$, $Q2(u'<0,\ w'>0)$, $Q3(u'<0,\ w'<0)$, and $Q4(u'>0,\ w'<0)$. The positive direction of w is upward, and if the azimuth angle of the measurement device is zero, the positive direction of u is eastward. The hyperbolic threshold also defines as $L = u'w'(\sigma_u\sigma_w)^{-1}$, where σ_u and σ_w are horizontal and vertical wind speed standard deviations, which applied to select the events exceeding the specific hole size (Thomas and Foken, 2007). The 20 Hz data of the sonic anemometer placed at 4 m above ground level at the main tower (as described in Sect. 2.1.2) were used to detect the coherent structure. The outliers were removed from sonic anemometer data, dropping the range of the data outer of $\pm 6\sigma$, assuming a normal distribution. Based on the flow statistic in the Waldstein forest, the perturbation timescale of 10 min was used to compute turbulence quantities. The three-dimensional coordinate rotation was applied to compute the fluxes and quadrant analysis (Wilczak et al., 2001). Since the horizontal and vertical wind are decorrelated, the coherent structure events located in $Q2$ having a $|L| > 0.5$ were defined as the ejection phase, and the events located in $Q4$ having $|L| > 0.5$ were defined as the sweep phase (Thomas and Foken, 2007).

2.7 Distributed sensible heat flux using FODS

The sensible heat flux from FODS ($< w' >< T' >$) is the product of instantaneous (e.g., 6 s) vertical wind perturbation ($< w' >$) and 6 s temperature perturbation ($< T' >$), which are defined as $< w' >= < w > - \overline{< w >}$ and $< T' >= < T > - < \overline{T} >$, $<w>$ being the 6 s vertical wind speed calculated using the regression of temperature differences between the upward- and downward-pointing coned fibers and vertical wind speed of the sonic anemometer. $\mathbf{<\overline{< w >}>}$ is the mean of the vertical wind speed over both perturbation timescale (10 min) and length along the fiber (LAF). Similarly, $\mathbf{<\overline{< T >}>}$ is the mean of air temperature observed with bare unheated fibers over both perturbation timescale (10 min) and LAF. We show the averaged instantaneous variables inside $<>$, spatially averaged variables with $\mathbf{<>}$, and averaged over time with an overbar. Sensible heat flux from FODS ($< w' >< T' >$) is without averaging overbar, since the perturbations from FODS are spatiotemporally averaged perturbations mostly affected by coherent structures, while in the case of eddy covariance fluxes, we use $\overline{w'T_s'}$, since the sonic anemometer perturbations have an inherent physical averaging by its response time. w' and T_s' are vertical wind and sonic temperature perturbations with the original sampling frequency of 20 Hz for the main tower and 10 Hz for the turbulence tower.

3 Results and discussion

3.1 Shroud experiment over grassland

During the shroud experiment at EBG, three experimental setups were tested to compare flow statistics between shrouded and unshrouded sensors (Table 1). At first glance, all of the shroud configurations appear to significantly reduce the vertical wind standard deviation while keeping a good correspondence between σ_w inside and outside the shroud, decreasing during the night and increasing during daytimes (Fig. 4a, b, and c). The scatterplot between the shrouded and unshrouded σ_w shown in Fig. 4d, e, and f confirms a high linear relationship (e.g., $R^2>0.9$). The coefficient of determination (R^2) in setups 2 and 3 with 0.975 and 0.976 reveals that the shroud with a 60 cm diameter reduces the vertical wind standard deviation less than the 1 m diameter shroud. Also, setup 3 is less scattered where the 95 % prediction interval is narrower compared to other setups. A prediction interval is a type of confidence that predicts the value of a new observation based on your existing model (Neter et al., 1996). The root mean square error (RMSE) shown in Table 1 shows the lowest error of 0.01 ms^{-1} for daytime and 0.02 ms^{-1} for nighttime for setup 3. Note that the unrotated wind statistics are used for comparisons, since the reduced horizontal wind speed inside the shroud caused unphysical results when applying coordinate rotation.

Besides vertical wind speed, the total ($U = \sqrt{u^2+v^2+w^2}$) and horizontal wind speeds ($U_\mathrm{H} = \sqrt{u^2+v^2}$) are included in the comparison of setups (Table 1), where u and v are horizontal wind speed and w is vertical wind speed. Setups 1 and 2 reduce U and U_H by 72 % and

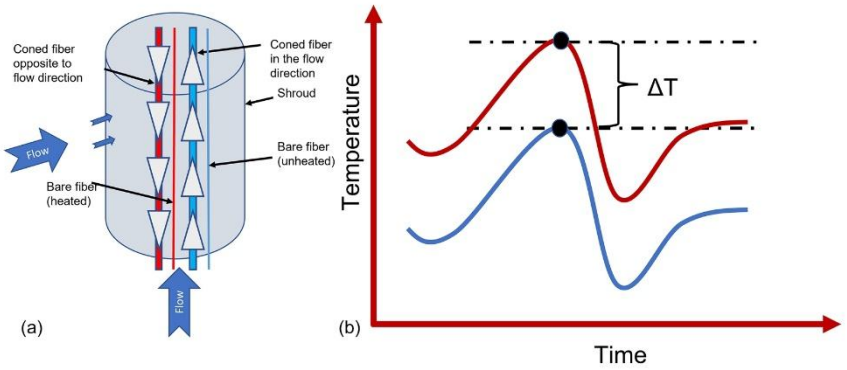

Figure 3. **(a)** Microstructure approach to detecting vertical wind direction using coned FO cables inside the cylindrical shroud. Assuming updraft, the left fiber (indicated in red) would be warmer than the right fiber (shown in blue) due to the cones' direction. **(b)** Microscopic approach – ΔT determined by wind direction.

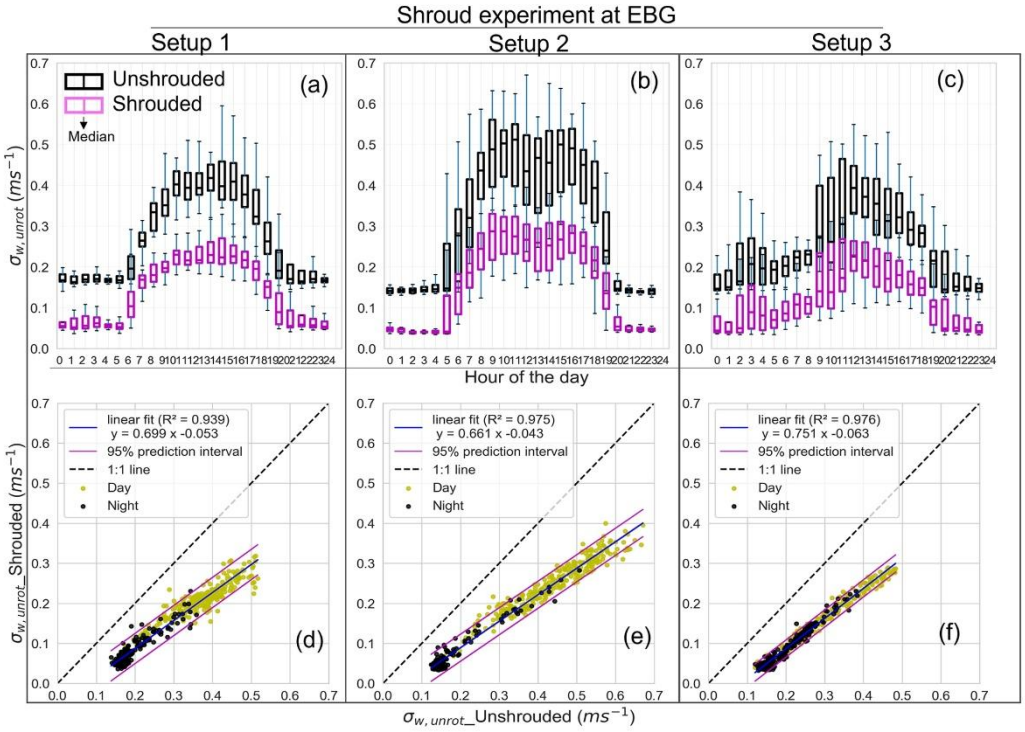

Figure 4. **(a, d)** Diurnal cycle of unrotated vertical wind speed standard deviation ($\sigma_{w,\,\mathrm{unrot}}$) and scatterplots between $\sigma_{w,\,\mathrm{unrot}}$ shrouded and $\sigma_{w,\,\mathrm{unrot}}$ unshrouded for setup 1 of the shroud experiment at EBG. Panels **(b)**, **(e)** and **(c)**, **(f)** show setup 2 and 3, respectively. A 10 min statistic was used to compare the setups. Black and yellow solid points separate night- and daytime. The linear prediction and 95 prediction intervals are shown with solid blue and magenta lines.

Table 1. Coefficient of determination and RMSE between total wind speed, horizontal wind speed standard deviation, and vertical wind standard deviations with and without shroud setup, with N being the number of averaging intervals of 10 min statistic. RP is the reduction percentage of each component within the shroud in comparison to the outside of the shroud. RMSE is calculated between data and the linear fit. The RMSE for each variable is shown in a range referring to the RMSE of daytime and nighttime data. The observational period is 15 April to 15 June 2020.

Statistics	N	Total wind speed (U)			Horizontal wind speed standard deviation ($\sigma_{U_{\mathrm{H,\,unrot}}}$)			$\sigma_{w,\,\mathrm{unrot}}$		
		RP (%)	R^2	RMSE (ms^{-1}) with – without	RP (%)	R^2	RMSE (ms^{-1}) with – without	RP (%)	R^2	RMSE (ms^{-1}) with – without
Setups										
Setup 1 (Gray and dense shroud, 1 m diameter, 1.5 m height, 14 May 2020 to 18 May 2020)	553	73	0.908	0.42–0.55	72	0.952	0.39–0.40	30	0.939	0.014–0.019
Setup 2 (Gray and dense shroud, 60 cm diameter, 1.5 m height, 27 May 2020 to 31 May 2020)	550	74	0.891	0.64–0.46	74	0.955	0.51–0.53	34	0.975	0.018–0.024
Setup 3 (White and not dense shroud, 60 cm diameter, 1.5 m height, 10 June 2020 to 14 June 2020)	552	35	0.911	0.10–0.14	33	0.974	0.09–0.13	25	0.976	0.012–0.017

74 %, which induces a 30 % and 34 % reduction in the vertical wind standard deviation, while in setup 3, the reduction is 35 % for total and horizontal wind speed and 25 % for vertical wind standard deviation. In terms of coefficient of determination and RMSE, the third setup has higher R^2, while having a lower RMSE than the other setups. However, using a 60 cm diameter dense shroud reduces horizontal and vertical wind speed (w) more than the third setup but reduces the goodness of fit between shrouded and unshrouded wind components significantly.

Spectral analysis was performed to compare the shrouded and unshrouded instruments for the third setup to investigate the frequency-specific impacts. Figure 5a and b show that the cylindrical shroud around a sonic anemometer reduces the energy in the integral scales (low frequencies) in both spectra and cospectra. In the inertial subrange, the energy decay slope for both shrouded and unshrouded setups remains mostly $-5/3$ for spectra and $-7/3$ for cospectra, which is consistent with Kolmogorov (1941). It confirms that the shroud has a minimal effect on the isotropic homogenous eddies in the inertial subrange. The significant effect of the shroud can be seen in the high frequencies closer toward the dissipation scales, where the shrouded and unshrouded spectra and cospectra deviate from each other significantly (Fig. 5c, d). The ratios decrease exponentially for high frequencies, which means the shroud dampens the high-frequency eddies extremely. There is a fixed ratio of spectral energy reduction in the low frequencies for temperature and wind components, momentum, and sensible heat flux in both spectral densities. The Pettitt test detected the timescale of the change point at which the spectral energy decreases abruptly. The change points are shown in Fig. 5c, d, with vertical dotted lines for each spectrum varying by approximately 2 and 6 s. It means the eddies smaller than 6 s are highly influenced by the shroud and should be considered in further analysis.

3.2 Shroud experiment in the forest

The third shroud setup from the grassland testing site was identified as the most promising and was subsequently deployed during the LOEWE20 experiment in the forest around coned FO cables to evaluate if the vertical wind component could be observed using a combination of the shroud setup and heated coned fibers. We made one modification to the shroud configuration by increasing the length of the shroud from 1.5 m at EBG to 3 m for the forest environment to account for the minimum resolvable scale; the fiber-optic cable and DTS device used in this experiment is 30 s (Freundorfer et al., 2021). In the preparatory phase of the experiment, our analyses yielded a mean magnitude of the vertical wind speed perturbations of 0.1 ms^{-1} for the Waldstein subcanopy site; hence a shroud length of at least $30\,\mathrm{s} \cdot 0.1\,\mathrm{ms}^{-1} = 3\,\mathrm{m}$ seemed optimal to sample the passing eddies by FODS. The turbulence spectrum in rough forest canopies is dominated by

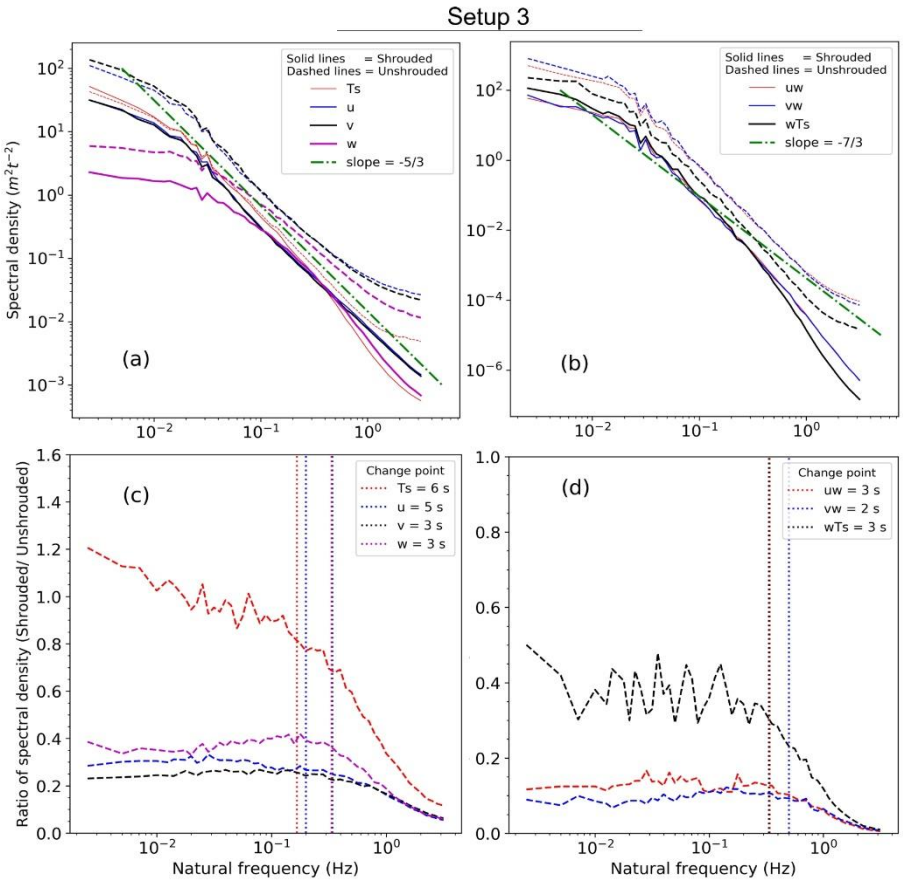

Figure 5. (a) The spectra of the wind speed components and the temperature of setup 3 computed every 10 min and ensemble averaged over the period of 5–14 June 2020; **(b)** the cospectra of the horizontal momentum fluxes, e.g., uw and vw and buoyancy flux, e.g., wT_s for the shrouded and unshrouded setups, and uw and vw are the momentum fluxes aligned with u and v, respectively; **(c)** the ratio of shrouded to unshrouded power spectra; and **(d)** the ratio of shrouded to unshrouded cospectra specifying the change points with vertical dotted lines. The colors used in **(c)** and **(d)** for dashed lines show the same variables in **(a)** and **(b)**. T_s is the sonic temperature, and v is the horizontal wind speed normal to u.

organized turbulent motions resulting in more low-frequency turbulence compared to short-vegetated grasslands; hence the integral length scale is larger. This adjustment seemed necessary to capture the main energy-containing eddies. Figure 6a shows a series of reddish and bluish strips of ΔT within both boxes, most likely induced by stronger updrafts and downdrafts, respectively. The depicted structures outside the shroud are clear and more organized than within the shroud and reflect the vertical air movements better than inside the shroud. Figure 6b magnifies the inside of the shroud, adding instantaneous vertical wind speed to give an idea of how ΔT responds to vertical wind speed change once there is no apparent correlation between the two. The correlation coefficient between ΔT and $w(\rho_w)$ in the main tower is 0.02 inside the shroud but increases to 0.35 outside, demonstrating the substantial increase in correlation between ΔT and w outside the shroud, where the horizontal wind speed in the subcanopy is at its lowest. The ρ_w coefficient further improved when the data subsampled based on rolling five window correlations between ΔT and $w(\rho_{\text{roll}})$ more than 0.8, increasing to 0.53 at the main tower outside the shroud and 0.62 at the turbulence tower.

However, the subsampling significantly improved the correlation outside the shroud for both towers, but no improve-

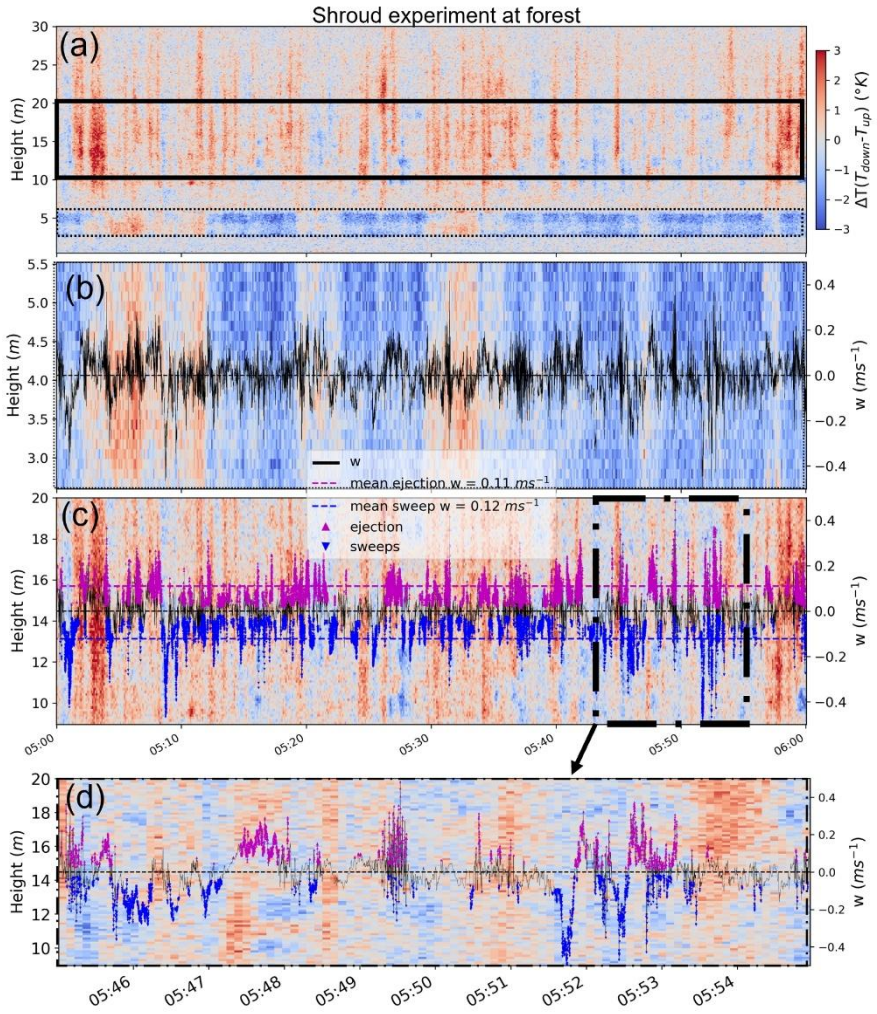

Figure 6. **(a)** Differences in upward-pointing and downward-pointing FODS temperature (ΔT), 6 s time resolution at the main tower during the LOEWE20 experiment on 24 October 2020, 05:00 to 06:00 UTC. The black box with a dashed line shows the location of the shroud installation, and the black box with a solid line shows the comparison section. Panel **(b)** shows the magnified temperature difference inside the shroud containing 2.75–5.75 m above the ground. The solid black line shows the 20 Hz vertical wind speed of the sonic anemometer installed in the middle of the shroud. Panel **(c)** shows the magnified temperature within the solid black box in **(a)**, the height range where the minimum horizontal wind speed occurs in the subcanopy. The magenta upward arrows show the vertical wind during the ejection phase, and the blue downward arrows show the vertical wind during the sweep phase extracted using 20 Hz sampled data at a 4 m height. Panel **(d)** shows the zoomed-in dashed–dotted black box in **(c)**.

ments were made inside the shroud, as shown in Fig. 7a. The ΔT within the shroud does not show a good agreement with vertical wind speed, and the results show the failure of the shroud configurations used in the forest experiment to achieve the research objectives. Potential reasons for the failure of this method can be summarized as follows: (i) the 3 m long shroud might act differently than the 1.5 m shroud to suppress the eddies that are passing through the shroud, and (ii) the percentage of the shroud's horizontal wind reduction is not large enough to keep the horizontal wind speed be-

low the speed observed with coned fibers inside the shroud. (iii) Strong vertical motions resulting from passing coherent structures, which are expected to induce an explicit ΔT at greater heights, may slow down when approaching the ground from above the canopy in the sweep phases and do not accelerate enough at the shroud height during the ejection phase. The findings of Thomas and Foken (2007), who studied flux contributions of coherent structures at this site, support this argument, because sensible heat fluxes are well coupled within the canopy up to a height of $0.72\,h$, h being the canopy, with a relative contribution of nearly 70 %, whereas at lower heights (e.g., $0.29\,h$), the contribution decreases to approximately 40 % due to weakly coupled top and subcanopy.

The analysis of the optimum shroud configuration at the forest failed to observe the sign and magnitude of the vertical wind perturbation using FODS; however, conducting this experiment coincided with an unexpected discovery that the heated coned fibers could observe the coherent structure events in the weak-wind subcanopy outside the shroud within the heights where the minimum horizontal wind speed occurs in the subcanopy. See Fig. S1 in the Supplement for the distributed wind speed profile calculated with FODS for the period of the data used in this study. Figure 6c and d show the mentioned height range together with the sweep and ejection phases, illustrating a good agreement between the positive ΔT with ejection phases and negative ΔT with the sweep phases. The magenta and blue arrows follow the reddish and blueish ΔT's, where higher vertical wind speeds are accompanied by solid features of reddish or blueish stripes, which indicates the duration of coherent structures, while the color intensity might represent the vertical wind speed of motions. In contrast, conditional sampling does not improve the correlation between ΔT and w inside the shroud (Fig. 7a). Note that the sonic anemometer data at a 4 m height were used to compute the correlation coefficients with a section of FODS data at the main tower at 12 to 17 m, adding two sources of uncertainty to the correlation. First, there may be a time lag between two measurements because of height differences, and second, the two heights may not be well coupled, so strong vertical movements of air at a 12–17 m height might dissipate or weaken at 4 m. The mentioned limitation at the main tower is expected to be less at the turbulence tower, since the sonic anemometer is placed at 36 m above the canopy level, where there is a robust sensible flux coupling between these two heights based on Thomas and Foken (2007). The scatterplot between ΔT and w shown in Fig. 7b and c confirms a slight positive correlation between ΔT and w with $\rho_w = 0.35$ and 0.36 at the main and turbulence tower for the whole selected period shown in yellow, respectively. This correlation improves under certain situations: for instance, the correlation coefficient increases to 0.53 and 0.62 when conditional subsampling is used based on the rolling five-window correlation of ΔT and $w(\rho_{\text{roll}})$ greater than 0.8 (shown in black in Fig. 7b and c). The best fit for the median of ensembled w over ΔT is the quadratic function for both towers with an R^2 of 0.78 and 0.93 and an RMSE of 0.02 and 0.14 ms^{-1} for the main and turbulence tower. The quadratic relation between w and ΔT is in line with similar equations describing the relation between convective heat loss from the fiber-optic cable and horizontal wind speed, including Sayde et al. (2015) and Van Ramshorst et al. (2020). The linear model is also the second best-fit model to the median points of the ensemble vertical wind speeds over the ΔT with an R^2 of 0.70 and 0.88 and an RMSE of 0.04 and 0.18 for main and turbulence towers (Table 3). The height of the error bar in Fig. 7a and b remains almost the same at different ΔT, but the scatterplots are more scattered in the low ΔT. The horizontal wind speed was found as the main reason for the deteriorating ΔT signal, where the lowest horizontal wind speed shows smaller error bars (Fig. 8a and b). However, the horizontal wind speed of less than 0.3 ms^{-1} at the subcanopy includes a few percent of the data, which were insufficient to separate and analyze the relationships within these periods.

Following the comparison between ΔT and w for a selected 7 h data for both main and turbulence towers, we evaluated the dataset for the percentage of correctly detected vertical wind directions, which is calculated as a fraction of the number of vertical wind directions that were successfully observed using FODS to the number of chosen data (F). A section of 5 m length of FODS ΔT from 12 to 17 m above ground level was selected and compared against sonic anemometer vertical wind direction to compute the F. Table 3 shows F for whole data and when the five-window rolling correlation (ρ_{roll}) between ΔT and w is larger than 0.8. The analyzed data shows 60 % and 63 % F at the main and turbulence towers, respectively, which increases to 71 % and 67 % for $\rho_{\text{roll}} > 0.8$. Since we know the sign of the distributed vertical wind perturbation with a defined F, we can compute the magnitude of the distributed vertical wind speed perturbations from the relationship between vertical wind speed and ΔT with a known correlation coefficient and have distributed air temperature perturbations directly observed from the unheated FO cable across the entire canopy; we computed the distributed sensible heat fluxes ($< w' >< T' >$) solely based on FODS using the linear and quadratic regression between w and ΔT in Fig. 7b and c to compute the vertical wind perturbation ($< w' >$) for the unshrouded section. The distributed heat flux in Fig. 9 is based on a linear regression between $< w >$ and ΔT at the turbulence and main towers, which yields an RMSE of 0.001 and 0.01 Kms^{-1} in comparison with the sonic anemometer's buoyancy heat flux ($\overline{w'T_s'}$). However, the RMSE is lower at the main tower, but the computed flux is independent of observation with a correlation of 0.04, whereas the correlation is 0.26 at the turbulence tower. Despite the many assumptions creating uncertainty in computing distributed sensible heat flux, the range and temporal dynamics of the computed fluxes across techniques match well for this selected period. We observe two

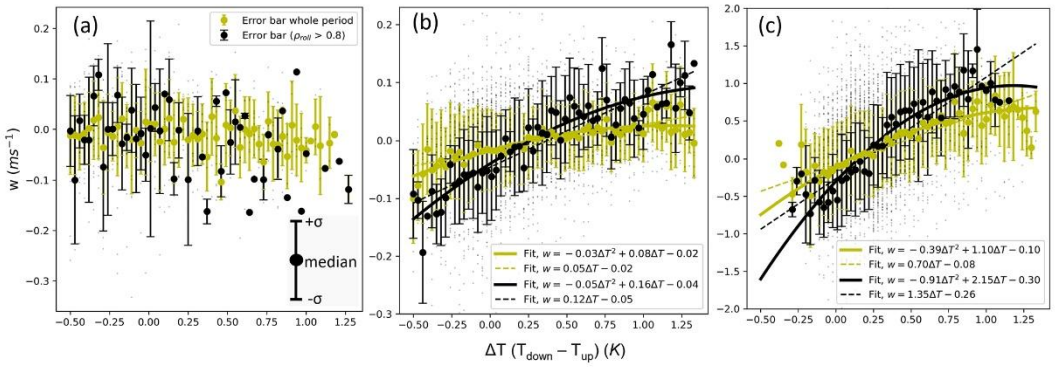

Figure 7. **(a)** Scatterplot between 6 s averaged vertical wind speed ($<w>$) of a sonic anemometer at a 4 m height and ΔT inside the shroud (3–5 m height) for the whole period shown in yellow and subsampled with ρ_{roll}>0.8 with black. The error bars show the median with a solid point with two whiskers at $\pm\sigma$. **(b)** The same scatterplot as **(a)** but outside the shroud at 12–17 m above ground level at the main tower. **(c)** The same scatterplot as **(b)** but for turbulence tower. The error bars are based on the ensemble average of w over ΔT with a bin size of 0.03 °C, and the fit lines are based on the median points for each bin. The data of 24 October 2020, 01:00 to 08:00 UTC, were used to produce the scatterplots. All the data in scatterplots are limited to the 99 % percentile.

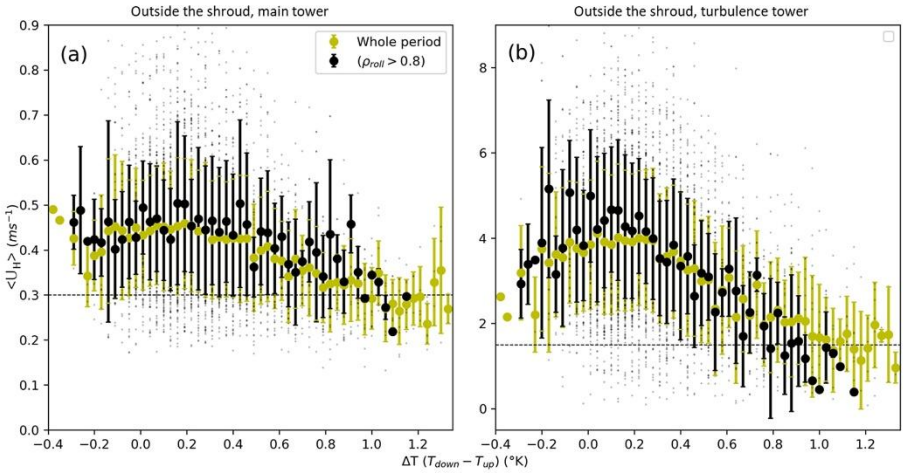

Figure 8. **(a)** Scatterplot between horizontal wind speed computed using FODS and ΔT both averaged at the 12–17 m above ground level at the turbulence tower. **(b)** The same plot as **(a)** but using the wind speed from a sonic anemometer at 36 m. See Fig. 7's caption for the error bar and data information.

areas with distinct differences (Fig. 9): (i) the area near to the ground up to about 7 m where the fluxes are negative and downward; interestingly, the features are more pronounced between 05:00 and 06:00 UTC when the horizontal wind is weaker, and (ii) the height between 9 and 20 m, where the fluxes are often positive and upward, and the features of updrafts are discernible most of the time, since the horizontal wind speed at the mentioned height remains below the threshold ($\sim 0.30\,\text{ms}^{-1}$ Fig. 8a). The comparison also confirms that the computed sensible heat fluxes are in the range of the estimates from classic eddy covariance using sonic anemometry, but, still, the method has some bias in heat flux with an RMSE of 0.01 and 0.0009 Kms^{-1} for the turbulence and main tower, respectively (Fig. 10). As discussed in Sect. 2.7, the fluxes shown as $< w' >< T' >$ and $\overline{w'T_s'}$ in this study are not expected to be identical, as they represent different parts of the forest canopy volume. This first presentation of spatially distributed sensible heat fluxes us-

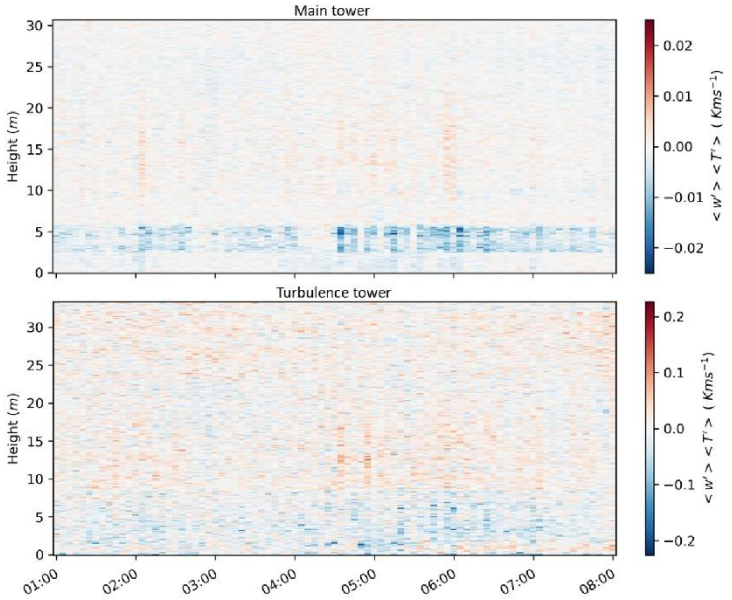

Figure 9. Distributed sensible heat flux estimates from FODS averaged over 5 min at the main and turbulence tower on 24 October 2020, 01:00 to 08:00 UTC. Our approach utilizes a linear regression between ΔT drove from coned fibers and w from a sonic anemometer at 36 m to calculate distributed w. The temperature of unheated bare fiber is used as distributed air temperature.

Table 2. Coefficient of determination (R^2) and RMSE between quadratic and linear fit on the median points at Fig. 7 for the whole period and $\rho_{roll}>0.8$, ρ_{roll} being the rolling correlations between ΔT and w. The number of data used to compute the R^2 and RMSE was $N = 62$ for all cases. The same data as Fig. 7 were used for computation.

	Main tower whole period	Main tower $\rho_{roll}>0.8$	Turbulence tower whole period	Turbulence tower $\rho_{roll}>0.8$
R^2, linear model	0.70	0.82	0.88	0.86
RMSE (ms^{-1})	0.044	0.032	0.184	0.412
R^2, quadratic model	0.78	0.85	0.93	0.92
RMSE (ms^{-1})	0.017	0.055	0.14	0.316

ing FODS solely reinforces the utility of the microstructure approach to directly observe vertical wind component with higher accuracy.

4 Conclusions

This study examined the potential of a physical shroud constructed around heated and unheated fiber-optic cables to overcome the limitations of the microstructure approach caused by the much stronger horizontal wind speed to observe the distributed vertical wind component from FODS. We arrive at the following conclusions:

i Comparison between different shrouds in shape, color, rigidity, and porosity suggested that the white shroud with a 0.60 m diameter is the optimum shroud suitable for filtering the horizontal wind speed by 35 % while having minimal effect on vertical wind speed.

ii The spectral analysis between shrouded and unshrouded setups showed a significant energy reduction dissipation range. This reduction is minor in the inertial subrange, and both shrouded and unshrouded spectra obey the energy decay law. The spectra ratio between shrouded and unshrouded setups revealed that the eddies smaller than 6 s are extremely damped within the shroud.

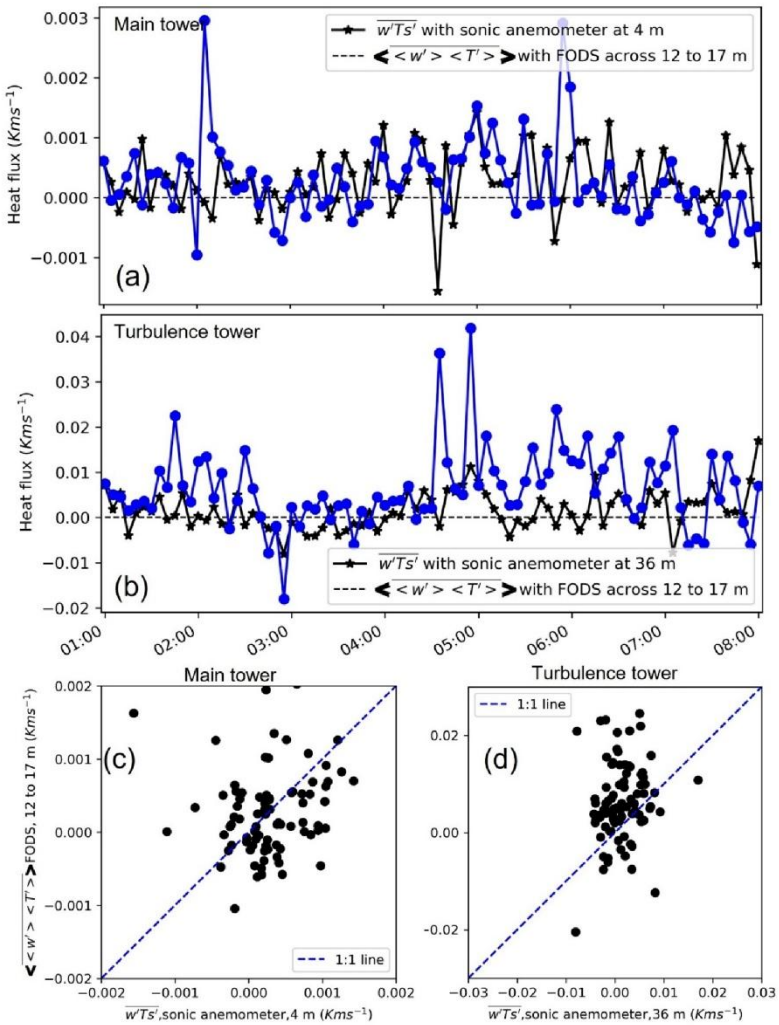

Figure 10. (a, b) Time series and **(c, d)** scatterplot of the sensible heat fluxes observed with the sonic anemometer and from FODS for heights between 12 and 17 m, which is the height where the horizontal wind speed is minimum.

iii Validating the promising shroud setup by adding heated coned fibers inside showed that the shroud fails to keep the vertical wind signal. This failure could be because (i) the shroud does not reduce the horizontal wind speed below the threshold so that the coned fibers can sense the signal. (ii) The shroud's increased length to 3 m changes the behavior of the shroud against the eddies in comparison with a 1.5 m shroud and causes suppression of the eddies that are dominant at the shroud height. (iii) The shroud installation height is not dominant with the same strong, coherent structures as the comparison section (12–17 m).

iv In contrast, evaluation of FODS observations from unshrouded paired coned and heated and unheated FO cables revealed that there is a height range in the subcanopy (12–17 m) where the ΔT from coned fibers show good agreement to sonic anemometer observations. This agreement is more significant during the ver-

tical air movement of coherent structures (e.g., sweep and ejection phases). Within the mentioned height range, the heated coned fiber is capable of detecting the vertical wind direction at least 60 % of the time. The vertical wind speed also has a correlation of 0.35 with the temperature difference between up- and down-pointing fibers, which improves up to 0.62 with conditional sampling.

v The distributed sensible heat flux was computed using the linear and quadratic regression of ΔT and w. Nonetheless, the distributed sensible heat flux seems within the plausible range of the measured fluxes with eddy covariance but still needs improvement. The spatial structure of the distributed sensible heat flux shows explicit information about flux distribution along with the canopy height and changing the sign of the flux at about a 7 m height. This study could be followed with further improvements by adjusting the cone shape and size to increase the correlation of ΔT and vertical wind direction and wind speed. Additionally, deploying DTS instruments with a high signal-to-noise ratio (SNR) and an FO cable with a low response time would lower the uncertainty.

vi This observational achievement is an important step toward developing a FODS-based flux sensor capable of resolving heat flux continuously across spatial and temporal scales.

Data availability. The dataset is available on Zenodo: https://doi.org/10.5281/zenodo.6913436 (Abdoli et al., 2022).

Supplement. The supplement related to this article is available online at: https://doi.org/10.5194/amt-16-809-2023-supplement.

Author contributions. Conceptualization: MA, KL, CKT; methodology and manufacturing: MA, CKT, KL, JS, and JO; field data collection: MA, KL, and JS; validation: MA; formal analysis: MA; investigation: MA and CKT; data curation: MA; writing – original draft preparation: MA; writing – review and editing: all authors; visualization: MA; project administration: CKT and MA; funding acquisition: CKT. All authors have read and agreed to the published version of the paper.

Competing interests. The contact author has declared that none of the authors has any competing interests.

Disclaimer. Publisher's note: Copernicus Publications remains neutral with regard to jurisdictional claims in published maps and institutional affiliations.

Financial support. This research has been supported by the European Research Council, H2020 European Research Council (DarkMix (grant no. 724629)).

This open-access publication was funded by the University of Bayreuth.

Review statement. This paper was edited by Cléo Quaresma Dias-Junior and reviewed by three anonymous referees.

References

Abdoli, M., Lapo, K., Schneider, J., Johannes, and Thomas, C.: Shroud Experiment 2020 (Version 1.0), Zenodo [data set], https://doi.org/10.5281/ZENODO.6913436, 2022.

Anfossi, D., Oettl, D., Degrazia, G., and Goulart, A.: An analysis of sonic anemometer observations in low wind speed conditions, Bound.-Lay. Meteorol., 114, 179–203, https://doi.org/10.1007/s10546-004-1984-4, 2005.

Brunet, Y.: Turbulent Flow in Plant Canopies: Historical Perspective and Overview, Bound.-Lay. Meteorol., 177, 315–364, https://doi.org/10.1007/S10546-020-00560-7, 2020.

Burgers, J. M.: A Mathematical Model Illustrating the Theory of Turbulence, Adv. Appl. Mech., 1, 171–199, https://doi.org/10.1016/S0065-2156(08)70100-5, 1948.

Cheng, Y., Sayde, C., Li, Q., Basara, J., Selker, J., Tanner, E., and Gentine, P.: Failure of Taylor's hypothesis in the atmospheric surface layer and its correction for eddy-covariance measurements, Geophys. Res. Lett., 44, 4287–4295, https://doi.org/10.1002/2017GL073499, 2017.

Corrsin, S.: Turbulent Flow, Am. Sci., 49, 300–325, 1961.

Engelmann, C. and Bernhofer, C.: Exploring Eddy-Covariance Measurements Using a Spatial Approach: The Eddy Matrix, Boundary-Layer Meteorol., 161, 1–17, https://doi.org/10.1007/s10546-016-0161-x, 2016.

Foken, T., Serafimovich, A., Eder, F., Hübner, J., Gao, Z., and Liu, H.: Energy and Matter Fluxes of a Spruce Forest Ecosystem, 229, 309–329, 2017.

Foken, T., Babel, W., Munger, J. W., Grönholm, T., Vesala, T., and Knohl, A.: Selected breakpoints of net forest carbon uptake at four eddy-covariance sites, Stock. Uni Press, 73, 1–12, https://doi.org/10.1080/16000889.2021.1915648, 2021.

Freundorfer, A., Lapo, K., Schneider, J., and Thomas, C. K.: Distributed sensing of wind direction using fiber-optic cables, J. Atmos. Ocean. Technol., 38, 1871–1883, https://doi.org/10.1175/jtech-d-21-0019.1, 2021.

Fritz, A. M., Lapo, K., Freundorfer, A., Linhardt, T., and Thomas, C. K.: Revealing the Morning Transition in the Mountain Boundary Layer Using Fiber-Optic Distributed Temperature Sensing, Geophys. Res. Lett., 48, 1–11, https://doi.org/10.1029/2020GL092238, 2021.

Grachev, A. A., Andreas, E. L., Fairall, C. W., Guest, P. S., and Persson, P. O. G.: The Critical Richardson Number and Limits of Applicability of Local Similarity Theory in the Stable Boundary Layer, Bound.-Lay. Meteorol., 147, 51–82, https://doi.org/10.1007/s10546-012-9771-0, 2013.

Kolmogorov, A. N.: Energy dissipation in locally isotropic turbulence, Dokl. Akad. Nauk. SSSR, 32, 19–21, 1941.

Lapo, K. and Freundorfer, A.: klapo/pyfocs v0.5, Zenodo [code], https://doi.org/10.5281/ZENODO.4292491, 26 November 2020.

Lapo, K., Freundorfer, A., Pfister, L., Schneider, J., Selker, J., and Thomas, C.: Distributed observations of wind direction using microstructures attached to actively heated fiber-optic cables, Atmos. Meas. Tech., 13, 1563–1573, https://doi.org/10.5194/amt-13-1563-2020, 2020.

Liang, J., Zhang, L., Wang, Y., Cao, X., Zhang, Q., Wang, H., and Zhang, B.: Turbulence regimes and the validity of similarity theory in the stable boundary layer over complex terrain of the Loess Plateau, China, Wiley Online Libr., 119, 6009–6021, https://doi.org/10.1002/2014JD021510, 2014.

Mahrt, L., Thomas, C., Richardson, S., Seaman, N., Stauffer, D., and Zeeman, M.: Non-stationary Generation of Weak Turbulence for Very Stable and Weak-Wind Conditions, Bound.-Lay. Meteorol., 147, 179–199, https://doi.org/10.1007/s10546-012-9782-x, 2013.

Neter, J., Kutner, M., Nachtsheim, C., and Wasserman, W.: Applied linear statistical models, ISBN 13 9780256117363, 1996.

Pettitt, A. N.: A Non-Parametric Approach to the Change-Point Problem, J. R. Stat. Soc. Ser. C, 28, 126–135, https://doi.org/10.2307/2346729, 1979.

Pfister, L., Lapo, K., Mahrt, L., and Thomas, C. K.: Thermal Submeso Motions in the Nocturnal Stable Boundary Layer. Part 2: Generating Mechanisms and Implications, Boundary-Layer Meteorol., 180, 203–224, https://doi.org/10.1007/s10546-021-00619-z, 2021.

Predosa, R.: Lasers in the Sky: Distributed Temperature Sensing and a Micro-Meteorological Approach to Quantifying Evapotranspiration, https://ir.library.oregonstate.edu/concern/graduate_thesis_or_dissertations/hx11xm175?locale=en (last access: 28 January 2017), 17 June 2016.

Sayde, C., Thomas, C. K., Wagner, J., and Selker, J.: High-resolution wind speed measurements using actively heated fiber optics, Geophys. Res. Lett., 42, 10064–10073, https://doi.org/10.1002/2015GL066729, 2015.

Schilperoort, B., Coenders-Gerrits, M., Jiménez Rodríguez, C., van der Tol, C., van de Wiel, B., and Savenije, H.: Decoupling of a Douglas fir canopy: a look into the subcanopy with continuous vertical temperature profiles, Biogeosciences, 17, 6423–6439, https://doi.org/10.5194/bg-17-6423-2020, 2020.

Sun, J., Mahrt, L., Banta, R. M., and Pichugina, Y. L.: Turbulence regimes and turbulence intermittency in the stable boundary layer: During CASES-99, J. Atmos. Sci., 69, 338–351, https://doi.org/10.1175/JAS-D-11-082.1, 2012.

Tennekes, H., Lumley, J., and Lumley, J.: A first course in turbulence, The MIT Press, https://doi.org/10.7551/mitpress/3014.001.0001, 1972.

Thomas, C. and Foken, T.: Flux contribution of coherent structures and its implications for the exchange of energy and matter in a tall spruce canopy, Bound.-Lay. Meteorol., 123, 317–337, https://doi.org/10.1007/s10546-006-9144-7, 2007.

Thomas, C. K.: Variability of Sub-Canopy Flow, Temperature, and Horizontal Advection in Moderately Complex Terrain, Bound.-Lay. Meteorol., 139, 61–81, https://doi.org/10.1007/s10546-010-9578-9, 2011.

Thomas, C. K. and Selker, J.: Optical Fiber-Based Distributed Sensing Methods, Springer Handbooks, 611–633, https://doi.org/10.1007/978-3-030-52171-4_20, 2021.

Thomas, C. K., Law, B. E., Irvine, J., Martin, J. G., Pettijohn, J. C., Davis, K. J., Thomas, C.:, Law, B. E., Irvine, J., Martin, J. G., Pettijohn, J. C., and Davis, K. J.: Seasonal hydrology explains interannual and seasonal variation in carbon and water exchange in a semiarid mature ponderosa pine forest in central Oregon, J. Geophys. Res.-Biogeo., 114, 4006, https://doi.org/10.1029/2009JG001010, 2009.

Thomas, C. K., Kennedy, A. M., Selker, J. S., Moretti, A., Schroth, M. H., Smoot, A. R., Tufillaro, N. B., and Zeeman, M. J.: High-Resolution Fibre-Optic Temperature Sensing: A New Tool to Study the Two-Dimensional Structure of Atmospheric Surface-Layer Flow, Bound.-Lay. Meteorol., 142, 177–192, https://doi.org/10.1007/s10546-011-9672-7, 2012.

Thomas, C. K., Serafimovich, A., Siebicke, L., Gerken, T., and Foken, T.: Coherent Structures and Flux Coupling BT – Energy and Matter Fluxes of a Spruce Forest Ecosystem, edited by: Foken, T., Springer International Publishing, Cham, 113–135, https://doi.org/10.1007/978-3-319-49389-3_6, 2017.

Thomas, C. K., Huss, J. M., Abdoli, M., Huttarsch, T., and Schneider, J.: Solid-Phase Reference Baths for Fiber-Optic Distributed Sensing, Sensors, 22, https://doi.org/10.3390/s22114244, 2022.

van de Giesen, N., Steele-Dunne, S. C., Jansen, J., Hoes, O., Hausner, M. B., Tyler, S., and Selker, J.: Double-Ended Calibration of Fiber-Optic Raman Spectra Distributed Temperature Sensing Data, Sensors, 12, 5471–5485, https://doi.org/10.3390/S120505471, 2012.

Van de Wiel, B. J. H., Moene, A. F., Jonker, H. J. J., Baas, P., Basu, S., Donda, J. M. M., Sun, J., and Holtslag, A. A. M.: The minimum wind speed for sustainable turbulence in the nocturnal boundary layer, J. Atmos. Sci., 69, 3116–3127, https://doi.org/10.1175/JAS-D-12-0107.1, 2012.

van Ramshorst, J. G. V., Coenders-Gerrits, M., Schilperoort, B., van de Wiel, B. J. H., Izett, J. G., Selker, J. S., Higgins, C. W., Savenije, H. H. G., and van de Giesen, N. C.: Revisiting wind speed measurements using actively heated fiber optics: a wind tunnel study, Atmos. Meas. Tech., 13, 5423–5439, https://doi.org/10.5194/amt-13-5423-2020, 2020.

Vickers, D. and Thomas, C. K.: Observations of the scale-dependent turbulence and evaluation of the flux–gradient relationship for sensible heat for a closed Douglas-fir canopy in very weak wind conditions, Atmos. Chem. Phys., 14, 9665–9676, https://doi.org/10.5194/acp-14-9665-2014, 2014.

Wilczak, J. M., Oncley, S. P., and Stage, S. A.: Sonic Anemometer Tilt Correction Algorithms, Bound.-Lay. Meteorol., 99, 127–150, https://doi.org/10.1023/A:1018966204465, 2001.

Zarenistanak, M., Dhorde, A. G., and Kripalani, R. H.: Trend analysis and change point detection of annual and seasonal precipitation and temperature series over southwest Iran, J. Earth Syst. Sci., 123, 281–295, https://doi.org/10.1007/s12040-013-0395-7, 2014.

Paper II

Improving turbulent airflow direction measurements for fiber-optic distributed sensing using numerical simulations

Status: Published (2025)
Journal: Atmospheric Measurement Techniques
doi: https://doi.org/10.5194/amt-18-6417-2025

Atmos. Meas. Tech., 18, 6417–6433, 2025
https://doi.org/10.5194/amt-18-6417-2025

Atmospheric Measurement Techniques
Open Access
EGU

Improving turbulent airflow direction measurements for fiber-optic distributed sensing using numerical simulations

Mohammad Abdoli[1,2], **Reza Pirkhoshghiyafeh**[3], **and Christoph K. Thomas**[1,4]

[1]Micrometeorology Group, University of Bayreuth, Universitätsstraße, 95447 Bayreuth, Germany
[2]Physical Geography and Climatology, RWTH Aachen University, Wüllnerstraße 5b, 52062 Aachen, Germany
[3]School of Mechanical Engineering, University of Tabriz, Bahman Boulevard 29, 5165665931 Tabriz, Iran
[4]Bayreuth Center for Ecology and Environmental Research (BayCEER), University of Bayreuth, Universitätsstraße, 95447 Bayreuth, Germany

Correspondence: Mohammad Abdoli (mohammad.abdoli@geo.rwth-aachen.de)

Received: 18 May 2025 – Discussion started: 4 July 2025
Revised: 16 September 2025 – Accepted: 7 October 2025 – Published: 12 November 2025

Abstract. This study investigates the impact of microstructure geometry on the thermal and turbulence responses of electrically heated fiber-optic (FO) cables under varying flow conditions and turbulence intensities for the purposes of sensing flow direction. The underlying measurement principle is the directionally sensitive heat loss from electrically heated FO cables with imprinted microstructures exposed to turbulent airflows resembling a long hot-wire anemometer. Using the COMSOL Multiphysics 6.0 finite-element software, this study explores a wider range of different configurations of filled-coned and hollow-coned microstructures of varying size compared to existing studies. The research identifies optimal combinations which maximize temperature differences (ΔT) across FO cables with cones pointing in opposite directions while balancing key design criteria such as sensitivity to wind speed and minimizing the FO-cables' PVC coverage. We demonstrate that FO cables with hollow-coned microstructures (radius = 24 mm, height = 24 mm, and spacing = 15 mm) outperform their filled-coned counterparts, maintaining ΔT values above 2 K across a broader range of wind speeds and turbulence intensities. Notably, the hollow-cone configuration sustains a temperature difference of up to 0.8 K at a 60° wind attack angle. The findings implicate substantial improvements for an optimized FO cable design in atmospheric boundary layer studies, enabling more accurate measurements of wind direction, distributed turbulent heat fluxes, and vertical wind speed perturbations using fiber-optic distributed sensing (FODS). Future work shall validate the findings under field conditions to assess the robustness and real-world applicability of the optimized design.

1 Introduction

Distributed temperature sensing (DTS) uses fiber-optic (FO) cable to measure temperature in continuous, defined sections along FO cables. DTS measurements involve sending a laser pulse into the FO cable, where parts of it are reflected. While most optical energy undergoes elastic scattering maintaining the original wavelength, some is absorbed and re-emitted at different wavelengths, known as inelastic Raman backscatter. The longer wavelength backscatter, called Stokes, has a nearly temperature-independent amplitude. The shorter wavelength backscatter, known as Anti-Stokes, has an amplitude which varies with temperature. By measuring the natural logarithm of the ratio of Stokes to Anti-Stokes backscatter averaged over continuous sections of the FO cable by means of range-gating, the temperature along the entire cable can be spatially resolved (Ukil et al., 2012; Selker et al., 2006; Thomas and Selker, 2021). Since their development in the 1980s, DTS technology has advanced significantly, enabling continuous temperature measurements with a resolution of 0.01 °C and spatial resolutions as fine as a few meters or even decimeters. These sensors have been widely used in various applications, including dam structural health monitoring (SHM) (Bado, 2021), pipelines, tunnels (Ishii et al., 1997), offshore oil and gas

Published by Copernicus Publications on behalf of the European Geosciences Union.

installations (Nakstad and Kringlebotn, 2008; Johny et al., 2021), mines (Silva et al., 2022), and also in research areas such as hydrological investigations (Selker et al., 2006; Tyler et al., 2009; Bense et al., 2016; Taniguchi, 1993), soil moisture measurements (Steele-Dunne et al., 2010), and atmospheric measurements of turbulence and air temperature (Thomas et al., 2012; Keller et al., 2011; Peltola et al., 2021; des Tombe et al., 2020; Higgins et al., 2018; de Jong et al., 2015; Fritz et al., 2021). Using fiber-optic distributed sensing (FODS) in atmospheric measurement has gained more attention in the study of the stable boundary layer, particularly because the turbulence dynamics in stable and very stable boundary layers are only insufficiently captured by conventional point-based sensors in combination with theoretical frameworks such as the Monin–Obukhov similarity theory, the Kolmogorov spectrum, and Taylor's hypothesis of frozen turbulence (Sun et al., 2012). High-resolution FODS has emerged as a powerful tool for probing the stable boundary layer and unraveling its underlying physical processes since it enables the simultaneous spatiotemporal observation of key atmospheric parameters such as temperature, wind speed, and wind direction. In this context, Zeeman et al. (2015) explored the thermal structure of near-surface motions in the nocturnal boundary layer using FODS, revealing detailed temperature structures under stable conditions, including gradients and intermittent patterns at the meter scale. Huss and Thomas (2024) examined the efficiency of vertical heat transport and the coupling mechanisms governing turbulence in the stable boundary layer (SBL). Utilizing data from sonic anemometers and FODS, the study identified appropriate modeling approaches for quantifying turbulent surface heat flux under stable conditions. Furthermore, Pfister et al. (2021a, b) detected semi-stationary thermal submesofronts in the nocturnal boundary layer using FODS, while Mack et al. (2025) utilized airborne FODS during the Arctic polar night to capture key features of the SBL, which were then compared against the HARMONIE-AROME model.

The development of wind speed measurement method using FODS (Sayde et al., 2015; van Ramshorst et al., 2020) has opened new insights into the application of FODS in continuous wind speed measurement, suggesting that this method could be used to spatially resolve turbulence. In 2019, the Darkmix project aimed at developing a 3D large eddy observation (LEO) technique using DTS with the goal of investigate the weak-wind and stable boundary layer across different land uses, including grassland, forest, and urban areas (Lapo et al., 2022). Within this project, Lapo et al. (2020) developed a method known as the "microstructure approach," which uses Computational Fluid Dynamics (CFD) modeling in concert with wind tunnel experiments to determine turbulent wind direction and speed using actively heated FO cables with imprinted filled-coned microstructures. This method employs the difference in convective heat loss from the filled-coned fibers when the wind flows along the direction of the cones compared to a cable with cones pointing in the opposite direction.

The principle behind using microstructures for sensing the wind speed and wind direction builds on convective heat transfer theory and is conceptually related to hot-wire anemometry (Sayde et al., 2015; van Ramshorst et al., 2020). When the fiber is heated above ambient air temperature, the cooling rate depends on the turbulent heat flux from the cable surface to the air, which scales with wind speed. By introducing asymmetric microstructures onto paired cables, oriented in opposite directions, the effective aerodynamic roughness of the surfaces is altered. This geometric asymmetry modifies the convective heat loss experienced by each cable. According to Owen and Thomson (1963), the convective heat flux from a roughened surface depends on air density, the specific heat of air, air–surface temperature difference, friction velocity, the effective roughness height, kinematic viscosity, and the Prandtl number. The orientation of the microstructures directly affects the effective roughness: cones aligned with the flow increase roughness, enhancing turbulent mixing and convective cooling, while cones pointing into the flow reduce roughness and suppress heat loss. This asymmetry in convective heat transfer produces a measurable temperature difference between paired cables. The sign of this temperature difference provides a robust signal for determining wind direction, and the magnitude of the temperature difference correlates with the wind speed.

This method was successfully tested in a field experiment by Freundorfer et al. (2021), where the wind direction was calculated using FODS and the accuracy of $\leq 15°$. Subsequently, Abdoli et al. (2023) attempted to compute continuous turbulent vertical airflow and air temperature perturbations to compute the spatially resolved sensible heat flux within a forest subcanopy using FODS and the microstructure approach and compared it with eddy covariance observations. In this study, the vertical wind speed was calculated using the differential heat loss approach described above, which demonstrated the potential of the microstructure approach to not only observe the wind direction but also measure the wind speed along the fiber. Nevertheless, this was only effective in weak-wind conditions with speeds typically less than $2\,\mathrm{m\,s^{-1}}$. One significant limitation of this methodology was the geometry of the microstructures printed onto the cable characterized by a high sensitivity of the vertically pointing heated and filled-coned FO cables to lateral wind speeds orthogonal to the cable, which resulted in the method becoming ineffective at horizontal wind speeds exceeding $0.2\,\mathrm{m\,s^{-1}}$. Despite these limitations, the effort demonstrated the considerable potential of the microstructure approach to observe turbulent airflow. However, further refinements are necessary to enhance its accuracy and performance in real-world turbulent flows. Furthermore, in the proof-of-concept study on the microstructure approach (Lapo et al., 2020), the selection of microstructure form, shape, size, and spacing was based on a limited set of combinations. The selection

was made exclusively on the basis of modeling the turbulence around the microstructures, and not modeling the heat transfer explicitly. We here test a much broader range of microstructure forms, shapes, sizes, and spacing combinations beyond those tested by Lapo et al. (2020) with incorporated heat exchange simulation added to the model bears the potential to improve the utility of this approach in sensing the turbulent flow direction.

In this numerical study, we aim at overcoming the major weaknesses of the existing microstructure approach to enhance wind speed and direction measurements using filled-coned FO cables while minimizing their sensitivity to lateral wind flows. The microstructures considered include filled-coned (similar to the one used in Lapo et al., 2020) for comparison with the previous numerical study and hollow-coned. The hollow-coned microstructure is selected to decrease the fiber's sensitivity to lateral airflows and reduce the fiber length covered with microstructures, which in turn increases its sensitivity to the heat loss and hence temperature difference. The tested microstructures vary in combinations of radius, height, and spacing, with a focus on turbulence and conjugate heat transfer. Our primary objective is to improve the temperature difference between the forward (wind directed towards the cone apex) and backward (wind opposite to the cone apex) coned fibers. A larger temperature difference between the forward and backward fibers ensures that the signal exceeds the measurement error 0 to 0.1 K reported by (Schilperoort et al., 2020). It therefore enhances the precision of the microstructure approach at higher wind speed ranges and increasing the persistence of the temperature difference under lateral wind conditions. Additionally, we aim at examining the sensitivity of the temperature difference for the most promising configurations to turbulence intensity (TI) and wind attack angle to increase the microstructure's utility for real-world turbulence flow sensing applications characterized by a large degree of space and time variability in magnitude, direction, and strength. The following section describe the modeling approach. All abbreviations used in this study are summarized in Appendix A, Table A1.

2 Materials and Methods

This study employed the finite-element software COMSOL Multiphysics 6.0 to simulate heat transfer and fluid flow around two distinct microstructure designs, a filled-coned and a hollow-coned structure attached to a thin fiber optic (FO) cable. The use of COMSOL for coupled heat transfer and fluid–solid interaction problems has been widely validated in similar studies (Chen et al., 2023; Sogukpinar, 2020; Sun et al., 2024; Ma et al., 2025; Kalantari et al., 2021). In particular, Chen et al. (2023) and Kalantari et al. (2021) specifically employed the K–ϵ turbulence model to heat-transfer simulations focusing on the thermal environment of a high geothermal tunnel and the heat transfer of fin-and-tube heat exchangers, respectively, thereby reinforcing the suitability of our selected model for the present study.

The modeling was conducted using incompressible air, with the study type set to stationary. All computations were executed on a desktop computer equipped with an Intel(R) Core(TM) i7-8700 CPU (3.20 GHz) and 64 GB of RAM. Figure 1 illustrates the schematic of the filled-coned microstructures attached to a FO cables. The computational domain was determined parametrically to locate six microstructures in length. The height was determined to be $16r$, with r being the radius of the cone. The separation distance between the forward and backward FO cables was determined to be $8r$. The dimensions were selected and optimized with several test runs to maintain accuracy and reduce computational costs. Solid copper was used as the FO cable material, and polyvinyl chloride (PVC) was chosen for the microstructures, and gas form air was used for the rest volume of the model. It is important to note that FO cables currently used in atmospheric measurements typically consist of a stainless steel sheath filled with gel, encased in a polyethylene (PE) layer which has about a 1s effective response time (Thomas et al., 2012). In this study, solid copper was used as a substitute to simplify the model and focus on the geometry of the microstructures rather than the properties of FO-cable. These materials were selected from COMSOL's built-in library, which includes all standard properties such as dynamic viscosity, heat capacity at constant pressure, density, and thermal conductivity.

The K–ϵ turbulence model was used to simulate the turbulence while the 'Heat Transfer in Solids and Fluids' module was employed for modeling the heat transfer between the conical fiber and the surrounding air. The K–ϵ model, first introduced by Launder and Sharma (1974), is one of the most widely applied turbulence models. It solves two transport equations for the turbulent kinetic energy (K) and its dissipation rate (ϵ), from which the turbulent viscosity is derived. While the model is numerically robust and computationally efficient for fully developed turbulent shear flows, its formulation is based on the assumption of isotropic turbulence and employs empirical constants as well as wall functions. These limitations reduce its accuracy in complex flow conditions, particularly in the presence of adverse pressure gradients, rotation, or separation (Puntigam et al., 2025). Nevertheless, due to the widespread application of this model in turbulence research and to allow comparability with the study of Lapo et al. (2020), we chose to employ the K–ϵ model in this study.

The inlet wind (U_{in}) was applied from left to right as shown in Fig. 1a with the turbulence intensity (TI) set to 0.05, which corresponds to moderate turbulence in the atmospheric boundary layer (Watkins, 2012). The TI is defined as $\frac{\sigma_U}{\overline{U}}$, where σ_U represents the standard deviation of the wind over an average period, and $\overline{U}$ is the total wind speed averaged over the same time period. Figure 1b shows a con-

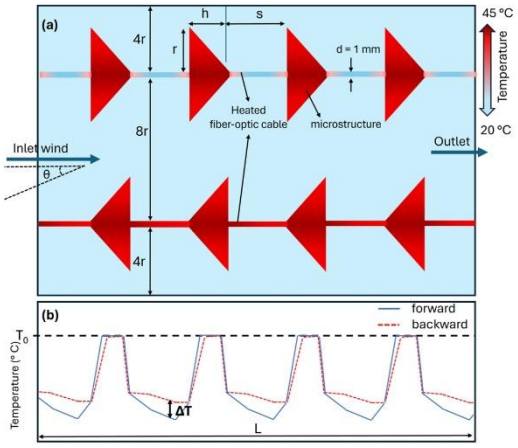

Figure 1. Schematic representing the modeled fiber optic cables featuring filled-coned microstructures. Panel **(a)** illustrates the surface temperature, ambient air temperature, and geometric parameters, while panel **(b)** depicts the conceptual temperature difference between the forward and backward fibers. Here, T_0 represents the temperature at the interface between the microstructure and the fiber optic cable. Forward fibers are those oriented with the wind directed toward the cone apex, whereas backward fibers are oriented with the wind opposing the cone apex.

ceptual schematic of the temperature along the fiber for both forward and backward coned fibers, along with the temperature difference between them. This temperature difference arises from the cone orientation. In forward coned fibers, the flow penetrates the cone openings and enhances cooling of the fiber. In contrast, in backward coned fibers, the cone acts as a shelter that reduces exposure to the flow and thereby lowers the cooling rate. This mechanism underpins the microstructure approach, which generates a directional temperature difference between forward and backward coned fibers. The turbulence length scale is set to built-in function of COMSOL as "based on geometry". To test the sensitivity of the model to TI, a range of 0.01 to 0.4 was applied to the model (Table 1). All boundaries except the inlet and outlet were set to act as a wall. The ambient air temperature of the model was set to 20 °C and the FO cable temperature was set to 45 °C to create a 25 K temperature difference between the FO cable and the ambient air. This temperature difference was selected to align with the range used in previous field experiments (Lapo et al., 2022), where FO cables were heated at a rate of 4.5 W m^{-1}, inducing temperature differences between 4.2 and 31.0 K. In addition, the temperature difference between air and FO cable was chosen to be large enough to prevent excessive cooling within the wind speed range of the modeling. Based on the initial model runs, the inlet wind speed range was varied between 0 and 4.0 m s^{-1} at 0.5 m s^{-1} steps between 0 and 1 m s^{-1}, and 1 m s^{-1} steps for higher wind speeds (Table 1).

Table 1. Model input parameters include: inlet wind speed (U_{in}), wind attacking angle (θ), turbulence intensity (TI), and geometry parameters including the radius (r), height (h), and spacing (s) of the microstructures used in geometry combinations.

Parameters	Range
U_{in} (m s^{-1})	[0, 0.5, 1, 2, 3, 4]
r (mm)	[6, 12, 18, 24]
h (mm)	[6, 12, 18, 24]
s (mm)	[15, 20, 25, 30]
θ (°)	[0, 30, 60, 90]
TI	0.01, 0.05, 0.1, 0.2, 0.3

A physics-controlled mesh, generated by COMSOL Multiphysics to align with the specific settings of the model's physics interface, was employed with a standard element size, as illustrated in Fig. 2. Additional adjustments were applied to the mesh manually to ensure adequate resolution of the boundary-layer profiles and the microstructure edges. Our design ensured that the mesh geometries for the two-dimensional (2D) and three-dimensional (3D) simulations matched perfectly. The first part of the study was done with 2D modeling of 64 different geometry combinations since the model was symmetric and the inlet wind was aligned with the fibers. The 2D modeling is also used to analyze the effects of different turbulence intensity ranges. Finally, the most promising combinations were selected based on the maximum temperature difference within the inlet wind speed range ($\Delta T_{U_{\text{in},0.5}} - \Delta T_{U_{\text{in},4}}$).

In the second part of the study, the most promising configurations of the first part for both filled-coned and hollow-coned were modeled in 3D in a manner analogous to the two-dimensional model, with the addition of an attacking angle ranging from 0 to 90°, as specified in Table 1. Please refer to the 3D schematic shown in Fig. A1. The parametric sweep function was used to run multiple combinations of input parameters simultaneously. In addition to the variable U_{in}, a variable cone radius (r), cone height (h), and spacing (s) were employed to cover 64 geometric combinations. These 64 geometric combinations were executed for all values of U_{in}, and the resulting differences between forward and backward coned fibers in temperature ($\Delta T = T_{\text{b}} - T_{\text{f}}$), turbulent kinetic energy ($\Delta K = K_{\text{b}} - K_{\text{f}}$), and wind speed ($\Delta U = U_{\text{b}} - U_{\text{f}}$) on the fiber were extracted, where the subscripts b and f denote the backward and forward inlet wind, respectively. The temperature is averaged over the surface of the fiber in 2D models and over the volume in 3D models. The turbulent kinetic energy and wind speed were extracted from the surface of the fiber exposed to airflow. The first two microstructures and the three initial spacings from the inlet wind were excluded from the averaging process to exclude

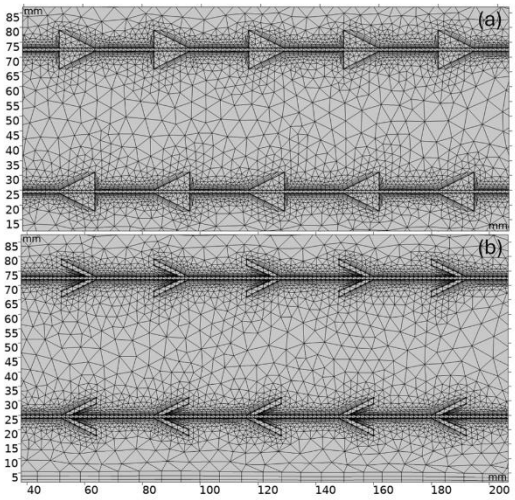

Figure 2. Mesh distribution example of **(a)** filled-coned and **(b)** hollow-coned microstructures.

the instationary transition region, where the flow adjusts to the microstructures, ensuring that only fully developed flow conditions are considered. The averages were obtained using the built-in functions of the COMSOL Multiphysics model and were subsequently analyzed in Python.

The governing physics of the $K-\epsilon$ turbulence model, along with the "Heat Transfer in Solids and Fluids" module employed in this study, are described in detail in the Appendix B. Mesh independence validation is essential to balance computational efficiency with numerical accuracy (Chen et al., 2023). To assess this, we tested four mesh sizes (Mesh A–D) with 9272, 12 202, 14 948, and 19 834 elements, respectively. A 2D model of a hollow-coned geometry ($r = 24$ mm, $h = 24$ mm, $s = 15$ mm) was simulated as an example, and fiber temperatures in forward and backward-oriented FO cables were compared. Figure 3 shows the simulated temperatures for the four mesh sizes. In both orientations, differences among the meshes are minimal. The standard deviation across the meshes remains below 0.4 K at the lowest wind speed and decreases further with increasing wind speed (< 0.1 K at $U_{\text{in}} = 4\,\text{m}\,\text{s}^{-1}$). These results indicate that the solution is effectively mesh-independent, ensuring both computational efficiency and model accuracy.

3 Results and discussion

3.1 Differences in modeled temperature and turbulent kinetic energy

An example of the modeled temperature (T) and turbulent kinetic energy (K) is shown in Fig. 4a and b, respectively. The results indicate that the temperature is lower for the forward fibers, with notably higher temperatures behind the cones in the backward direction. Conversely, K remains lower in the backward cones compared to the forward cones.

FO cables with hollow-coned microstructures exhibit similar behavior to those with filled-coned microstructures, with the backward direction being warmer and the forward direction cooling down (Fig. 5a and b). In filled-cone fibers, the entire cone height is attached to the fiber, whereas in hollow-cone fibers only part of the cone is attached, leaving the fiber in the hollow section exposed to airflow. This reduced PVC attachment in hollow-cone fibers results in less heat transfer within the microstructure itself, so the fiber temperature is less affected by the surrounding material. A longer exposed fiber length additionally results in a shorter thermal response time. In the present study, however, the model was run only until steady-state heat transfer was reached, and the response time was not examined in detail. In contrast, the more PVC material printed on filled-cone fibers, the longer it takes for the fiber temperature to equilibrate with the air temperature, due to PVC's lower thermal conductivity compared to copper or steel. The modeling results confirmed the viability of the fundamental principle behind the microstructure approach in creating a temperature difference between the forward and backward FO cables, which is induced by variations in directional heat loss. The relationship between the temperature difference (ΔT) and the inlet wind speed (U_{in}) in both microstructure types shown in Fig. 6a and b aligns with the findings of Lapo et al. (2020), where ΔT is higher at low wind speeds and decreases non-linearly with increasing inlet wind speed. The comparison of the best-performing microstructure design ($r = 6$ mm, $h = 12$ mm, $s = 20$ mm) reported by Lapo et al. (2020) with the modeled combination illustrated in Fig. 6a shows a R^2 of 0.95, indicating that the model behaves similarly to the wind tunnel experiment (The comparison graph is shown in Appendix A4). Furthermore, in this study, the most promising combinations were selected based on the maximum ($\Delta T_{U_{\text{in},0.5}} - \Delta T_{U_{\text{in},4}}$), which equals 1.15 K in Lapo et al. (2020) and 0.98 K in the model. However, the magnitude of the modeled ΔT in this study differs from the wind tunnel ΔT by an offset of 1.32 K. The following points may explain this discrepancy:

- The simplifications applied to the FO cable in the model. In the wind tunnel experiment, the FO cable consisted of a thin metal sheath filled with jelly and glass cores, while in the model it was simplified as a solid copper bar.

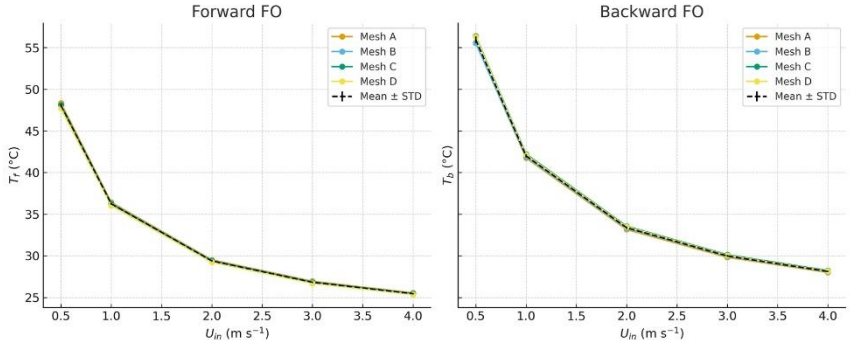

Figure 3. Mesh independence of modeled FO cable temperatures for forward and backward fibers at different inlet wind speeds. STD denotes the standard deviation of the FO cable temperature for different mesh sizes.

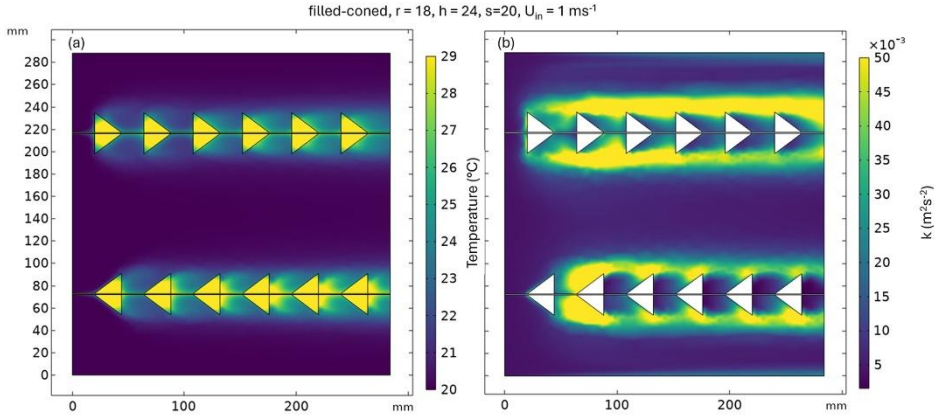

Figure 4. Modeled temperature (T) and turbulent kinetic energy (K) in FO cables and surrounding air with filled-coned microstructures under an inlet wind speed of 1 m s^{-1}.

– Differences in turbulence characteristics between the wind tunnel and the COMSOL model. In wind tunnels, turbulence intensity and scales arise from inflow generation and boundary layer development, whereas in COMSOL the K–ϵ closure with wall functions represents turbulence in an averaged, isotropic way. This difference can reduce the fidelity of convective heat transfer predictions, particularly around small-scale cable structures.

– The difference in FO cable materials also leads to differences in heating rate between the wind tunnel and the model, which can affect the magnitude of ΔT.

Based on the 2D modeling, the four most promising geometric combinations for filled-coned and hollow-coned FO cables were depicted in Fig. 6a and b, which were selected based on the ΔT magnitude between the $U_{\text{in}} = 0.5$ and 4 m s^{-1}, plotted as marked bold lines. For example, the combination of hollow-coned microstructure (radius = 24 mm, height = 24 mm, and spacing = 15 mm) produced a temperature difference ($\Delta T_{U_{\text{in},0.5}} - \Delta T_{U_{\text{in},4}}$) of 4.78 K. The geometry used in the previous study is also added to the plot as a reference. We used ΔT to identify the most promising cone geometry combinations; for completeness, the combinations selected based on ΔK and ΔU are also provided in Appendix Figs. A2 and A3. The filled-coned microstructures are able to induce a temperature difference of 3.57 K at 0.5 m s^{-1} and a ($\Delta T_{U_{\text{in},0.5}} - \Delta T_{U_{\text{in},4}}$) of 2.61 K between 0.5 and 4 m s^{-1} with the geometry parameters of $r = 18$ mm, $h = 24$ mm, and $s = 15$ mm where the hollow-coned combinations reached 7.25 K at 0.5 m s^{-1} and a ($\Delta T_{U_{\text{in},0.5}} - \Delta T_{U_{\text{in},4}}$) of 4.78 K between 0.5 and 4 m s^{-1} with the geometry pa-

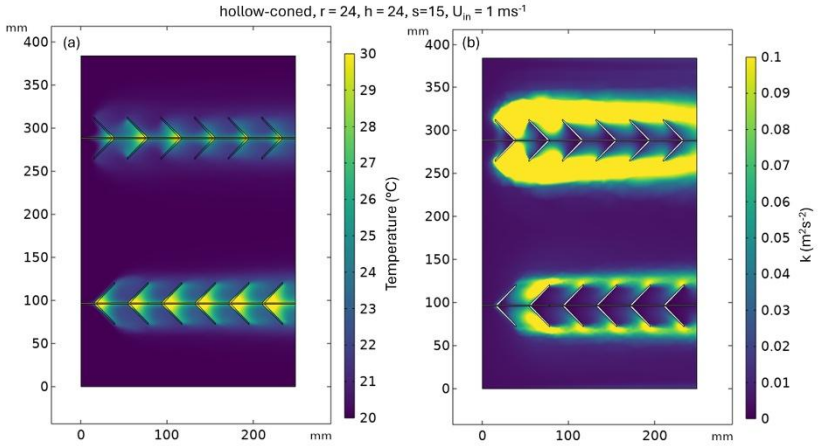

Figure 5. Modeled temperature (T) and turbulent kinetic energy (K) in and around of FO cable with attached hollow-coned microstructures and inlet wind of 1 m s^{-1}.

rameters of $r = 24$ mm, $h = 24$ mm, and $s = 15$ mm (Fig. 6a and b). Both microstructure types show improvement in ΔT magnitude compared to (Lapo et al., 2020). Considering the flow conditions over the FO cables, in filled-coned microstructures, a decrease in turbulent kinetic energy and total wind speed (U) is determined down to -0.21 m^{2}s^{-2} and -0.55 m s^{-1}, respectively, where the top ΔT combinations are not necessarily the ones with the lowest ΔK and ΔU (Fig. 6c and e). The reason is part of the FO cable is covered with PVC microstructures and the heat exchange is a function of the turbulent heat loss as well as the heat transfer within the microstructures. In contrast to filled-coned, the highest ΔT combinations also show a lower ΔK and ΔU of -0.11 m^{2}s^{-2} and -0.21 m s^{-1} in hollow-coned combinations, where a smaller part of the FO cable is covered with microstructures (Fig. 6d and f). Our findings indicate that aspect ratio alone is not a significant geometric factor in influencing the temperature difference on the FO cable, as configurations with similar aspect ratios exhibit different temperature differences and the thermal properties of the material used in the FO cable, as well as its volume, influence the thermal heat loss from cable. To select the optimal microstructures to implement in observational experiments, additional criteria beyond the highest temperature difference must be considered. The ΔT should be sufficiently large to be detectable by FODS as the standard uncertainty for the conventional FO device, Silixa Ultima-S DTS system (Hertfordshire, UK), is defined as 0.36 °C for sampling every second, over every 12.7 cm and for FO cables less than 500 meters (des Tombe et al., 2020). In addition, the microstructures should cover as little of the FO cable as possible with PVC, minimizing any increase in the fiber's response time to temperature changes and reducing the extra weight associated with additional costs. Based on before mentioned criterion, the geometry combinations of $r = 18$ mm, $h = 24$, and $s = 20$ mm in filled-coned and $r = 24$ mm, $h = 24$, and $s = 15$ mm in hollow-coned is selected as the most promising combinations to further investigate the effect of turbulence intensity on resulted ΔT's.

3.2 Effects of turbulence intensity on ΔT and Δk

The dynamic nature of the atmospheric boundary layer generates varying flow conditions near the Earth's surface, resulting in a range of turbulence intensities. To evaluate the performance of the selected microstructure configurations under different turbulence conditions, we applied a conventional range of TI values (Table 1) to the inflow of the 2D model. The filled-coned configuration demonstrated the capability to maintain a $\Delta T > 1$ K for TI values below 0.2 and inlet velocities (U_{in}) up to 2 m s^{-1}, as illustrated in Fig. 7a. This temperature difference is significantly large to be detected using FODS. Furthermore, the magnitude of the ΔK on the FO cable exhibited a higher sensitivity to TI compared to the inlet wind speed. This observation underscores the critical role of TI in governing directional heat loss from the FO cable. On the other hand, the hollow-coned microstructure maintained a ΔT exceeding 2 K across all turbulence intensities and for inlet wind speeds of up to 4 m s^{-1} (Fig. 8a). The ΔK decreased with increasing inlet wind speed across the range of TI values, exhibiting only a minimal increase in TI between 0.1 and 0.15 (Fig. 8a). These findings indicate that the selected hollow-coned microstructure outperforms the filled-coned configuration across the range of tested turbulence intensities.

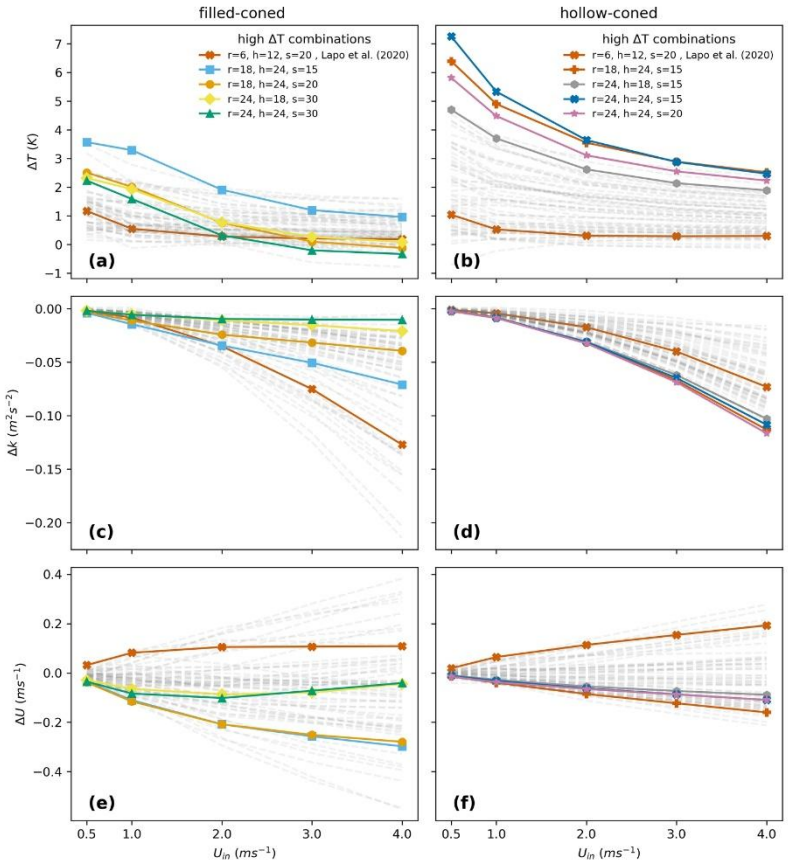

Figure 6. The differences in modeled temperature (ΔT) **(a, b)**, turbulent kinetic energy (ΔK) **(c, d)**, and total wind speed (ΔU) **(e, f)** between forward and backward fiber optic cables are presented for varying inlet wind speeds in filled-coned and hollow-coned microstructures, respectively, across 64 geometric combinations. The four combinations producing the highest ΔT, along with one corresponding to the geometry of the filled-coned microstructure modeled in Lapo et al. (2020), are shown as solid lines with markers, while the remaining combinations are depicted as faded lines.

3.3 Wind attack angle effect on ΔT and Δk

The wind attack angle is critically important for real-world applications at the field scale, since the turbulent flow varies substantially in speed and direction. The inclusion of hollow-coned microstructures in this study aimed at decreasing the sensitivity of the FO cable's temperature difference (ΔT) to lateral winds, i.e. flow component orthogonal to the orientation of the FO cable, when compared to the previous study. Consequently, the wind attack angle effect was analyzed exclusively for FO cables featuring hollow-coned microstructures with a 3D model. In the analysis, inlet wind was applied at attack angles of 0, 30, 60, and 90° relative to the fiber. The 0° attack angle corresponds to wind aligned along the fiber, whereas the 90° angle represents wind orthogonal to the fiber. As expected, the hollow-coned configuration with geometry parameters of $r = 24$ mm, $h = 24$, and $s = 15$ exhibited a ΔT of up to 0.8 K at a wind attack angle of 60° (Fig. 9a). Furthermore, this configuration demonstrated a distinct decay pattern in ΔT across various wind speeds and attack angles, a crucial characteristic for analyzing real FO cables. The turbulent kinetic energy difference (ΔK) increased with inlet wind speed, reaching its maximum at a wind attack angle of 30°, where the maximum ΔK was observed to be $-0.32\,\mathrm{m^2\,s^{-2}}$ (Fig. 9b).

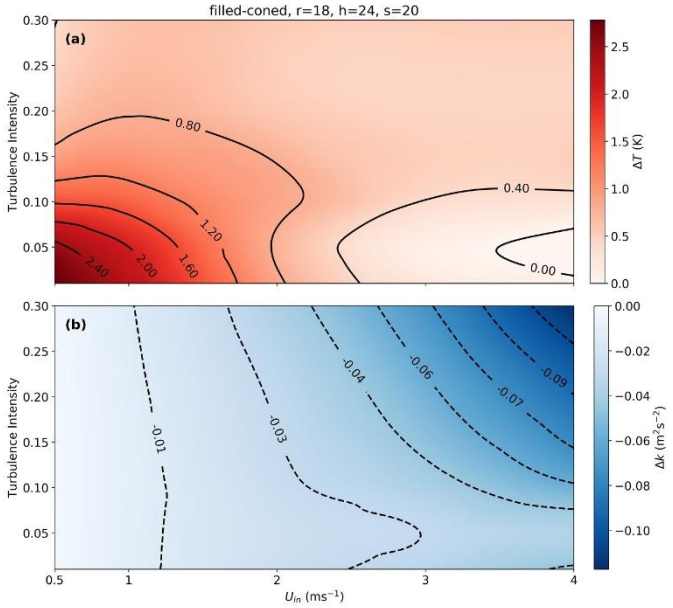

Figure 7. **(a)** The variation of **(a)** ΔT and **(b)** ΔK across different turbulence intensities and inlet wind speeds for the selected filled-coned microstructure based on 2D model. This map and also the map in Fig. 8 are generated using cubic interpolation of discrete values of the modeled ΔT and ΔK across different TI's and inlet wind speeds.

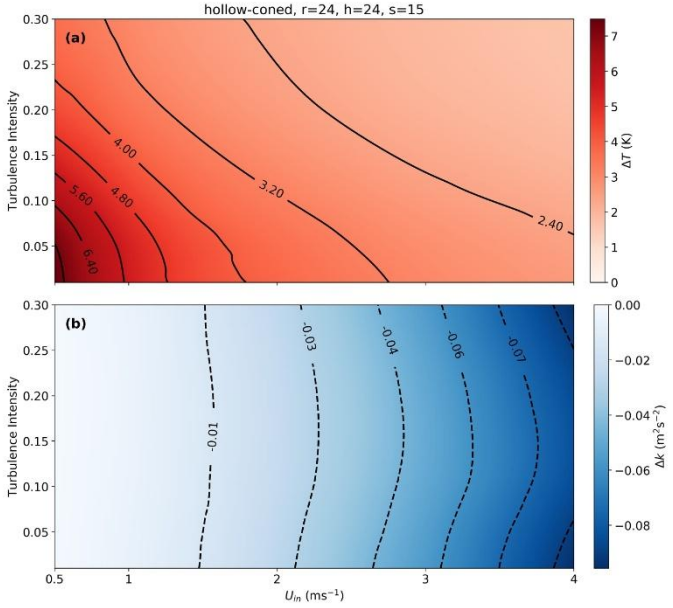

Figure 8. **(a)** The variation of **(a)** ΔT and **(b)** ΔK across different turbulence intensities and inlet wind speeds for the selected hollow-coned microstructure based on 3D model.

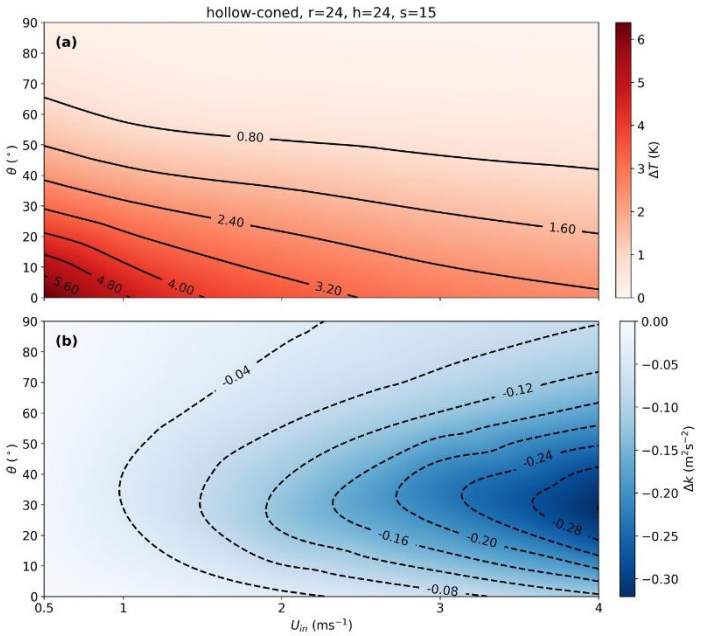

Figure 9. Directional sensitivity of ΔT for the selected geometric configuration of hollow-cone microstructures. This map is generated using cubic interpolation of discrete values of the modeled ΔT and ΔK across different wind attack angles and inlet wind speeds.

4 Conclusions

This study investigated the influence of varying geometry of microstructures attached to FO cables on the thermal and turbulence responses under varying flow conditions and turbulence intensities. A comparative evaluation of geometric configurations identified specific combinations of hollow-cone- and filled-coned microstructures which optimize ΔT while balancing additional criteria, such as maintaining sensitivity to wind speed and minimizing PVC coverage on the FO cable. The findings highlight the potential to improving upon earlier numerical and experimental studies employing the same principle by optimizing geometry of the microstructures including their radius, height, spacing, shape, and hollow or filled while at the same time reducing the sensitivity of the heated filled-coned FO cable to flow components orthogonal to the cable. The results demonstrated that FO cables with filled-coned microstructures with a radius of 18 mm, height of 24, and spacing of 20 mm outperformed the earlier designs. Moreover, FO cables with hollow-coned microstructures, with parameters $r = 24$ mm, $h = 24$ mm, and $s = 15$ mm, exhibited superior performance over the tested conditions. These hollow-coned configurations maintained ΔT values exceeding 2 K across all turbulence intensities and wind speeds up to 4 m s^{-1}, demonstrating robustness across a wide range of flow conditions. In contrast to the study by Lapo et al. (2020), which primarily considers the aspect ratio and spacing of the cones to determine the optimal configuration, our findings demonstrate that aspect ratio alone is not a decisive geometric factor in influencing the temperature difference on the FO cable. Instead, the cone's overall dimensions play a crucial role, as configurations with similar aspect ratios exhibit different temperature differences. This study also emphasizes the importance of integrating heat transfer and turbulent flow, considering not only turbulence but also the thermal properties and volume of the material, which are directly linked to cone dimensions. Sensitivity analysis of wind attack angles revealed that the hollow-coned combination achieved a ΔT of up to 0.8 K at a 60° angle, with a distinct decay pattern across various wind speeds. This analysis is important because in the real-world, 3D turbulent flows are inherently stochastic in both wind speed and direction. This behavior underscores the significance of microstructure design in mitigating the impact of orthogonal wind and preserving temperature gradients along the FO cable. These results pave the way for deploying optimized FO cable designs specifically for weak-wind boundary layer studies, enhancing their capability to accurately capture wind direction and observe distributed turbulent heat fluxes using FODS as demonstrated in Abdoli et al. (2023).

Future research should prioritize experimental validation of the proposed designs under field conditions to confirm their robustness and reliability in real-world applications. Such studies will further advance the applicability of FO cables in atmospheric boundary layer research, particularly in enhancing the accuracy of distributed heat flux and turbulence measurements.

Appendix A: Abbreviations

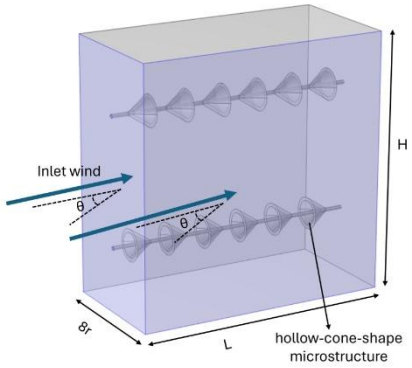

Figure A1. A 3-dimensional schematic of the hollow-coned model with inlet wind vectors varying with θ. The light blue surfaces were designated as inlets to expose the FO cables to constant wind speeds at different angles.

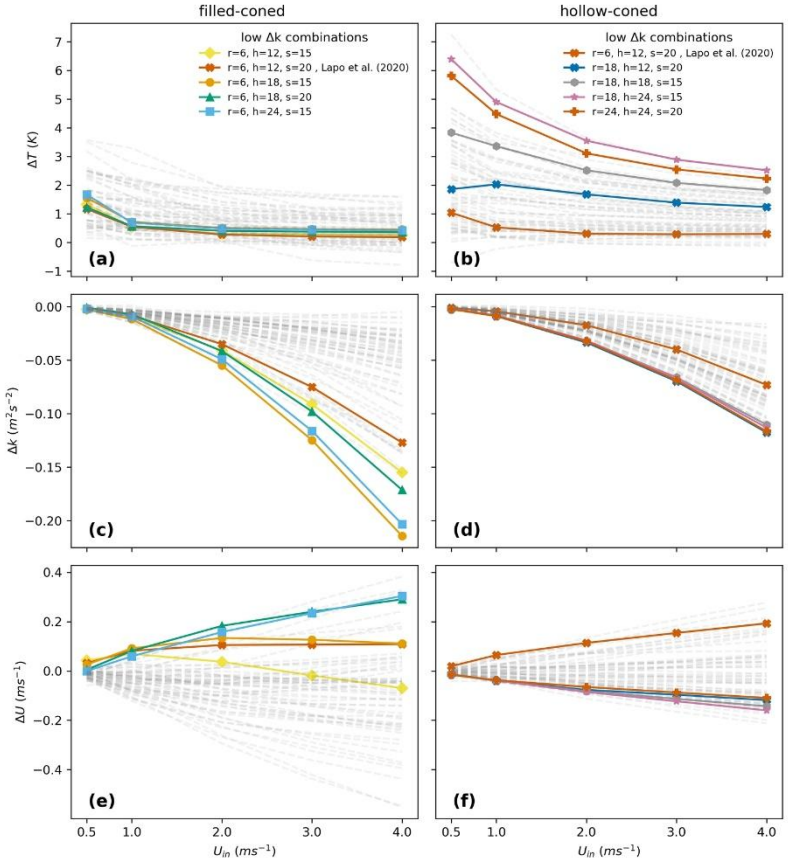

Figure A2. The differences in temperature (ΔT) **(a, b)**, turbulent kinetic energy (ΔK) **(c, d)**, and total wind speed (ΔU) **(e, f)** between forward and backward fiber optic cables are presented for varying inlet wind speeds in filled-coned and hollow-coned microstructures, respectively, across 64 geometric combinations. The four combinations producing the highest ΔK, along with one corresponding to the geometry of the filled-coned microstructure modeled in Lapo et al. (2020), are shown as solid lines with markers, while the remaining combinations are depicted as faded lines.

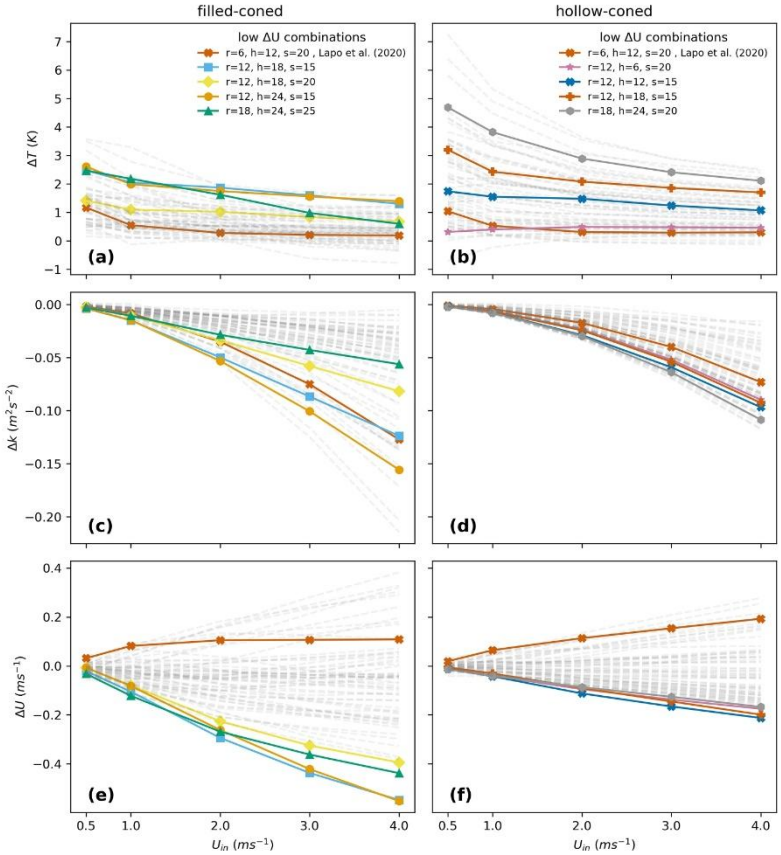

Figure A3. The differences in temperature (ΔT) **(a, b)**, turbulent kinetic energy (ΔK) **(c, d)**, and total wind speed (ΔU) **(e, f)** between forward and backward fiber optic cables are presented for varying inlet wind speeds in filled-coned and hollow-coned microstructures, respectively, across 64 geometric combinations. The four combinations producing the highest ΔU, along with one corresponding to the geometry of the filled-coned microstructure modeled in Lapo et al. (2020), are shown as solid lines with markers, while the remaining combinations are depicted as faded lines.

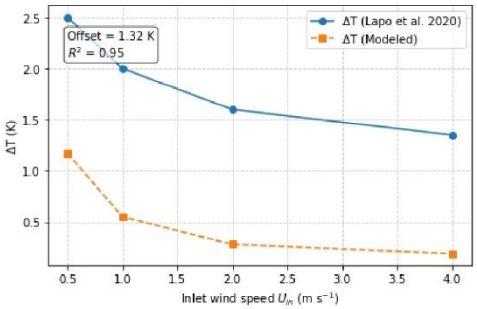

Figure A4. The comparison of the best performing filled-cone microstructure design ($r = 6$ mm, $h = 12$ mm, $s = 20$ mm) reported by Lapo et al. (2020) with the one modeled in this study.

Table A1. Nomenclature.

Parameter	Symbol	Description	Units
Temperature	T	Absolute temperature	K
Turbulent kinetic energy	K	Turbulent kinetic energy	$m^2\,s^{-2}$
Inlet velocity	U_{in}	Velocity of the airflow at the inlet	$m\,s^{-1}$
Radius	r	Radius of the filled-coned or hollow–coned microstructure	mm
Length	L	Length of the Channel	mm
Height	h	Height of the microstructure	mm
Spacing	s	Spacing between microstructures	mm
Wind attack angle	θ	Wind attack angle	degrees
Turbulence intensity	TI	Intensity of turbulence in the flow	Dimensionless
Turbulence integral length scale	TL	Integral length scale of turbulence	m
Interface temperature	T_0	Temperature at PVC and fiber interface	°C
Solid density	ρ_s	Density of the solid material	$kg\,m^{-3}$
Specific heat	C_p	Specific heat capacity at constant pressure	$J\,kg^{-1}\,K^{-1}$
Translational velocity	$\boldsymbol{u}_{trans}$	Velocity vector of translational motion	$m\,s^{-1}$
Heat flux (conduction)	$\mathbf{q}$	Heat flux by conduction	$W\,m^{-2}$
Heat flux (radiation)	$\mathbf{q}_r$	Heat flux by radiation	$W\,m^{-2}$
Thermal expansion	α, α_p	Coefficient of thermal expansion	K^{-1}
Stress tensor	S	Second Piola-Kirchhoff stress tensor	Pa
Heat source	Q_{add}	Additional heat sources	$W\,m^{-3}$
Fluid density	ρ	Density of the fluid	$kg\,m^{-3}$
Fluid pressure	p	Pressure in the fluid	Pa
Viscous stress tensor	τ	Stress tensor representing viscous forces	Pa
Eddy viscosity	μ_T	Turbulent eddy viscosity	Pa s
Turbulent dissipation	ϵ	Rate of turbulent kinetic energy dissipation	$m^2\,s^{-3}$
Production term	P_k	Production term for turbulent kinetic energy	$m^2\,s^{-3}$
Constant for turbulence	C_μ	Constant in k–ϵ model ($C_\mu = 0.09$)	Dimensionless
Turbulence constant 1	$C_{\epsilon 1}$	Constant in ϵ equation ($C_{\epsilon 1} = 1.44$)	Dimensionless
Turbulence constant 2	$C_{\epsilon 2}$	Constant in ϵ equation ($C_{\epsilon 2} = 1.92$)	Dimensionless
Turbulence constant 3	σ_k	Constant for turbulent kinetic energy equation ($\sigma_k = 1.0$)	Dimensionless
Turbulence constant 4	σ_ϵ	Constant for turbulent dissipation equation ($\sigma_\epsilon = 1.3$)	Dimensionless

Appendix B: Governing physics

Turbulence was modeled using the K-ϵ approach, and the "Heat Transfer in Solids and Fluids" module was employed to simulate the thermal interactions between the filled-coned fiber and the ambient air. The bidirectional coupling between turbulent flow and heat transfer was achieved by adopting the non-isothermal flow coupling interface. To obtain more accurate solution results, the Kays-Crawford heat transfer turbulence model was adopted in the simulation studies. The following sections present the governing equations of the employed model, including those pertaining to heat transfer in solids and fluids, as well as turbulent flow.

B1 Heat Transfer in Solids

The heat conduction in a solid is described by the Fourier equation, where heat transfers from the higher temperature point to the lower temperature point. The following equation describes the heat transfer in solids:

$$\rho_s C_p \left(\frac{\partial T}{\partial t} + \boldsymbol{u}_{trans} \cdot \nabla T \right) + \nabla \cdot (\mathbf{q} + \mathbf{q}_r) = -\alpha : \frac{dS}{dt} + Q_{add} \quad \text{(B1)}$$

Where ρ_s represents the density of the solid, C_p denotes the specific heat at constant pressure, and T stands for the absolute temperature. The velocity vector of translational motion is given by $\boldsymbol{u}_{trans}$, while $\mathbf{q}$ and $\mathbf{q}_r$ correspond to the heat flux by conduction and by radiation, respectively. The coefficient of thermal expansion is denoted by α, and S is the second Piola-Kirchhoff stress tensor. Finally, Q_{add} accounts for any additional heat sources present in the system. The colon (:)

represents the double dot product (or tensor contraction) between two second-order tensors.

B2 Heat Transfer in Fluids

The heat transfer in fluids can be described by the following equation:

$$\rho C_p \left(\frac{\partial T}{\partial t} + \boldsymbol{u} \cdot \nabla T \right) + \nabla \cdot (\mathbf{q} + \mathbf{q}_\mathrm{r}) = Q_p + Q_v + Q_\mathrm{add} \quad \text{(B2)}$$

where:

$$Q_p = \alpha_p T \left(\frac{\partial p}{\partial t} + \boldsymbol{u} \cdot \nabla p \right), \quad Q_v = \tau : \nabla \boldsymbol{u} \quad \text{(B3)}$$

Where p denotes the pressure, and α_p is the coefficient of thermal expansion. The velocity vector is given by $\boldsymbol{u}$, while $\mathbf{q}$ and $\mathbf{q}_\mathrm{r}$ represent the heat flux by conduction and radiation, respectively. The viscous stress tensor is denoted by τ. The coefficient of thermal expansion α_p is given by:

$$\alpha_p = -\frac{1}{\rho} \frac{\partial \rho}{\partial T} \quad \text{(B4)}$$

In accordance with the simulation's stationary mode, the time-dependent variables presented in Eqs. (1)–(4) are equal to zero.

B3 Turbulent Flow

The k–ϵ model contains two dependent variables: turbulent kinetic energy (K) and the turbulent dissipation rate (ϵ). The eddy viscosity (μ_T) is defined as:

$$\mu_\mathrm{T} = \rho C_\mu \frac{k^2}{\epsilon} \quad \text{(B5)}$$

and the transport equation for K is as follows:

$$\rho \frac{\partial k}{\partial t} + \rho \boldsymbol{u} \cdot \nabla k = \nabla \cdot \left[\left(\mu + \frac{\mu_\mathrm{T}}{\sigma_\mathrm{k}} \right) \nabla k \right] + P_\mathrm{k} - \rho \epsilon \quad \text{(B6)}$$

where the production term P_k is:

$$P_\mathrm{k} = \mu_\mathrm{T} \left[\nabla \boldsymbol{u} : \left(\nabla \boldsymbol{u} + (\nabla \boldsymbol{u})^T \right) - \frac{2}{3} (\nabla \cdot \boldsymbol{u})^2 \right] - \frac{2}{3} \rho k \nabla \cdot \boldsymbol{u} \quad \text{(B7)}$$

The transport equation for ϵ is as follows:

$$\rho \frac{\partial \epsilon}{\partial t} + \rho \boldsymbol{u} \cdot \nabla \epsilon = \nabla \cdot \left[\left(\mu + \frac{\mu_\mathrm{T}}{\sigma_\epsilon} \right) \nabla \epsilon \right] + C_{\epsilon 1} \frac{\epsilon}{k} P_\mathrm{k} - C_{\epsilon 2} \rho \frac{\epsilon^2}{k} \quad \text{(B8)}$$

Where the constant values are determined as follows: $C_\mu = 0.09$, $C_{\epsilon 1} = 1.44$, $C_{\epsilon 2} = 1.92$, $\sigma_\mathrm{k} = 1.0$, and $\sigma_\epsilon = 1.3$.

Data availability. The datasets generated and analyzed during the current study are publicly available in the Zenodo repository under the following link: https://doi.org/10.5281/zenodo.17136833 (Abdoli, 2025).

Author contributions. Conceptualization: MA; methodology and manufacturing: MA and RP; formal analysis: MA; investigation: MA; data curation: MA; writing – original draft preparation: MA; writing – review and editing: MA and CKT; visualization: MA; project administration: CKT and MA; funding acquisition: CKT. All authors have read and agreed to the published version of the paper.

Competing interests. The contact author has declared that none of the authors has any competing interests.

Disclaimer. Publisher's note: Copernicus Publications remains neutral with regard to jurisdictional claims made in the text, published maps, institutional affiliations, or any other geographical representation in this paper. While Copernicus Publications makes every effort to include appropriate place names, the final responsibility lies with the authors. Views expressed in the text are those of the authors and do not necessarily reflect the views of the publisher.

Acknowledgements. This publication was funded by the open-access publishing fund of the University of Bayreuth. We also thank the two anonymous reviewers for their constructive comments and suggestions, which helped improve the quality of this manuscript.

Financial support. This research has been supported by the European Research Council, H2020 European Research Council (grant no. 724629).

Review statement. This paper was edited by Cléo Quaresma Dias-Junior and reviewed by two anonymous referees.

References

Abdoli, M.: Improving turbulent airflow direction measurements for fiber-optic distributed sensing using numerical simulations, Zenodo [data set], https://doi.org/10.5281/zenodo.17136833, 2025.

Abdoli, M., Lapo, K., Schneider, J., Olesch, J., and Thomas, C. K.: Toward quantifying turbulent vertical airflow and sensible heat flux in tall forest canopies using fiber-optic distributed temperature sensing, Atmos. Meas. Tech., 16, 809–824, https://doi.org/10.5194/amt-16-809-2023, 2023.

Bado, M. F.: Distributed Sensing for Serviceability Analysis of Reinforced Concrete Structures, Ph.D. Thesis, Vilnius Tech, Vilnius, Lithuania, https://etalpykla.vilniustech.lt/handle/123456789/107056 (last access: 10 November 2025), 2021.

Bense, V. F., Read, T., and Verhoef, A.: Using distributed temperature sensing to monitor field scale dynamics of ground surface temperature and related substrate heat flux, Agricultural and Forest Meteorology, 220, 207–215, https://doi.org/10.1016/j.agrformet.2016.01.138, 2016.

Chen, X., Zhou, X., Zhong, Z., Liang, N., Wang, Y., and Zhang, X.: Study on temperature field and influencing factors of the high geothermal tunnel with extra-long one-end construction ventilation, International Journal of Thermal Sciences, 191, 108322, https://doi.org/10.1016/j.ijthermalsci.2023.108322, 2023.

de Jong, S. A. P., Slingerland, J. D., and van de Giesen, N. C.: Fiber optic distributed temperature sensing for the determination of air temperature, Atmos. Meas. Tech., 8, 335–339, https://doi.org/10.5194/amt-8-335-2015, 2015.

des Tombe, B., Schilperoort, B., and Bakker, M.: Estimation of Temperature and Associated Uncertainty from Fiber-Optic Raman-Spectrum Distributed Temperature Sensing, Sensors, 20, 2235, https://doi.org/10.3390/s20082235, 2020.

Freundorfer, A., Lapo, K., Schneider, J., and Thomas, C. K.: Distributed Sensing of Wind Direction Using Fiber-Optic Cables, Journal of Atmospheric and Oceanic Technology, https://doi.org/10.1175/JTECH-D-21-0019.1, 2021.

Fritz, A. M., Lapo, K., Freundorfer, A., Linhardt, T., and Thomas, C. K.: Revealing the Morning Transition in the Mountain Boundary Layer Using Fiber-Optic Distributed Temperature Sensing, Geophysical Research Letters, 48, e2020GL092238, https://doi.org/10.1029/2020GL092238, 2021.

Higgins, C. W., Wing, M. G., Kelley, J., Sayde, C., Burnett, J., and Holmes, H. A.: A high resolution measurement of the morning ABL transition using distributed temperature sensing and an unmanned aircraft system, Environmental Fluid Mechanics, 18, 683–693, https://doi.org/10.1007/s10652-017-9569-1, 2018.

Huss, J.-M. and Thomas, C. K.: The Impact of Turbulent Transport Efficiency on Surface Vertical Heat Fluxes in the Arctic Stable Boundary Layer Predicted from Similarity Theory and Machine Learning, Journal of the Atmospheric Sciences, 81, 1977–1998, 2024.

Ishii, H., Kawamura, K., Ono, T., Megumi, H., and Kikkawa, A.: A fire detection system using optical fibres for utility tunnels, Fire Safety Journal, 29, 87–98, https://doi.org/10.1016/S0379-7112(96)00065-3, 1997.

Johny, J., Amos, S., and Prabhu, R.: Optical fibre-based sensors for oil and gas applications, Sensors, 21, 6047, https://doi.org/10.3390/s21186047, 2021.

Kalantari, H., Ghoreishi-Madiseh, S. A., Kurnia, J. C., and Sasmito, A. P.: An analytical correlation for conjugate heat transfer in fin and tube heat exchangers, International Journal of Thermal Sciences, 164, 106915, https://doi.org/10.1016/j.ijthermalsci.2021.106915, 2021.

Keller, C. A., Huwald, H., Vollmer, M. K., Wenger, A., Hill, M., Parlange, M. B., and Reimann, S.: Fiber optic distributed temperature sensing for the determination of the nocturnal atmospheric boundary layer height, Atmos. Meas. Tech., 4, 143–149, https://doi.org/10.5194/amt-4-143-2011, 2011.

Lapo, K., Freundorfer, A., Pfister, L., Schneider, J., Selker, J., and Thomas, C.: Distributed observations of wind direction using microstructures attached to actively heated fiber-optic cables, Atmos. Meas. Tech., 13, 1563–1573, https://doi.org/10.5194/amt-13-1563-2020, 2020.

Lapo, K., Freundorfer, A., Fritz, A., Schneider, J., Olesch, J., Babel, W., and Thomas, C. K.: The Large eddy Observatory, Voitsumra Experiment 2019 (LOVE19) with high-resolution, spatially distributed observations of air temperature, wind speed, and wind direction from fiber-optic distributed sensing, towers, and ground-based remote sensing, Earth Syst. Sci. Data, 14, 885–906, https://doi.org/10.5194/essd-14-885-2022, 2022.

Launder, B. and Sharma, B.: Application of Energy Dissipation Model of Turbulence to the Calculation of Flow Near Spinning Disc, Letters Heat Mass Transfer, 1, 131–137, https://doi.org/10.1016/0735-1933(74)90024-4, 1974.

Ma, Y., Mohebbi, R., Yang, Z., and Sheremet, M. A.: Numerical analysis of heat sink configurations and their impact on conjugate heat transfer in manifold systems, International Journal of Thermal Sciences, 218, 110145, https://doi.org/10.1016/j.ijthermalsci.2025.110145, 2025.

Mack, L., Kähnert, M., Rauschenbach, Q., Frank, L., Hasenburg, F. H., Huss, J.-M., Jonassen, M. O., Malpas, M., Batrak, Y., Remes, T., Pirk, N., and Thomas, C. K.: Stable Boundary Layers in an Arctic Fjord-Valley System: Evaluation of Temperature Profiles Observed From Fiber-Optic Distributed Sensing and Comparison to Numerical Weather Prediction Systems at Different Resolutions, Journal of Geophysical Research: Atmospheres, 130, e2024JD042825, https://doi.org/10.1029/2024JD042825, 2025.

Nakstad, H. and Kringlebotn, J. T.: Probing oil fields, Nature Photonics, 2, 147–149, 2008.

Owen, P. R. and Thomson, W.: Heat transfer across rough surfaces, Journal of Fluid Mechanics, 15, 321–334, 1963.

Peltola, O., Lapo, K., Martinkauppi, I., O'Connor, E., Thomas, C. K., and Vesala, T.: Suitability of fibre-optic distributed temperature sensing for revealing mixing processes and higher-order moments at the forest–air interface, Atmos. Meas. Tech., 14, 2409–2427, https://doi.org/10.5194/amt-14-2409-2021, 2021.

Pfister, L., Lapo, K., Mahrt, L., and Thomas, C. K.: Thermal Submeso Motions in the Nocturnal Stable Boundary Layer. Part 2: Generating Mechanisms and Implications, Boundary-Layer Meteorology, 180, 203–224, https://doi.org/10.1007/s10546-021-00619-z, 2021a.

Pfister, L., Lapo, K., Mahrt, L., and Thomas, C. K.: Thermal Submeso Motions in the Nocturnal Stable Boundary Layer. Part 2: Generating Mechanisms and Implications, Boundary-Layer Meteorology, 180, 203–224, https://doi.org/10.1007/s10546-021-00619-z, 2021b.

Puntigam, S., Radl, S., and Karlinger, P.: Considerations for Computational Fluid Dynamics Studies of Cleanrooms Exceeding Classical Indoor Air Simulations: A Systematic Review, Indoor Air, 2025, 4302921, https://doi.org/10.1155/ina/4302921, 2025.

Sayde, C., Thomas, C. K., Wagner, J., and Selker, J.: High-resolution wind speed measurements using actively heated fiber optics, Geophysical Research Letters, 42, 10064–10073, https://doi.org/10.1002/2015GL066729, 2015.

Schilperoort, B., Coenders-Gerrits, M., Jiménez Rodríguez, C., van der Tol, C., van de Wiel, B., and Savenije, H.: Decoupling of a Douglas fir canopy: a look into the subcanopy with continuous vertical temperature profiles, Biogeosciences, 17, 6423–6439, https://doi.org/10.5194/bg-17-6423-2020, 2020.

Selker, J. S., Thévenaz, L., Huwald, H., Mallet, A., Luxemburg, W., Van De Giesen, N., Stejskal, M., Zeman, J., West-

hoff, M., and Parlange, M. B.: Distributed fiber-optic temperature sensing for hydrologic systems, Water Resources Research, 42, 2006WR005326, https://doi.org/10.1029/2006WR005326, 2006.

Silva, L. C. B., Segatto, M. E. V., and Castellani, C. E. S.: Raman scattering-based distributed temperature sensors: A comprehensive literature review over the past 37 years and towards new avenues, Optical Fiber Technology, 74, 103091, https://doi.org/10.1016/j.yofte.2022.103091, 2022.

Sogukpinar, H.: Effect of hairy surface on heat production and thermal insulation on the building, Environmental Progress & Sustainable Energy, 39, e13435, https://doi.org/10.1002/ep.13435, 2020.

Steele-Dunne, S. C., Rutten, M. M., Krzeminska, D. M., Hausner, M., Tyler, S. W., Selker, J., Bogaard, T. A., and Van De Giesen, N. C.: Feasibility of soil moisture estimation using passive distributed temperature sensing, Water Resources Research, 46, 2009WR008272, https://doi.org/10.1029/2009WR008272, 2010.

Sun, J., Mahrt, L., Banta, R. M., and Pichugina, Y. L.: Turbulence Regimes and Turbulence Intermittency in the Stable Boundary Layer during CASES-99, Journal of the Atmospheric Sciences, https://doi.org/10.1175/JAS-D-11-082.1, 2012.

Sun, Y., Yao, S., and Alexandersen, J.: Topography optimisation using a reduced-dimensional model for transient conjugate heat transfer between fluid channels and solid plates with volumetric heat source, Structural and Multidisciplinary Optimization, 67, 45, https://doi.org/10.1007/s00158-024-03760-8, 2024.

Taniguchi, M.: Evaluation of vertical groundwater fluxes and thermal properties of aquifers based on transient temperature-depth profiles, Water Resources Research, 29, 2021–2026, 1993.

Thomas, C. K. and Selker, J.: Optical Fiber-Based Distributed Sensing Methods, in: Springer Handbook of Atmospheric Measurements, edited by: Foken, T., Springer International Publishing, Cham, 609–631, ISBN 978-3-030-52171-4, https://doi.org/10.1007/978-3-030-52171-4_20, 2021.

Thomas, C. K., Kennedy, A. M., Selker, J. S., Moretti, A., Schroth, M. H., Smoot, A. R., Tufillaro, N. B., and Zeeman, M. J.: High-Resolution Fibre-Optic Temperature Sensing: A New Tool to Study the Two-Dimensional Structure of Atmospheric Surface-Layer Flow, Boundary-Layer Meteorology, 142, 177–192, https://doi.org/10.1007/s10546-011-9672-7, 2012.

Tyler, S. W., Selker, J. S., Hausner, M. B., Hatch, C. E., Torgersen, T., Thodal, C. E., and Schladow, S. G.: Environmental temperature sensing using Raman spectra DTS fiber-optic methods, Water Resources Research, 45, https://doi.org/10.1029/2008WR007052, 2009.

Ukil, A., Braendle, H., and Krippner, P.: Distributed Temperature Sensing: Review of Technology and Applications, IEEE Sensors Journal, 12, 885–892, https://doi.org/10.1109/JSEN.2011.2162060, 2012.

van Ramshorst, J. G. V., Coenders-Gerrits, M., Schilperoort, B., van de Wiel, B. J. H., Izett, J. G., Selker, J. S., Higgins, C. W., Savenije, H. H. G., and van de Giesen, N. C.: Revisiting wind speed measurements using actively heated fiber optics: a wind tunnel study, Atmos. Meas. Tech., 13, 5423–5439, https://doi.org/10.5194/amt-13-5423-2020, 2020.

Watkins, S.: Turbulence characteristics of the atmospheric boundary layer and possibilities of replication for aircraft, in: Joint Symposium of DFG and DLR-Airbus Third-Symposium-Simulation of Wing and Nacelle Stall, 21–22, 2012.

Zeeman, M. J., Selker, J. S., and Thomas, C. K.: Near-Surface Motion in the Nocturnal, Stable Boundary Layer Observed with Fibre-Optic Distributed Temperature Sensing, Boundary-Layer Meteorology, 154, 189–205, https://doi.org/10.1007/s10546-014-9972-9, 2015.

Paper III

Dynamic stability and canopy structure drive Spatio-Temporal Variability of Greenhouse Gases in the sub-canopy of a Temperate Spruce Forest

Status: Submitted (2025, under review)
Journal: Agricultural and Forest Meteorology
doi: http://dx.doi.org/10.2139/ssrn.5681842

Dynamic stability and canopy structure drive Spatio-Temporal Variability of Greenhouse Gases in the sub-canopy of a Temperate Spruce Forest

Mohammad Abdoli[1,4] · Karl Lapo[2] · Christoph K. Thomas[1,3]

Abstract

We investigated the micrometeorological controls on spatio-temporal variability of CO_2, CH_4, and H_2O mixing ratios in the horizontal and vertical dimensions within a temperate forest canopy using high-resolution measurements from sensor networks and machine learning techniques. The main objective was to identify the governing factors controlling scalar gas variability within the sub-canopy and to assess how static stability and thermal stratification influence scalar mixing processes under varying wind regimes. Scalar variability was characterized in both vertical and horizontal dimensions across weak- and strong-wind regimes, defined using sub- and above-canopy turbulence statistics. A Random Forest model was employed to identify key drivers of scalar variability showing that in the forest sub-canopy it is primarily controlled by shear-induced turbulence during strong winds and by buoyancy during weak winds. Under strong wind conditions, CO_2 variability is mainly influenced by TKE and dynamic stability, whereas air temperature becomes the key driver under weak-wind conditions. For CH_4, temperature remains an important factor across all conditions, with wind shear playing a role during strong winds and horizontal advection influencing its variability under weak winds. H_2O variability is closely tied to temperature in all wind regimes, reflecting evapotranspiration dynamics and energy distribution. Additionally, vertical profiles of potential temperature from Fiber-Optic Distributed Sensing (FODS) were clustered using k-means to classify stratification regimes, showing that unstable temperature profiles promote mixing and reduce variability,

✉ Mohammad Abdoli
Mohammad.abdoli@geo.rwth-aachen.de
[1] Micrometeorology Group, University of Bayreuth, Bayreuth, Germany
[2] Until Fall 2021: Micrometeorology Group, University of Bayreuth, Bayreuth, Germany
[3] Bayreuth Center for Ecology and Environmental Research (Bayceer), University of Bayreuth, Bayreuth, Germany
[4] Physical Geography and Climatology, Institute of Geography, RWTH Aachen University, Aachen, Germany

whereas stable stratification suppresses mixing and enhances scalar variability. Horizontal and vertical CO_2 and CH_4 spatial variability could be explained by thermal stratification, integrating effects of turbulence and radiation, while H_2O variability was primarily governed by evapotranspiration dynamics and energy availability, particularly during transition periods. Our results emphasize the critical role of the non-linear interplay of turbulence, static stability, canopy structure, and energy inputs in shaping fine-scale greenhouse gas mixing and transport. They also demonstrate the effectiveness of dense sensor networks combined with machine learning methods to enhance process-level understanding of gas exchange dynamics within the forest sub-canopy.

Keywords Greenhouse gases, Random Forest, wind regimes, thermal stratification, canopy flows, eddy covariance

1 Introduction

Forests play a substantial role in land-atmosphere interaction as they uptake carbon dioxide through photosynthesis. Covering approximately 30% of the Earth's surface, forests account for roughly 45% of terrestrial carbon storage and contribute to 50% of net primary production (Bonan, 2008). The intricate nature of forest's spatial variability makes it challenging to understand transport and mixing processes within their canopies and sub-canopy regions. Various factors including diverse canopy structures, clearings, and geometric configurations can significantly impact turbulence patterns and scalar variability and subsequently affect the exchange and budgets of mass, momentum, and heat within the canopy (Dupont et al., 2012; Thomas, 2011). While numerous studies have examined the carbon dioxide (CO_2) budget and transport within sub-canopy environments, there remains a noticeable scarcity of research investigating the spatiotemporal variations in the most important greenhouse scalar fields of carbon dioxide (CO_2), methane (CH_4), and water vapor (H_2O) in sub-canopy of temperate forests for different wind regimes which are foundational for comprehensively analysing transport processes, and mixing dynamics in the forest. Wind regimes are commonly classified as strong or weak wind conditions. Strong wind conditions occur when the wind speed exceeds a certain threshold, above which turbulence rapidly increases with increasing wind. In contrast, weak wind conditions correspond to wind speeds below this threshold, where turbulence is not driven by bulk

shear but rather generated locally through small-scale, non-stationary motions. (Liang et al., 2014; Mahrt et al., 2015; Sun et al., 2012). Learning more about the variability of scalars gains special attention due to the emergence of weak-wind situations in sub-canopy during the night time when the air near the ground stably stratifies and causes conventional theories of turbulence, including the Monin-Obukhov similarity theory, the Kolmogorov spectrum, and Taylor's hypothesis of frozen turbulence to collapse (Belcher et al., 2008). Various research efforts have explored the variability of sub-canopy scalar gas mixing ratios, as well as temperature and wind, using observational measurement networks in the forest. Wilson and Meyers, (2001) assessed the variability of sub-canopy using three Eddy Covariance (EC) systems that were separated vertically and horizontally. Their primary focus was to examine the representativeness of a single eddy covariance system in estimating soil respiration by examining the variation in turbulent fluxes of carbon dioxide, latent heat, and sensible heat. They concluded that the variability is time-dependent: as the temporal averaging period increases, the spatial variability of these fluxes decreases. Feigenwinter et al. (2010) investigated anomalous CO_2 patterns in Norunda, Sweden, during the late summer. Elevated CO_2 mixing ratios, peaking at 500 μmol mol^{-1} below 30 m above ground level (agl), exhibited substantial vertical and horizontal gradients, resulting in variable advective fluxes. This build-up of CO_2 occurred as canopy stratification shifted from stable to neutral conditions during the second part of the night, moving largest temperature and CO_2 gradients from near the ground to the forest crown space. Thomas (2011) investigated the space-time structure of wind and temperature fields within a dense forest sub-canopy in moderately complex terrains. Using a network of ten sensor stations and advanced analytical techniques, he revealed significant differences in the space-time characteristics of wind and temperature fields, with short-lived, small-scale motions dominating wind variability and diurnal temperature oscillations driving temperature signal variability over larger time scales. Nevertheless, this study did not incorporate scalar gas mixing ratios to assess their interrelated variability within the sub-canopy system.

Additionally, Oliveira et al. (2018) examined night-time wind and scalar variability within and above an Amazonian canopy by assessing nocturnal turbulent kinetic energy (TKE) and the exchange of energy, CO_2, and ozone (O_3) between the Amazon forest and the

atmosphere. Spectral analysis revealed that a substantial portion of the variability observed during intermittent nights can be attributed to low-frequency, non-turbulent fluctuations. Additionally, intermittent turbulence can lead to substantial fluxes impacting CO_2 and O_3 mixing ratios, highlighting the complex interplay of stability and turbulence in nocturnal atmospheric conditions. This study focuses exclusively on mixing ratio profiles and flow statistics in the vertical and horizontal directions. Given the inherent horizontal variability of canopy structure, soil properties, and ground surface conditions, these aspects are essential for a comprehensive characterization of transport and mixing processes within the canopy. Despite various studies investigating the variability of greenhouse gases, wind, and temperature in the sub-canopy, there is a lack of comprehensive research on the spatiotemporal variability of CO_2, H_2O, and CH_4 mixing ratios. Moreover, there is a need to identify the driving forces of each gas while highlighting the differences across different wind regimes.

Besides experimental observations, the Large-Eddy Simulation (LES) and various models have been extensively utilized to investigate flow and mixing ratio variability in forest environments (Kanani-Sühring and Raasch, 2015). However, simulations using advanced models are computationally intensive and often display significant biases compared to observational data (Girach et al., 2022). In contrast, machine learning (ML) models, which leverage observational datasets, are expected to generate outputs with lower biases due to their data-driven nature and have considerably shorter runtimes than conventional models. This has led to a growing recognition of the potential benefits of artificial intelligence (AI) and ML in atmospheric sciences (Arcomano et al., 2020). We employed ML approach to determine scalar gas driving forces in forest canopies for the purpose of: (i) identifying the most critical variables for modelling scalar gas variability and (ii) clustering vertical temperature profiles to evaluate scalar gas variability under different vertical temperature stratifications.

Our methodology relies on an extensive and unique observational dataset from Fiber-Optic Distributed Sensing (FODS) for continuous temperature observation in combination with a scalar gas sampling network for measuring CO_2, CH_4, and H_2O mixing ratios in both vertical and horizontal orientations, and the deployment of four EC systems. These advanced tools and data sources enable us to achieve our key research objectives. (i) To

elucidate the governing factors underlying the scalar gas variability observed within the sub-canopy, encompassing the dynamic fields of CO_2, H_2O, and CH_4. (ii) To understand the influence of static stability and thermal stratification on scalar mixing processes in the sub-canopy environment under different wind flow regimes. The integration of these innovative observational methods and analytical techniques empowers us to address these fundamental research inquiries comprehensively and advance our understanding of complex environmental dynamics within forested ecosystems.

2 Materials and methods

2.1 Study site

The Large-eddy ObsErvatory Waldstein Experiment 2020 (LOEWE20) was conducted at the long-term ecosystem flux site Waldstein-Weidenbrunnen (DE-Bay) between August and November 2020. The Waldstein is a forested site in the Fichtelgebirge mountains in the Lehstenbach catchment. The forest is dominated by Norway spruce (Picea abies) and is characterized by variable tree heights and densities. The canopy height was measured to be 27m in 2011 (Serafimovich et al., 2011). The sub-canopy vegetation is moderately dense with a cumulative plant area index of 0.7 m^2m^{-2}, characterized by shrubs ≤1 m in height. The plant area index (PAI) is 5.6±2.1 m^2m^{-2} for the overstory trees and 3.5 m^2m^{-2} for the understory trees. At the Waldstein site, the above-canopy flow is dominated by westerly and southeasterly winds with a wind speed range of 2 to 5 ms^{-1}; the understory flow is dominated by northerly and southwesterly winds with a range of 1 to 2 ms^{-1} (Foken, 2017). The experimental configuration of LOEWE20 (Fig. 1) consisted EC systems together with fast-response high-resolution pressure transducers, Gas Sampling Network (GCSN), and

FODS in a plot of approximately 200m×200m extended in both vertical and horizontal directions.

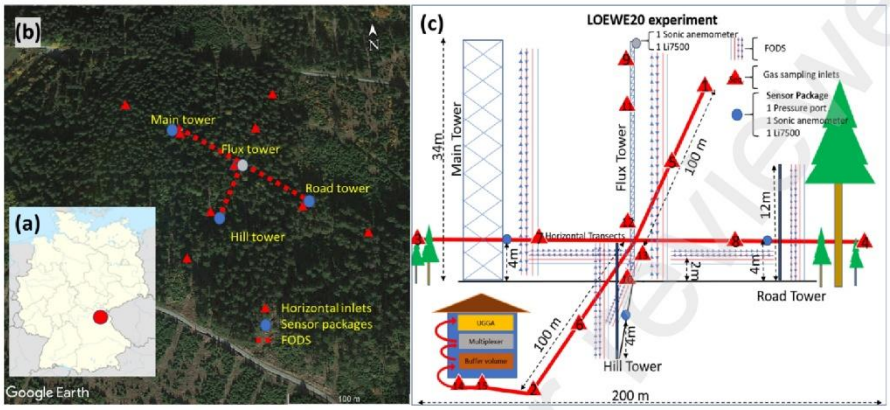

Figure 1. (a) Location of the LOEWE20 experiment marked with a red dot on the map of Germany. (b) Layout of the measurement network showing the FODS arrays as dashed red lines, the horizontal inlets of the Gas Mixing ratio Sampling Network (GCSN) as red triangles labelled S1–S8 and S12, and four vertical measurement towers with sensor packages indicated by blue solid points. (c) Detailed schematic of the experimental setup illustrating the vertical and horizontal FODS arrays, including two unconed fibers (one of which is heated) and two heated coned fibers, and the GCSN inlets in both vertical and horizontal configurations, along with the sensor packages placed at three positions at 4 m and one at 36 m height. UGGA refers to ultra-portable close-path greenhouse gas analyser.

2.2 Turbulent flux measurement

The LOEWE20 experiment includes four sensor packages. These sensors are positioned as follows: one at the top of the canopy at 36 m, and the remaining three at a height of 4 meters agl. All of the sensor packages are equipped with a sonic anemometer (Model CSAT3, Campbell Scientific Inc., Logan, UT, USA), and an open-path infrared CO_2 / H_2O gas analyser (Licor 7500, LI-COR Biosciences, USA). Except for the flux tower, which is a long-term EC system at the study site, the other three stations are additionally equipped with a quad disk static pressure transducer (Model 745-16B, Paroscientific, Inc.). The data of sensor packages at 4m were sampled at 20 Hz, and at the top of the 36m flux tower at 10 Hz. All of the eddy covariance systems in this study use the same eddy covariance data processing and flux computation routine described in Appendix A of (Thomas et al., 2009). Perturbation and averaging timescales of 10 min were used to compute the turbulent fluxes. Appendix A (Fig. A1) shows the time period of the data used in this study and the availability of different variables. It includes 3196 ten-minute intervals of EC and Gas

Mixing ratio Sampling Network (GCSN) data, along with 1248 intervals of available FODS observations from 10 September to 5 October 2020.

2.3 Gas Concentration Sampling Network (GCSN)

In addition to measuring CO_2 and H_2O turbulent fluxes and concentrations using four EC systems, an ultra-portable close-path greenhouse gas analyser (UGGA, Los Gatos Research Inc.) was used to measure the scalar gas mixing ratio including CH_4, CO_2, and H_2O sampled from different vertical and horizontal inlets. An air pump was used to draw air from each measurement inlet into the bottom of a 2.5-liter bottle-shaped buffer volume. The inlet of each tube at the measurement point was connected to a 1µm Gelman filter (ACRO 50 PTFE; Gelman, Ann Arbor, Michigan, USA). Additionally, a nylon funnel was installed at each air intake to minimize particle and rain water droplets entering the tubing and filter. Two further tubes are attached to the top of the buffer volume, one going to the UGGA multiplexer and the other connected to an air pump set to a flow rate for continuous ventilation of the buffer volume. The gas sampling multiplexer connected between the buffer volumes and the gas analyser allows sequencing between all inlets shown with red triangles (Fig. 1) of which 13 out of 15 inlets were positioned as vertical and horizontal ambient air inlets in the subcanopy and canopy spaces, and the remaining two were connected to 381 and 455 ppm reference CO_2 gases for continuous reference and validation. The sequence time for the 13 sampling ambient air was 7 minutes. The two reference gas inlets were measured for 90 s each after 11 full sequences of 13 ambient air inlets giving a total cycle time through all 15 inlets of 80 minutes.

In the post-processing stage, the initial 15 s of each measured sequence were discarded to allow for flushing the tubing and analyser's cavity to prevent cross-contamination between subsequent air samples. The remaining data were averaged to 10 minutes to synchronize with the turbulent flux measurements. The spatial standard deviation of scalar gas mixing ratios computed using the equation: $\hat{\sigma}_\chi = 1/n \sum_0^n (\chi_n - \hat{\chi})$, where $\hat{\sigma}_\chi$ stands for spatial standard deviation of scalar gas mixing ratio, n is the number of inlets used and χ is the mixing ratio in each inlet. Due to the existing systematic gradient in the vertical scalar gas mixing ratio profile, the hourly average profile is subtracted from the vertical inlets before computing the spatial standard deviation. The inlets S9, S10, S11, S12, and S13 used for vertical and S1, S2, S3, S4, S5, S6, S7, S8, and S12 used for horizontal standard deviation

computation. The accuracy of the UGGA device was determined to be -1.39 ppm for the 381 ppm and -0.04 ppm for the 455 ppm CO_2 reference gases. A cross-comparison of CO_2 and H_2O mixing ratios measured by the GCSN and EC systems at four EC stations is presented in the scatter plots in Fig. A2.

2.4 Fiber-Optic distributed sensing

A quartet of fiber-optic (FO) arrays is utilized for measuring distributed temperature, wind speed, and wind direction in both vertical and horizontal transects, as illustrated in Fig1. The FO arrays consist of two pairs of parallel coned and unconed FO cables, with one of the unconed and both coned fibers being heated using the Heat Pulse Unit (HPU) system (Model Heat Pulse System, Silixa, London, UK) and subjected to a constant electric current of 4 Wm-1 to the stainless-steel sheath. One of the cores of the FO cable contains four 50 µm multimode bend-insensitive cores (inner tube diameter = 1.06 mm, outer diameter = 1.32 mm; Model C-Tube, Solifos AG, Switzerland; resistance = 1.8Ω m-1) connected to the Distributed Temperature Sensing (DTS) device (Model 5 km ULTIMA, Silixa, London, UK) with a sampling resolution of 0.127 m and temporal resolution of 1 s. The cones of the coned FO cables are constructed from polyethylene with a diameter and height of 12 mm, spaced at 2 cm intervals along the FO cable (Freundorfer et al., 2021). Two warm and cold solid-phase calibration baths with a constant temperature (Thomas et al., 2022) were positioned at the beginning and end of the FO arrays to serve as calibration references. DTS measurements were conducted in a double-ended configuration using two channels of each DTS device (Van de Giesen et al., 2012).

The start and end of each fiber were linked to two different channels, recording the temperature of the fiber by alternating every 3 s between the two channels. Each channel was saved individually and combined into a single dataset with a time resolution of 6 s during the data post-processing. The post-processing was carried out using the pyfocs code developed by Lapo and Freundorfer (2020), which employs the matrix inversion method utilizing constant temperature sections wrapped around warm and cold solid-state reference baths (des Tombe et al., 2020). The distributed horizontal wind speed (UFODS)

223 was derived using paired heated and unheated FO cables in vertical FODS arrays,
224 following the method described by van Ramshorst et al. (2020).

225 **2.5 Defining wind regimes**

226 We identified strong and weak wind regimes using the standard deviation of vertical wind
227 velocity (σ_w) derived from three sub-canopy and one above-canopy EC systems. We
228 postulate that a linear correlation between σ_w values above and below the canopy indicates
229 sufficiently strong turbulence to maintain canopy coupling. Conversely, when above-
230 canopy σ_w is insufficient to induce turbulence within the sub-canopy, decoupling occurs.
231 Freundorfer et al. (2019) caution that the observed linear relationship under strong wind
232 conditions may be confounded by the superposition of weak and strong wind regimes.
233 Nevertheless, we opted to use σ_w as the primary indicator rather than friction velocity (u*),
234 as σ_w has been recognized in the literature as a suitable metric for diagnosing canopy
235 decoupling in forests (Acevedo et al., 2009; Thomas et al., 2013) and has been shown to
236 yield similar thresholds to those based on u_* (Stiegler et al., 2023).
237 To define the wind regime, the scatter of σ_w in the above canopy-space was plotted against
238 the sub-canopy for day and night periods (Fig. 2). Time periods with global radiation
239 exceeding 20 Wm^{-2} above the main tree canopy were classified as daytime, while those
240 with lower values were considered night-time. The scatter plot was then divided into bins
241 based on the mean of every 150 points within the scatter plot. The Pettitt (1979) test was
242 employed to detect the weak-wind thresholds for both day and night periods. The final
243 wind regime for the study site was determined based on the times when at least two of the
244 three EC systems at the sub-canopy exhibited similar regimes (Fig. 2). The weak-wind
245 threshold of σ_w was determined to be 0.34 m s^{-1} for both the main and road towers during
246 day and night (Fig. 2a–c).
247

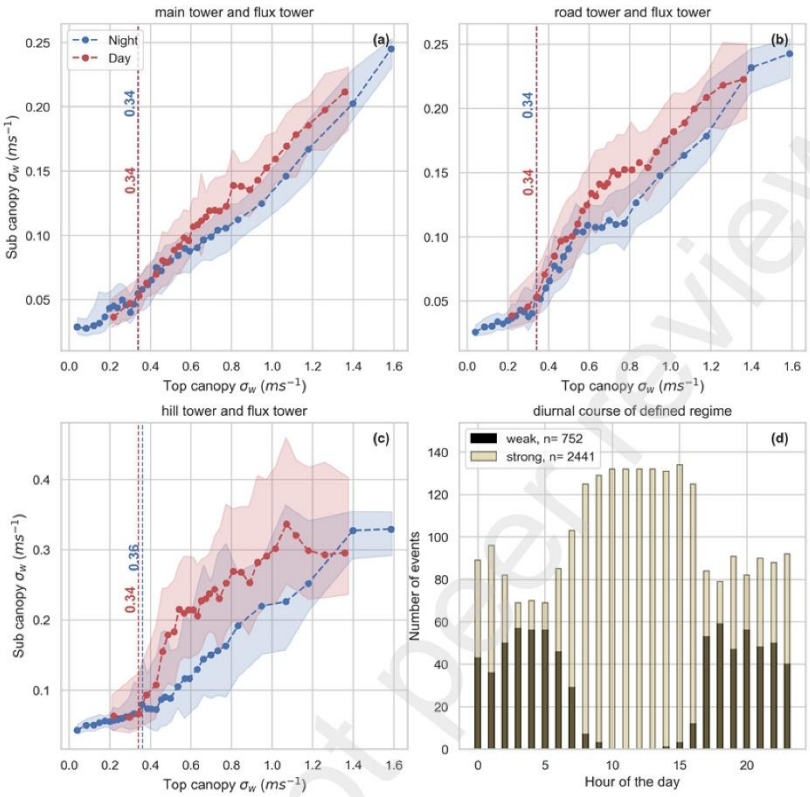

Figure 2. Determining the thresholds of the weak-wind regime using σ_w in the sub-canopy and above-canopy for the main tower (a), road tower (b), and hill tower (c), along with the diurnal course of the defined regime for the entire sub-canopy.

2.6 Random Forest Modeling of Scalar Gas Variability

Random Forest (RF) is an established machine learning method and offers the advantage of capturing complex, non-linear relationships between the target and predictors by utilizing an ensemble of decision trees independently grown on random data subsets. We utilized the RF algorithm (Breiman, 2001) using python package RandomForestRegressor in sklearn (Pedregosa et al., 2011) to determine the importance weighting of the predictor variables outlined in Table 1 which contains a set of micrometeorological variables, turbulence metrics, wind properties, and temperature. The target variables, $\hat{\sigma}_{CO_2}$, $\hat{\sigma}_{CH_4}$, and $\hat{\sigma}_{H_2O}$ were derived from GCSN using horizontal and vertical inlets with 10-minute data as described earlier. Separate models were trained for each tower in the sub-canopy and across

the strong and weak wind regimes resulting in six distinct modeling scenarios. For each scenario, data were randomly split into training (80%) and testing (20%) subsets. Feature scaling was applied independently to training and test sets using StandardScaler and hyperparameter tuning was performed via 10-fold cross-validation using GridSearchCV. To assess the contribution of each predictor, we employed permutation importance, calculated as the mean decrease in model performance (R^2) when individual features were randomly shuffled. Importance scores were averaged over 10 permutations, and standard deviations were computed as uncertainty estimates.

Table 1. The predictor variables used in the RF algorithm were derived from 10-minute interval data collected at four tower locations: the main tower, road tower, hill tower, and flux tower. Vertical wind shear (dU/dz) was calculated as the difference in scalar wind speed between the upper and lower measurement heights, divided by the vertical distance between them. The wind direction shift (Δφ) represents the divergence in wind direction between the sub-canopy and above-canopy layers.

Variable	Unit	Mean±Std main tower	Mean±Std road tower	Mean±Std hill tower	Mean±Std flux tower
Turbulent Kinetic Energy (TKE)	$m^2\ s^{-2}$	-0.01 ± 0.03	0.01 ± 0.03	0.02 ± 0.10	0.08 ± 0.16
Mean vertical wind (w)	$m\ s^{-1}$	0.10 ± 0.05	0.11 ± 0.06	0.17 ± 0.11	0.60 ± 0.33
Std deviation of vertical wind (σ_w)	$m\ s^{-1}$	0.36 ± 0.20	0.37 ± 0.21	0.50 ± 0.30	1.37 ± 0.76
Std deviation of vertical wind ($\sigma_{u,H}$)	$m\ s^{-1}$	0.00 ± 0.01	-0.01 ± 0.01	-0.01 ± 0.02	-0.38 ± 0.40
Momentum flux ($\overline{u'w'}$)	$m^2\ s^{-2}$	0.33 ± 2.00	0.70 ± 4.50	0.88 ± 4.01	0.09 ± 0.91
Stability parameter ($\zeta = z/L$)	-	-0.09 ± 0.04	-0.09 ± 0.04	-0.08 ± 0.04	-0.09 ± 0.04
Wind shear (dU/dz)	s^{-1}	-0.01 ± 0.03	0.01 ± 0.03	0.02 ± 0.10	-
Wind speed (U)	$m\ s^{-1}$	0.76 ± 0.38	0.69 ± 0.34	0.89 ± 0.51	3.23 ± 1.46
φ (Wind direction)	degrees (°)	137 ± 79	133± 83	136± 88	169 ± 74
Wind direction shift (Δφ)	degrees (°)	36 ± 45	38± 41	43± 40	-
Mean air temperature (T)	K	13.96 ± 4.83	14.32 ± 4.75	13.98 ± 4.90	14.26 ± 4.43
Std of air temperature (σ_T)	K	0.15 ± 0.08	0.19 ± 0.11	0.23 ± 0.13	0.25 ± 0.15

2.6 FODS temperature profile classification using k-means

The k-means algorithm is a popular clustering method that divides n observations into k clusters. Each observation is assigned to the cluster whose mean (centroid) is closest to it. The algorithm refines these centroids iteratively and assigns observations to clusters based on their proximity to these centroids (Jain, 2010). In this study, we used the k-means to cluster the FODS temperature profiles for the strong- and weak-wind regimes and assessed the role of thermal stratification on scalar gas spatial variability. The FODS temperature is

converted to potential temperature before feeding into the k-means algorithm. The potential temperature (θ) expressed as:

$$\theta = T_{FODS}\left(\frac{P_0}{P}\right)^k \quad (1)$$

where P is the air pressure in kPa, P0 = 100 kPa is the reference pressure, and k is the Poisson constant assumed to be 2/7. This transformation ensures that the temperature used in the clustering process appropriately reflects the atmospheric conditions by adjusting for pressure effects.

3 Results and discussions

3.1 Forest microclimate during the LOEWE20 experiment

During the LOEWE20 experiment, air temperature ranged from 3.2°C to 26.3°C and median being between 13.7°C to 14.2°C with sub-canopy and above-canopy temperatures exhibiting similar variability (Fig. 3a, and b). The median scalar wind speed (U) was between 0.68 and 0.76 ms-1 in the sub-canopy and 3 ms-1 above the canopy. The hill tower has higher wind speeds and exhibits a different wind speed distribution compared to the other two sub-canopy stations. This is due to its more open canopy structure and its location near the southwestern edge of the forest (Fig. 3c and d). Similar to wind speeds in the sub-canopy, TKE was significantly lower compared to that above the canopy ranging from 0.01 to 6.01 m2s-2 for above canopy and 0.01 to 0.81 m2s-2 for sub-canopy with a median of 0.23 to 0.46 m2s-2 in sub-canopy and 0.96 m2s-2 above-canopy (Fig. 3g, and h).

The dominant wind direction was south-easterly in both the sub-canopy and above-canopy (Fig. 3e and f). In the sub-canopy, the secondary dominant wind direction was from the north and north-east, while in the above-canopy, it was from the west. The observed wind directions are consistent with the prevailing wind directions reported by Thomas and Foken (2007). Based on the weak-wind regime definition in Section 2.5, 76 percent of the data collected during the LOEWE20 experiment were classified as strong-wind conditions, while 24 percent were classified as weak-wind. Additionally, the occurrence of strong winds is primarily confined to the diurnal period, manifesting predominantly between the hours of 09:00 and 16:00. During nocturnal periods, wind conditions exhibit variability, ranging from weak to strong, with weak winds being more prevalent. The periods from

02:00 to 05:00 in the early morning and from 17:00 to 20:00 during the evening transition are characterized by weak-wind conditions (Fig. 3d).

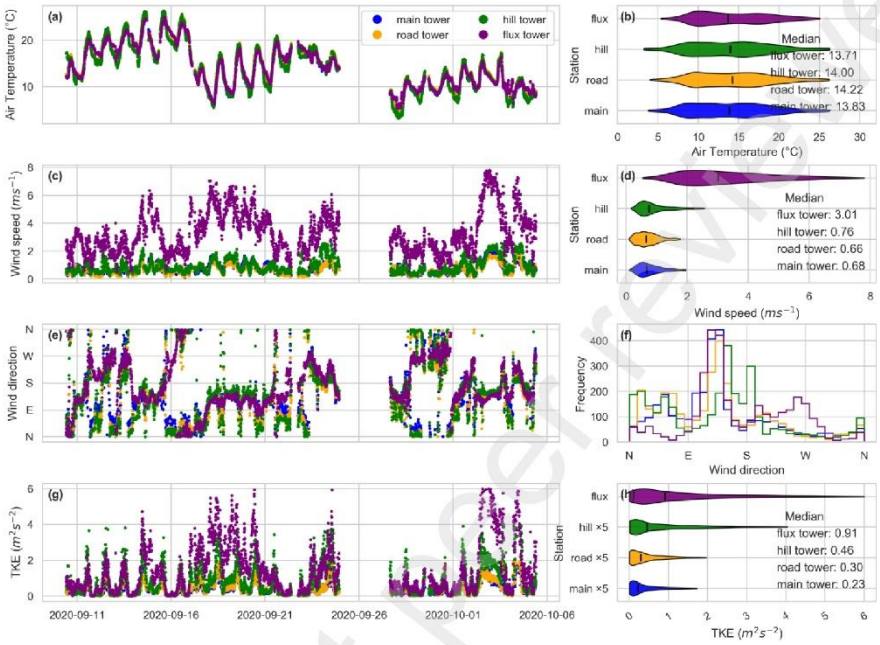

Figure 3. Overview of time series and violin plots of (a, b) air temperature, (c, d) wind speed (g, h) turbulent kinetic energy, and (e, f) time series and histogram of wind direction during the LOEWE20 experiment, representing measurements from the sub-canopy and above-canopy. The flux tower is located above the canopy, while the other three stations are situated within the sub-canopy. In g, and h the TKE in sub-canopy was multiplied by 5 to make the plots more visible.

During strong wind regimes, the polar plots of wind speed at sub-canopy stations indicate that higher wind speeds predominantly originate from the south, southwest, and southeast. In contrast, lower wind speeds are associated with winds coming from the north, northwest, and northeast. A similar distribution pattern is observed at the above-canopy station. Under weak-wind regimes, wind speeds are more evenly distributed across all directions at both sub-canopy and above-canopy levels (Fig. 4a-d). The mean vertical potential temperature profile observed with FODS under strong-wind conditions exhibits a similar structure to that of the full observation period, with a maximum temperature of 14.2 °C occurring at a

height of 22 m. This profile structure is consistent with earlier findings by Raupach (1989) and Schilperoort et al. (2020).

The lower canopy (below 5 m) remains stably stratified in both strong- and weak-wind regimes, with a vertical temperature difference (ΔT) of 0.9 K during strong winds and 2.4 K during weak winds. In contrast, the upper portion of the profile shows increased temperatures, indicating stronger vertical gradients and reduced mixing above the subcanopy (Fig. 4e, and f).

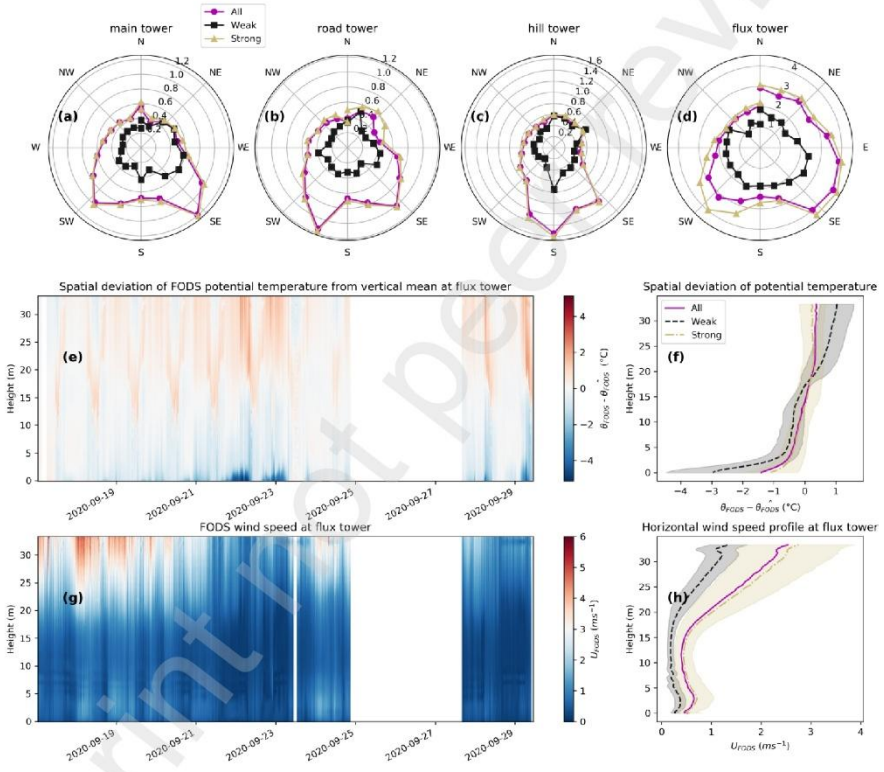

Figure 4. Polar plots of scalar wind speed for the main, road, hill, and flux towers are shown in panels (a–d), separated by weak and strong wind regimes. Panel (e) presents the spatial deviation of FODS-derived temperature time series at the flux tower, while panel (f) displays the corresponding temperature spatial deviation profiles averaged by wind regime. Panel (g) shows the distributed FODS wind speed, calculated following (van Ramshorst et al., 2020), and panel (h) presents the vertical wind speed profiles averaged by wind regimes. All data presented in this graph were 10-minute averages. Shaded areas in f and h show the variability (± Std) of the mean values.

342 The wind speed profiles in both strong- and weak-wind regimes exhibit a pronounced
343 vertical gradient caused by the drag exerted by the forest canopy. Wind speeds are higher
344 above the canopy and decrease sharply within the subcanopy due to momentum absorption
345 by leaves and branches. Notably, the profiles display a local maximum at around 3 m and
346 a minimum at approximately 11 m in both regimes, a pattern consistent with findings from
347 previous studies such as Thomas and Foken (2007) and Rodrigues et al. (2021).

348 **3.2 Sub-canopy scalar gas mixing ratios**

349 At the horizontal inlets CO_2 mixing ratios ranging from 394 to 425 ppm were measured,
350 while vertical inlets recorded a broader range from 394 to 491 ppm, based on the 5th and
351 95th percentiles, respectively. CO_2 mixing ratio indicates a relatively uniform horizontal
352 distribution, in contrast to a vertical gradient with accumulation near the forest floor that
353 decreases with height (Table 2). CO_2 mixing ratios remained consistent over time across
354 both horizontal and vertical inlets, with the exception of inlet S10, located 10 cm agl. S10
355 exhibited persistently higher mixing ratios, driven by soil autotrophic and heterotrophic
356 respiration. These elevated levels were especially prominent during night-time, when
357 weak-wind conditions and stable stratification in the subcanopy suppress turbulence and
358 inhibit vertical mixing (see time series in Appendix Fig. A3a). The diurnal evolution of
359 vertical profiles reinforces this vertical gradient, with CO_2 mixing ratios peaking near the
360 ground and decreasing with height during night-time, then becoming more mixed during
361 daytime. In contrast, the horizontal inlets showed minimal variation in CO_2 mixing ratio
362 across locations, following a consistent diurnal pattern with lowest values occurring around
363 13:00 and highest mixing ratios during the early night-time hours (Fig 5a, b). This build-
364 up results from ecosystem respiration accumulating under weak-wind and stably stratified
365 conditions with suppressed turbulent mixing. As daytime heating initiates the development
366 of a convective turbulent boundary layer, buoyancy-driven turbulence intensifies,
367 generating large eddies that interact with the canopy top. The upper canopy acts as a
368 momentum sink, absorbing energy and producing shear-driven turbulence in the canopy-
369 top shear layer. This turbulence can penetrate downward, especially through canopy gaps
370 or more open understory areas, enhancing vertical mixing within the subcanopy. The
371 resulting increase in turbulent exchange reduces CO_2 accumulation near the ground by

372 facilitating more efficient transport (Raupach et al., 1996; Thomas et al., 2013; Vickers and
373 Thomas, 2014).
374 CH_4 mixing ratios were found to fall within the range of 1891 to 2036 ppb for 5th and 95th
375 percentiles consistent with similar studies like (Song et al., 2024; Sundqvist et al., 2015)
376 showing subtle differences across horizontal inlets and stronger gradient in vertical inlets
377 (Table 2). In contrast to CO_2, the CH_4 mixing ratio at the ground is the lowest among all
378 inlets, which supports the observation of a forest soil as a sink of methane for temperate
379 forests (Dutaur and Verchot, 2007). The main factors influencing methane dynamics in
380 forest ecosystems are soil moisture, soil nutrients such as carbon, nitrate, and phosphorus,
381 and natural disturbances such as drought and fire (Feng et al., 2020). Accordingly, the
382 observed sharp peaks in Fig. A3b mostly occur after precipitation events, displacing the
383 CH_4 in soil pores. The diurnal cycle of the CH_4 mixing ratio peaked during the night-time
384 in both horizontal and vertical inlets (Fig. 5c, and d) when the weak-wind regime
385 dominated and the lowest mixing ratio occurred during the day in the late afternoon similar
386 to the diurnal courses observed in (Botía et al., 2020; Harazono et al., 2015; Querino et al.,
387 2011). The observed increase in CH_4 mixing ratio with height (i.e., lower near the forest
388 floor and higher aloft) implies a positive vertical gradient ($\partial CH_4/\partial z > 0$). According to flux-
389 gradient similarity theory, this corresponds to a downward turbulent flux of CH_4, assuming
390 near-neutral stratification and sufficient turbulence and suggests that the forest floor is a
391 net sink of CH_4 (Borken et al., 2006; Krebs et al., 2024; Ni and Groffman, 2018). The
392 secondary minimum in CH_4 mixing ratios around 05:00 is attributed to wind regime
393 dynamics. During this period, an increased frequency of weak-wind events suppresses the
394 downward transport of CH_4 from above the canopy to lower layers (Fig. 2d). Furthermore,
395 the night-time shift in sub-canopy wind direction—from approximately 135° at 01:00 to
396 105° at 03:00 modifies the source area influencing CH_4 mixing ratios, contributing to the
397 observed minimum.
398 The time series of water vapor mixing ratios from both vertical and horizontal inlets exhibit
399 a consistent fluctuation (Fig. A3c), with values ranging between 8.05 and 17.39 ppth for
400 the 5th and 95th percentiles, respectively (Table 2). The horizontal inlets generally show a
401 homogeneous distribution of H_2O mixing ratios, with the exception of inlets S6, S12, and
402 S13. These inlets are positioned in more open canopy areas, where increased solar radiation

leads to enhanced subcanopy evapotranspiration (ET). The vertical profile shows a negative gradient with decreasing H_2O mixing ratios with height. Similar to the CO_2 mixing ratio patterns, water vapor tends to accumulate near the forest floor due to stable stratification and suppressed turbulent mixing (Table 2).

		CO_2 (ppm)				CH_4 (ppb)				H_2O (ppth)			
Inlets		**p5**	**p50**	**mean**	**p95**	**p5**	**p50**	**mean**	**p95**	**p5**	**p50**	**mean**	**p95**
S1	Horizontal inlets at 4m	395	406	407	422	1924	1986	1982	2034	8.06	12.51	12.27	16.28
S2		394	407	408	425	1925	1987	1983	2035	8.13	12.62	12.34	16.34
S3		395	407	407	421	1926	1986	1983	2035	8.29	12.57	12.33	16.26
S4		395	407	408	422	1925	1987	1983	2036	8.15	12.58	12.32	16.25
S5		395	407	407	422	1924	1986	1982	2034	8.17	12.63	12.36	16.35
S6		395	408	409	425	1924	1985	1982	2035	8.18	12.65	12.40	16.48
S7		395	407	408	422	1925	1986	1982	2034	8.23	12.57	12.35	16.34
S8		395	407	408	425	1924	1985	1982	2035	8.21	12.61	12.36	16.32
S9, 32m	Vertical inlets	394	403	404	418	1928	1989	1985	2036	8.05	12.41	12.13	15.98
S11, 23m		394	404	405	418	1927	1989	1985	2036	8.14	12.47	12.21	16.10
S12, 4m		395	410	410	425	1923	1984	1981	2034	8.37	12.66	12.43	16.51
S13, 2.5		395	410	410	427	1923	1983	1980	2033	8.30	12.65	12.44	16.52
S10, 10 cm		398	426	433	491	1891	1968	1964	2030	8.60	12.93	12.84	17.39

Table 2. Statistics of scalar gas mixing ratios observed with GCSN during the LOEWE20 experiment, the diurnal courses of which is presented in Fig. 5. The values for p5, p50, and p95 represent the 5th percentile, median, and 95th percentile, respectively. Each column is color-coded from blue to red, representing low to high values.

The diurnal variation in H_2O mixing ratio closely follows the patterns of solar radiation and vapor pressure deficit (VPD), consistent with findings by Shen et al. (2015). As solar radiation and air temperature rise from early morning, ET increases, leading to elevated H_2O mixing ratios that typically peak between 10:00 and 12:00. In the afternoon, despite continued increases in temperature, the H_2O mixing ratio declines (Fig. 5e, f), due to intensified turbulent mixing under stronger wind conditions, which enhances vertical transport of water vapor from the sub-canopy. An exception is observed at inlet S10, where a pronounced accumulation of water vapor occurs near the ground in the absence of significant turbulence. This inlet displays a stronger diurnal amplitude compared to others, with its maximum coinciding with a marked reduction in scalar wind speed in the sub-canopy between 16:00 and 17:00. Additionally, delayed soil temperature peaks typically

422 2–4 hours after the air temperature maximum (Ruehr et al., 2010) could contribute to the
423 later peak in forest floor ET by increased evaporation relative to that from upper canopy
424 layers.

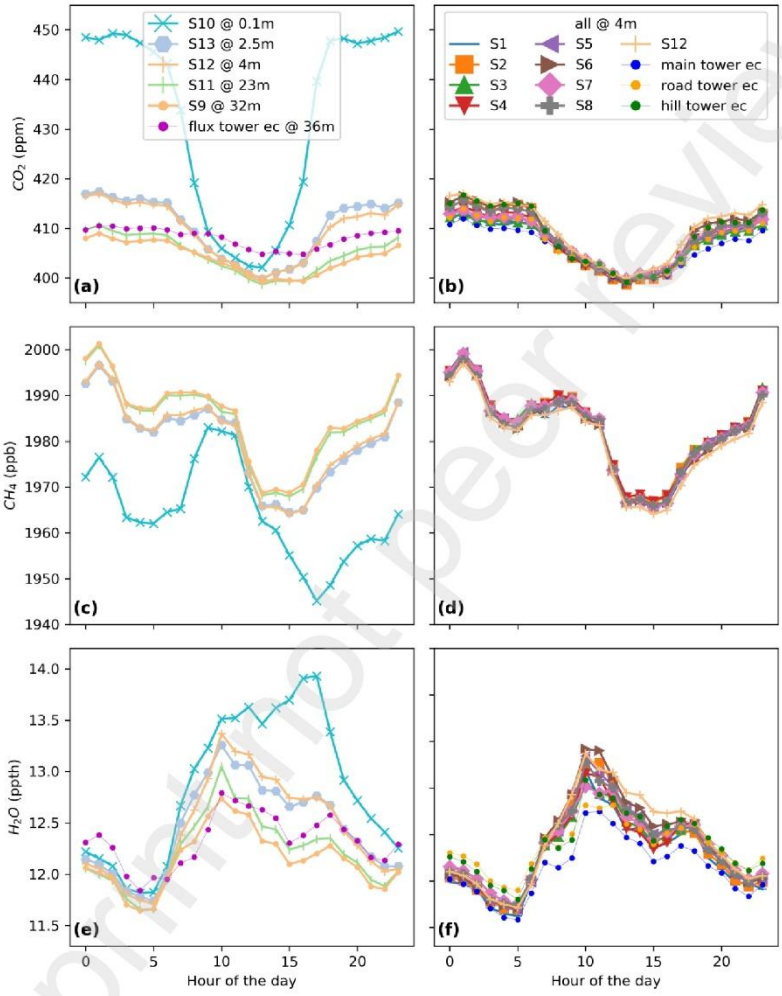

425

426 **Figure 5. Diurnal course of scalar gas mixing ratios in the vertical profile (a, c, and e) and horizontal**
427 **(b, d, and f) including eddy covariance measurements computed based on 10-minute data averaged**
428 **over study period in different hours of the day.**

429

3.3 Spatial variability of scalar gas mixing ratio

As demonstrated in Figure 6a and g, the vertical $\hat{\sigma}_{CO_2}$ displays a greater range in comparison to the horizontal, with a mean of 10.81 and 2.01 ppm, respectively. High vertical $\hat{\boldsymbol{\sigma}}_{\boldsymbol{CO_2}}$ can be attributed to the greater temporal variability in CO_2 vertical profiles, as demonstrated in Fig. 5a. The horizontal $\hat{\sigma}_{CO_2}$is considered to be a consequence of the alteration of wind field and the shuffling of wind direction between different sources, specifically the south-easterly winds in the subcanopy and easterly winds above the canopy. (Fig. A4d, j, p, and v).

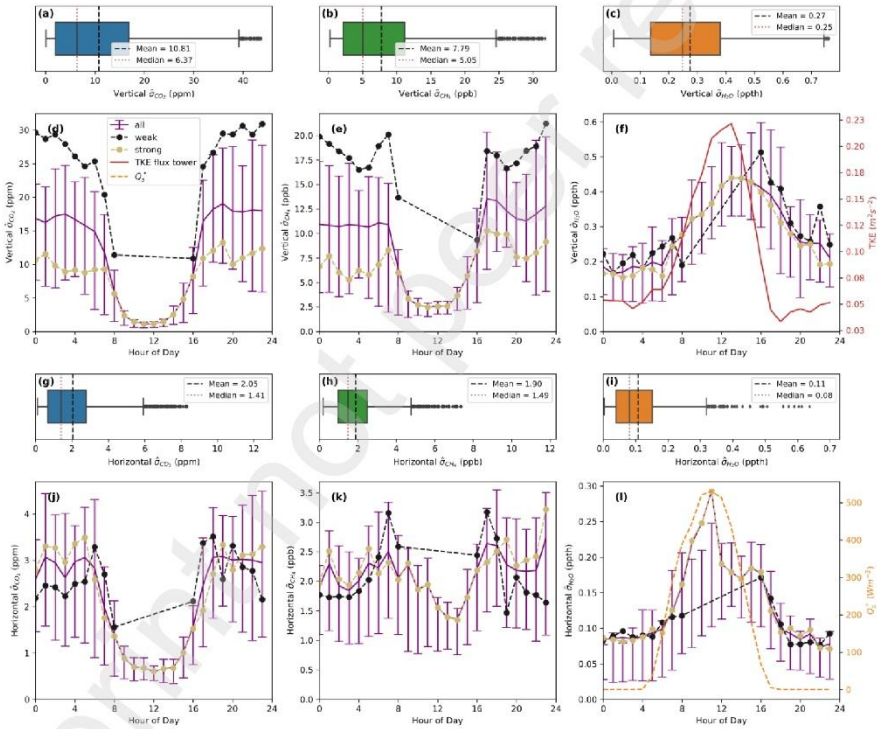

Figure 6. Boxplots of the spatial standard deviations of CO_2, H_2O, and CH_4 mixing ratios ($\hat{\sigma}_{CO_2}$, $\hat{\sigma}_{CH_4}$, and $\hat{\sigma}_{H_2O}$) are shown for the vertical (a–c) and horizontal (g–i) inlets, alongside their respective diurnal cycles in the vertical (d–f) and horizontal (j–l) under weak and strong wind regimes. Error bars in the diurnal plots and width of boxes represent the interquartile range (IQR, 25th to 75th percentiles). The whiskers extend to 1.5 IQR, and outliers beyond this range are plotted individually. Mean and median values are marked as dashed and dotted lines to highlight asymmetries in the distribution. The diurnal course of TKE in flux tower were added to subplot (f) and global radiation (R_g) to subplot (l) for comparison.

The diurnal cycle of $\hat{\sigma}_{CO_2}$exhibits a comparable diurnal pattern to mean CO_2 mixing ratio in both vertical and horizontal inlets. $\hat{\sigma}_{CO_2}$increasing during nocturnal periods and decreasing for daylight conditions, coinciding with the development of a turbulent boundary layer within the forest. It is evident that the wind regime also plays a significant role during nocturnal periods, as evidenced by the increase in $\hat{\sigma}_{CO_2}$during periods of weak-wind and subsequent decrease during periods of strong wind (Fig. 6d). In contrast, the wind regime does not separate the diurnal course of horizontal $\hat{\sigma}_{CO_2}$, with the exception of the morning and evening transition periods, during which $\hat{\sigma}_{CO_2}$ exhibits a maximum.

The mean $\hat{\sigma}_{CH_4}$ across all wind regimes ranges between 1.90 and 7.79 ppb for horizontal and vertical inlets, respectively. A notable peak in the vertical diurnal cycle of $\hat{\sigma}_{CH_4}$is evident during periods of weak wind, specifically for the early morning transition (EMT) and late afternoon transition (LAT) times, as illustrated in Figure 6e. Horizontal $\hat{\sigma}_{CH_4}$shows minor variations, indicating that methane is predominantly well-mixed in the horizontal plane at a depth of 4 metres (Fig. 6k). It is interesting to note that vertical $\hat{\sigma}_{CH_4}$does match the diurnal pattern of CH_4 mixing ratio, but rather is more similar to the diurnal evolution of spatial standard deviations of CO_2. This finding suggests that the vertical spatial variability of CH_4 mixing ratio is driven by mechanical shear in sub-canopy. As illustrated in Figure 6f, the peak of TKE coincidences with minimum $\hat{\sigma}_{CH_4}$. It is evident that, in consideration of the wind direction, during periods of strong wind regimes, the $\hat{\sigma}_{CH_4}$ magnitudes show a lack of sensitivity to wind direction. Conversely, for the weak wind regime, sub-canopy northly and north-easterly winds contribute substantially to $\hat{\sigma}_{CH_4}$.

Similar to $\hat{\sigma}_{CO_2}$and $\hat{\sigma}_{CH_4}$, $\hat{\sigma}_{H_2O}$ exhibits a greater variability in the vertical direction than in the horizontal with mean values of 0.27 and 0.11 ppth, respectively (Fig. 6c and i). It is, however, markedly higher during the daytime and lower at night for both vertical and horizontal inlets. Under weak-wind conditions, vertical inlets show pronounced variability during the evening transition period (Fig. 6f and l). Notably, the horizontal $\hat{\sigma}_{H_2O}$ peaks concurrently with global radiation (Q_s^*), suggesting that spatial heterogeneity in canopy density and differential solar heating of the forest floor and subcanopy vegetation lead to varying ET rates and, consequently, greater variability. In contrast, the vertical $\hat{\sigma}_{H_2O}$ peak

does not coincide with peak of either TKE or Q_s^*. This might be attributed to magnitude of ET which reaches to its diurnal maximum with 2-3 hours later than TKE and Q_s^*.

3.4 Drivers of spatiotemporal variability of greenhouse gases

To investigate the drivers of greenhouse gas variability in the sub-canopy, we consider three groups of potential drivers: statistics of turbulence, the mean flow, and air temperature (Table 1). The scatterplots in Figure A4 illustrate an example of the variation of the chosen micrometeorological variables for vertical $\hat{\sigma}_{CO_2}$ at the hill tower, demonstrating a nonlinear relationship between the micrometeorological variables and vertical $\hat{\sigma}_{CO_2}$. RF model is employed to assess the contribution of each variable to modelling the spatial standard deviation of greenhouse gases.

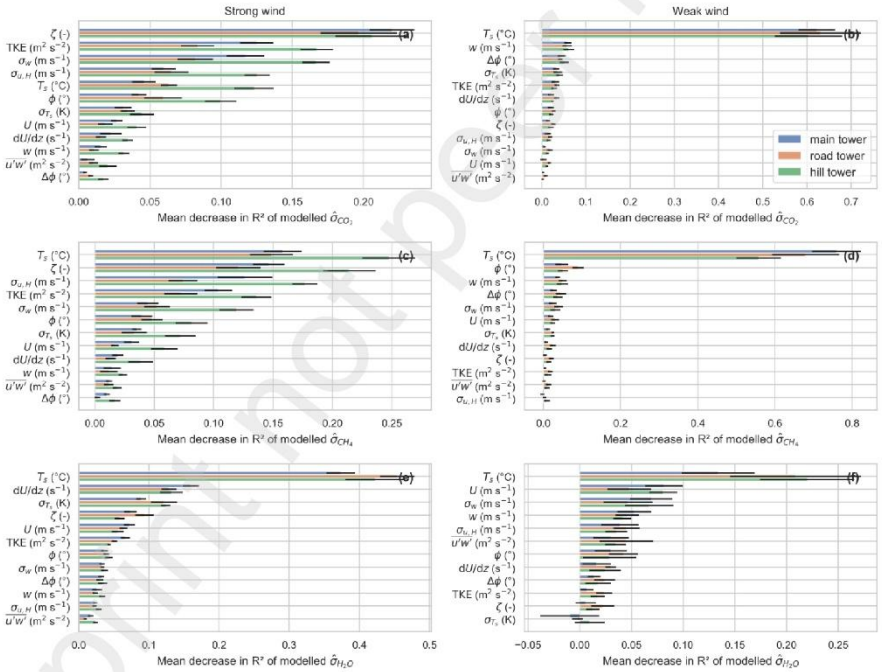

Figure 7. Random forest feature importance of micrometeorological variables in modeling the vertical standard deviation of CO_2, CH_4, and H_2O under strong- and weak-wind regimes at main, road, and hill towers, including vertical wind shear (dU/dz) and wind direction shift (Δφ) derived from sub- and above-canopy stations. The length of each bar represents the mean importance score, indicating the relative contribution of each feature to model performance, while error bars (± Std) reflect variability across 10 permutation repetitions.

493 Permutation feature importance analysis for both vertical and horizontal $\hat{\sigma}_{CO_2}$ under strong-
494 wind regimes reveals that the MOST dynamic stability parameter of sub-canopy (ζ), TKE,
495 and σ_w are the dominant predictors. This indicates that turbulence-driven processes largely
496 govern the variability of $\hat{\sigma}_{CO_2}$ during strong-wind conditions (Figs. 7a and 8a). In contrast,
497 under weak-wind conditions, air temperature driven by absorbed solar radiation emerges
498 as the most influential variable in explaining both vertical and horizontal $\hat{\sigma}_{CO_2}$(Figs. 7b and
499 8b). This underscores the critical role of temperature in modulating mixing processes
500 during weak-wind periods, which frequently occur at night due to radiative cooling and
501 reduced mechanical turbulence. The result is generally consistent with expectations from
502 nocturnal boundary-layer theory, yet it is reassuring to see this pattern quantitatively
503 confirmed by the statistical analyses.
504 For vertical $\hat{\sigma}_{CH_4}$, temperature is also a primary predictor in both wind regimes (Figs. 7c,
505 8c), with turbulence metrics being of secondary importance during strong-wind periods.
506 However, the behavior of horizontal $\hat{\sigma}_{CH_4}$ differs: under strong-wind conditions, its
507 variability is primarily driven by σ_w and vertical wind shear (dU/dz), under weak-wind
508 conditions, the horizontal $\hat{\sigma}_{CH_4}$is best explained by the scalar wind speed (U) (Figs. 8c and
509 8d). Since σ_w is typically influenced by bulk shear (e.g., U) and is not included as a
510 predictor here, it can be argued that during weak-wind conditions, turbulence is not
511 primarily driven by bulk shear but site-dependent non-stationary motions (Mahrt et al.,
512 2015). Furthermore, U and wind direction being important predictors of horizontal $\hat{\sigma}_{CH_4}$,
513 highlight the influence of horizontal advection processes within the subcanopy.
514 It is important to note that other potential drivers—such as soil moisture and soil
515 temperature—can significantly influence CH_4 fluxes in forest sub-canopy (Krebs et al.,
516 2024). These factors may contribute to the spatial variability of CH_4 mixing ratios; however,
517 the temperature variation in September and October is relatively small compared to
518 midsummer and is therefore expected to have only a minimal effect on the explanatory
519 power of the models for CH_4 dynamics.
520 Figures 7e, f and 8e, f demonstrate the dominant role of temperature in explaining the
521 variability of $\hat{\sigma}_{H_2O}$ across wind regimes and both vertical and horizontal directions. For
522 horizontal $\hat{\sigma}_{H_2O}$, temperature remains the most important variable, reinforcing observations

discussed in Section 3.4. There, we attributed spatial variability in ET to heterogeneity in sub-canopy radiation caused by variable canopy cover, which results in ground-level temperature differences. These differences affect ET rates and thus horizontal variability in H_2O mixing ratio. However, such spatial heterogeneity cannot explain vertical $\hat{\sigma}_{H_2O}$ variability, as vertical sampling inlets are collocated on a single tower. In this case, the importance of temperature reflects its direct control over ET processes across vertical canopy layers, each with different available energy. For instance, the available energy at the ground differs substantially from that of the canopy crown, leading to variability in canopy crown transpiration. Furthermore, coherent structures, the primary mechanism driving canopy transport, can also influence the variability of greenhouse gas concentrations within the canopy (Thomas and Foken, 2007b).

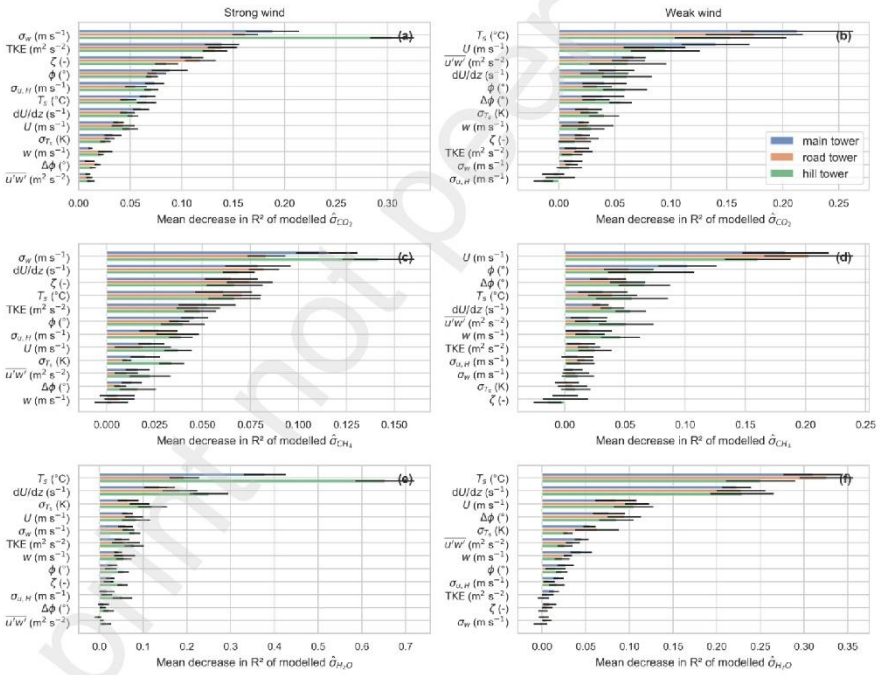

Figure 8. Random forest feature importance of micrometeorological variables in modeling the horizontal standard deviation of CO_2, CH_4, and H_2O under strong- and weak-wind regimes at main, road, and hill towers, based on input features including vertical wind shear (dU/dz) and stability index (Δφ) derived from sub- and above-canopy stations. The length of each bar represents the mean importance score, indicating the relative contribution of each feature to model performance, while error bars (± Std) reflect variability across 10 permutation repetitions.

3.5 Comparing FODS temperature profiles to spatiotemporal variability of greenhouse gases

The vertical profile of FODS potential temperature at the flux tower was used to analyse the role of thermal stratification in the forest canopy on scalar gas mixing, as the temperature profile will respond to changes in wind shear induced mixing and solar radiation. These vertical profiles were then fed into the k-means algorithm to cluster the data, resulting in three clusters for each wind regimes, as shown in Figure 10a and b. Each cluster under strong-wind conditions can be described as follows. Cluster 1 predominantly occurs during the daytime on sunny days, when the canopy crown absorbs solar radiation and heats up while the sub-canopy remains relatively cool. This results in a modest warming of the upper understory (at heights between 10–15 m) and the development of unstable stratification within the densest part of the canopy (at heights between 15 and 25 m). Cluster 2 primarily occurs during night-time, driven by radiative cooling of both the canopy and forest floor, leading to stable stratification near the ground and weakly stable conditions at canopy height. Cluster 3 is mainly associated with morning and evening transition periods and is characterized by stable stratification near the ground and near-neutral conditions at canopy height. This regime typically develops under cloudy conditions, which inhibit significant heating of the canopy.

During strong-wind conditions, all three clustered temperature profiles indicate stable stratification near the forest floor with different stability strength. The distribution of event hours for each cluster is shown in Figure10c and d.

The clusters under weak-wind conditions can be described as follows. Cluster 1 is characterized by weaker stable stratification near the ground and above the canopy, with near-neutral conditions around 5 m height. This pattern develops as both the forest floor and canopy cool through longwave radiative loss. Notably, the forest floor is also subject to radiative cooling, as it can partially exchange radiation with the sky through canopy gaps. This stratification pattern predominantly occurs during night-time, including a significant number of events during the evening transition period. Clusters 2 and 3 exhibit very stable stratification within the sub-canopy and stable conditions above the canopy, driven by radiative cooling of both the forest canopy and forest floor. These clusters display a

571 strongly stratified structure compared to the first cluster, with no indication of near-neutral
572 stratification around 5 m height.

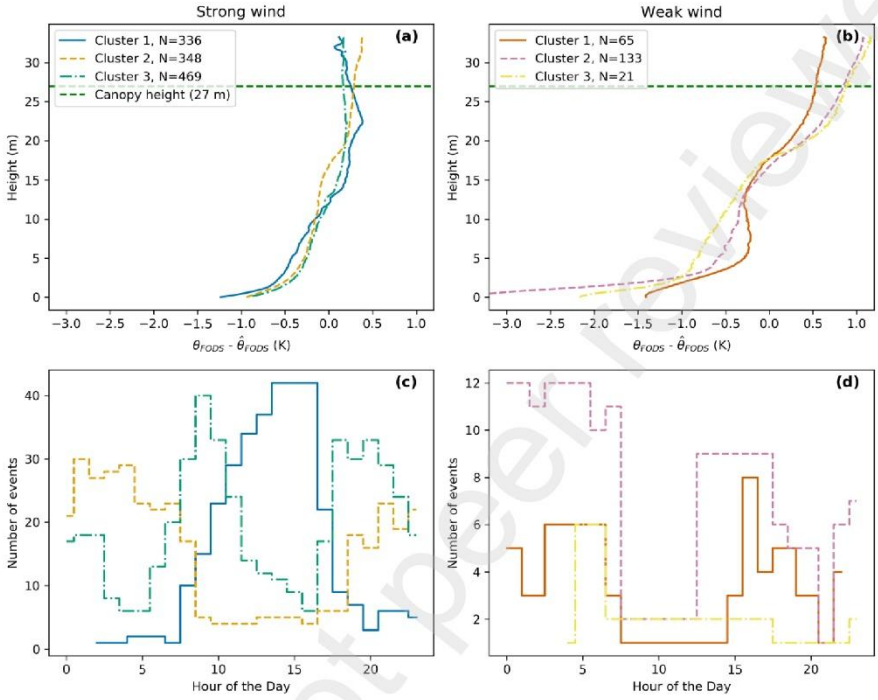

573

574 **Figure 9. Average FODS potential temperature profiles for each cluster, normalized by subtracting**
575 **the spatial mean of each profile within the cluster, under strong- (b) and weak-wind (c) conditions at**
576 **the flux tower. Panel (d) shows the distribution of event hours for each cluster during strong-wind**
577 **conditions, and panel (e) during weak-wind conditions. The canopy height reference is based on.**

578 ### 3.5.1 Horizontal variability of greenhouse gases

579 Cluster 2 in strong-wind conditions is the only cluster that occurs during the night (Fig. 9a
580 and c); hence IQR range of $\hat{\sigma}_{CO_2}$ and $\hat{\sigma}_{CH_4}$ in horizontal inlets are the greatest due to higher
581 mixing ratio of CO_2 and CH_4. The IQR and median of $\hat{\sigma}_{CO_2}$and $\hat{\sigma}_{CH_4}$in the two other clusters
582 decrease with increasing stability strength at the forest floor in horizontal inlets (Fig. 10a
583 and b). Weak-wind conditions, dominated by night-time except cluster 1, which presents
584 calm evening transition periods, where the IQR and median of horizontal spatial standard
585 deviation of greenhouse gases remain high. The variability among different horizontal
586 inlets can be attributed to differences in canopy structure openness, which varies across

inlets and affects the local stratification the lower subcanopy. Additionally, the evening transition period—marked by a sudden drop in TKE, reduced photosynthesis, and accumulation of gases—further contributes to this variability, as the transition does not occur simultaneously across the entire sub-canopy due to spatial heterogeneity in forest structure. The IQR and median for clusters 2 and 3 obey the static stability strength, the more stable, the less spatial variability in horizontal (Fig. 10d and e).

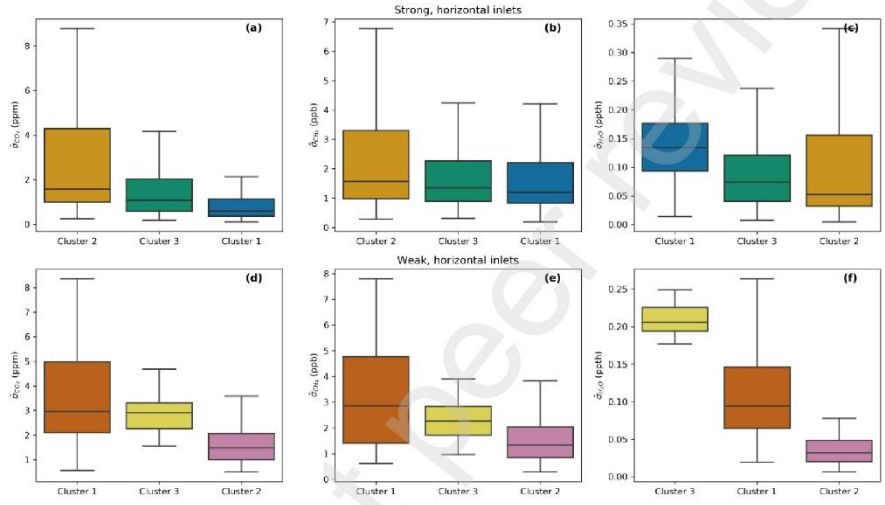

Figure 10. Box plots of the horizontal spatial standard deviation of scalar gas concentrations ($\hat{\sigma}_{CO_2}$, $\hat{\sigma}_{CH_4}$, and $\hat{\sigma}_{H_2O}$) under strong-wind (a, b, c) and weak-wind (d, e, f) regimes. The regimes are defined based on the FODS potential temperature clusters at the main tower, as shown in Fig. 9a and b. Box plot colors correspond to the cluster colors used in Fig. 9. The horizontal line within each box represents the median, and the box plots are ordered by decreasing median values.

During strong-wind regimes, the highest median of horizontal $\hat{\sigma}_{H_2O}$ was observed in Cluster 1, which represents daytime conditions. This can be attributed, first, to high ET rates during sunny periods, enhancing horizontal variability in water vapor. Second, spatial variability in ET across horizontal inlets is driven by variability in solar radiation reaching the forest floor and horizontal differences, in vegetation structure contributes to this pattern (see Fig. 9c and Fig. 10c). The variability of the vegetation structure is evident in the aerial image shown in Fig. 1a, where the southern and northeastern parts of the study area are adjacent to partially open canopy and younger trees. During weak-wind regimes, the horizontal variability of H_2O is highest in Cluster 1, which is the only cluster that includes

daytime period particularly the evening transition when ET is still substantial. This variability is further enhanced by spatial heterogeneity in ET, driven by sub-canopy structural differences and uneven radiation distribution across the forest sub-canopy. Under strongly stable stratification, mixing processes are largely suppressed together with absence of ET during the night time, resulting in minimal variability in H_2O mixing ratio (Fig. 10f).

3.5.2 Vertical variability of greenhouse gases

The vertical variability of $\hat{\sigma}_{CO_2}$and $\hat{\sigma}_{H_{20}}$ under strong-wind conditions scales with the static stability of the upper canopy (above 15 m). Cluster 1, characterized by unstable stratification, shows the lowest variability, whereas Cluster 2, with stable stratification, exhibits the highest variability. Cluster 3, with near-neutral conditions, lies in between (Fig. 11a, b).

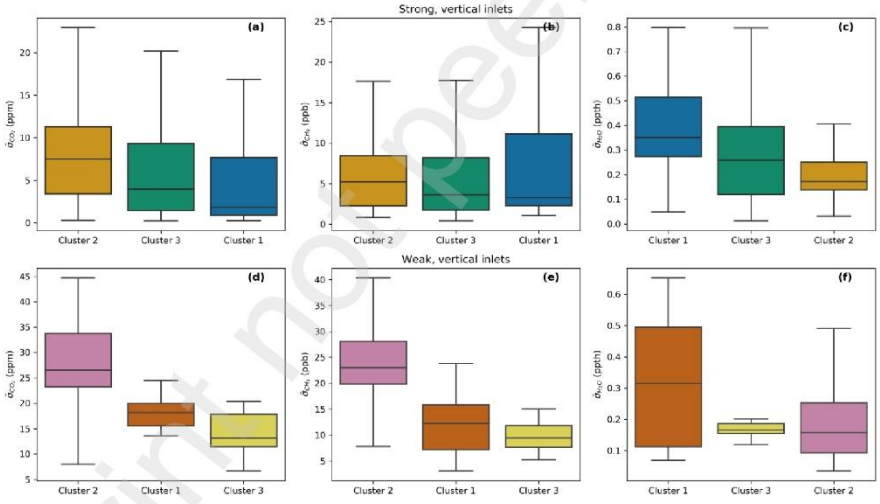

Figure 11. Box plots of the vertical spatial standard deviation of scalar gas concentrations ($\hat{\sigma}_{CO_2}$, $\hat{\sigma}_{CH_4}$, and $\hat{\sigma}_{H_{20}}$) under strong-wind (a, b, c) and weak-wind (d, e, f) regimes. The regimes are defined based on the FODS potential temperature clusters at the main tower, as shown in Fig. 10a and b. Box plot colors correspond to the cluster colors used in Fig. 10. The horizontal line within each box represents the median, and the box plots are ordered by decreasing median values.

Under weak-wind conditions, Cluster 2 displays the largest IQR and median values due to very stable stratification near the ground, which suppresses mixing and leads to vertical separation of ground-emitted gases. In contrast, Cluster 1, with weaker stability near the

ground and within the canopy, shows reduced IQR and median. For H_2O under strong-wind conditions, vertical variability is greatest in Cluster 1 (daytime), driven by both variability in energy and TKE, and by vertical differences in ET sources: the ground and canopy contribute significantly, while the mid-canopy adds little (Fig. 11c). During weak-wind conditions, H_2O variability is also highest in Cluster 1, which includes daytime especially the evening transition period. During this time, ET remains substantial, and near-neutral stratification in the subcanopy allows mixing between lower and upper layers, enhancing vertical spatial variability (Fig. 11f).

It can be argued that the spatial variability of CO_2 and CH_4, both horizontally and vertically, can largely be explained by the potential temperature profile alone, which integrates the effects of TKE and radiative processes into the resulting thermal stratification. In this framework, unstable or near-neutral profiles increase mixing and reduce scalar variability, while stable stratification especially near the ground or within the canopy suppresses mixing and enhances spatial gradients. For horizontal variability in CO_2 and CH_4, additional factors such as forest structural heterogeneity and local differences in leaf area index (LAI) further modulate stratification patterns and the degree of gas accumulation or dispersion across inlets. However, H_2O variability deviates from this pattern due to the fundamentally different nature of its source ET, which is tightly coupled to solar radiation, plant physiology, and surface moisture availability. Since ET occurs primarily during the daytime and can vary strongly with both vertical (ground vs. canopy crown) and horizontal heterogeneity (e.g., gaps, undergrowth), potential temperature alone is insufficient to explain H_2O variability. Instead, H_2O variability reflects a complex interplay between energy availability, ET dynamics, and local canopy structure, particularly during transitional periods when residual ET continues under weakly stratified conditions.

4 Conclusions

Our analysis of scalar gas measurements in the forest sub-canopy revealed distinct vertical and horizontal variabilities for CO_2, CH_4, and H_2O mixing ratios, shaped by the interplay between biological processes and micrometeorological conditions. CO_2 showed strong vertical gradients, driven by nocturnal accumulation from respiration near the ground under stable stratification and weak turbulence, while CH_4 exhibited an inverse gradient,

consistent with soil uptake. H_2O mixing ratios also followed a vertical structure, with accumulation near the forest floor and diurnal patterns aligned with ET dynamics. Horizontal variations were notably smaller for all scalars, reflecting the homogeneous lateral distribution at 4 m height, except in areas with more open canopy, which altered the local radiation and ET balance. Diurnal and spatial variability of greenhouse gases were closely tied to wind regime and turbulence intensity: weak-wind regime enhanced vertical heterogeneity, while convective daytime turbulence led to more uniform mixing. Spatial standard deviations of scalar mixing ratios were generally higher in the vertical than the horizontal dimension. Notably, $\hat{\sigma}_{CO_2}$ and $\hat{\sigma}_{CH_4}$ were highest under weak-wind conditions, while $\hat{\sigma}_{H_2O}$ peaked during the day, correlating with radiation-driven ET heterogeneity. These findings underscore the importance of capturing fine-scale spatiotemporal variability and understanding the micrometeorological drivers that govern scalar transport in complex forest environments. They also highlight the utility of dense sensor networks like GCSN for advancing process-level understanding and improving model parameterizations of trace gas exchange in forest ecosystems.

The RF analysis reveals that scalar gas variability in the forest sub-canopy is governed by turbulence under strong winds and by temperature under weak winds. CO_2 variability is driven mainly by TKE, σ_w, and stability during turbulent conditions, while temperature dominates when weak-wind regime dominates. For CH_4, temperature is consistently important, with wind shear contributing under strong winds and advection (wind speed and direction) under weak winds. H_2O variability is strongly linked to temperature across all conditions, reflecting ET dynamics and energy gradients.

The analysis of FODS-derived potential temperature profiles highlights thermal stratification as a key driver of scalar gas variability, especially under weak-wind conditions. K-means clustering revealed distinct stratification regimes, with strong-wind periods marked by unstable profiles that enhance mixing, and weak-wind conditions dominated by stable layers that suppress turbulence, particularly near the forest floor and canopy top. This stratification strongly shapes the spatial variability of CO_2 and CH_4: unstable or near-neutral profiles enhance mixing and reduce variability, while stable conditions increase scalar accumulation and spatial gradients. The potential temperature profile thus effectively integrates the influence of both turbulence and radiative processes

on scalar dispersion. For horizontal variability, structural heterogeneity and differences in LAI further modulate gas transport by shaping local stratification and mixing conditions. However, H_2O variability follows a distinct pattern due to its ET-driven source, which is tightly linked to daytime energy input and plant physiological responses. Unlike CO_2 and CH_4, H_2O variability cannot be fully explained by thermal stratification alone; instead, it reflects a complex interaction of radiation, soil moisture, and canopy structure particularly during transition periods when residual ET persists under weakly stratified conditions.

These insights into the drivers of scalar gas variability have practical implications beyond process-level understanding. By resolving fine-scale spatiotemporal patterns, our results can inform forest management strategies aimed at optimizing carbon sequestration and maintaining ecosystem health. They also provide valuable constraints for improving terrestrial greenhouse gas budgets and modeling trace gas exchange under different micrometeorological regimes, which is relevant for climate protection and mitigation efforts. Finally, the study demonstrates the utility of high-resolution sensor networks and combined observational–statistical approaches for capturing the complexity of forest-atmosphere interactions, which could benefit researchers and practitioners seeking to better quantify and predict ecosystem-scale gas fluxes.

Author contributions

Conceptualization: MA, CKT; methodology and manufacturing: MA, CKT; field data collection: MA, KL; data validation: MA, KL; data analysis: MA; investigation: MA; data curation: MA; writing – original draft preparation: MA; writing – review and editing: all authors; visualization: MA; funding acquisition: CKT. All authors have read and agreed to the published version of the paper.

Competing interests

The contact author has declared that none of the authors has any competing interests.

Data availability

The dataset is available on Zenodo: to be added in final version.

Acknowledgements

This research was supported by the European Research Council (ERC) under the Horizon 2020 programme (DarkMix, grant no. 724629). We gratefully acknowledge Elena Nitzler for her involvement in the scalar gas measurement campaign. We also thank Johann Schneider and Johannes Olesch for their valuable assistance with fieldwork and technical support.

Appendix A

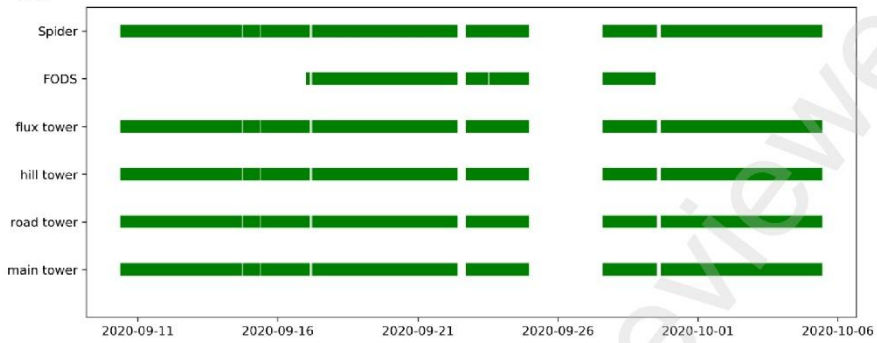

Figure A1. Data availability of LOEWE20 experiment

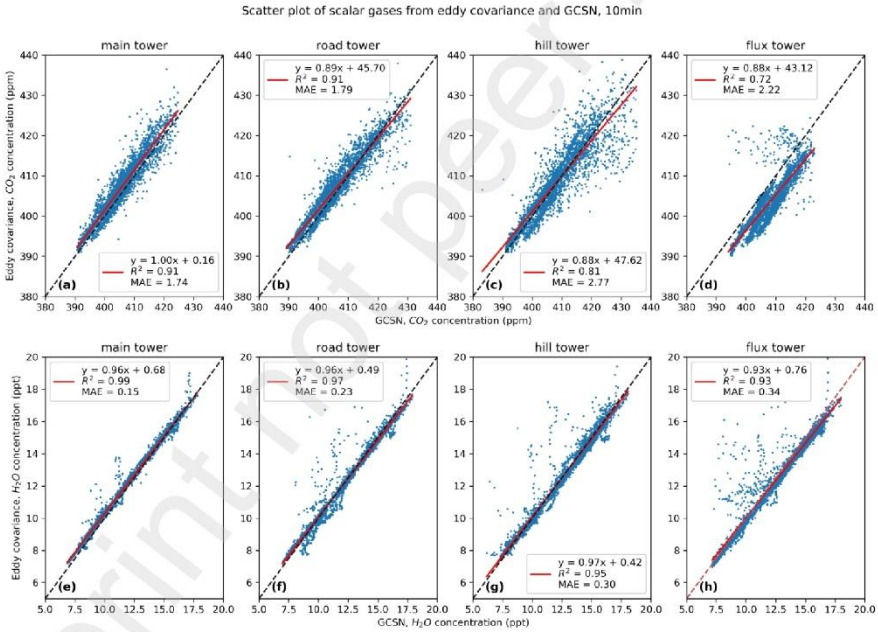

Figure A2. Comparison between the scalar gas mixing ratio of close path gas analyser and EC. The inlet 7 used to be compared with EC tower at main tower EC (a, e), the inlet S8 used in road tower EC (b,f), the inlet 6 used for hill tower EC (c,g), and the inlet 9 used to be compared with flux tower EC.

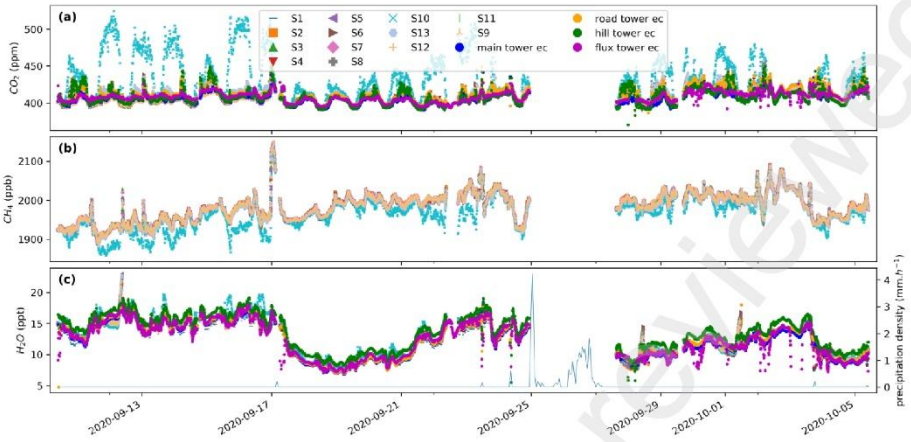

751

752 **Figure A3. (a) CO_2, (b) CH_4, and (c) H_2O mixing ratio and precipitation during LOEWE20 experiment.**
753 **ppth stand for part per thousand, ppm for part per million, and ppb for part per billion.**

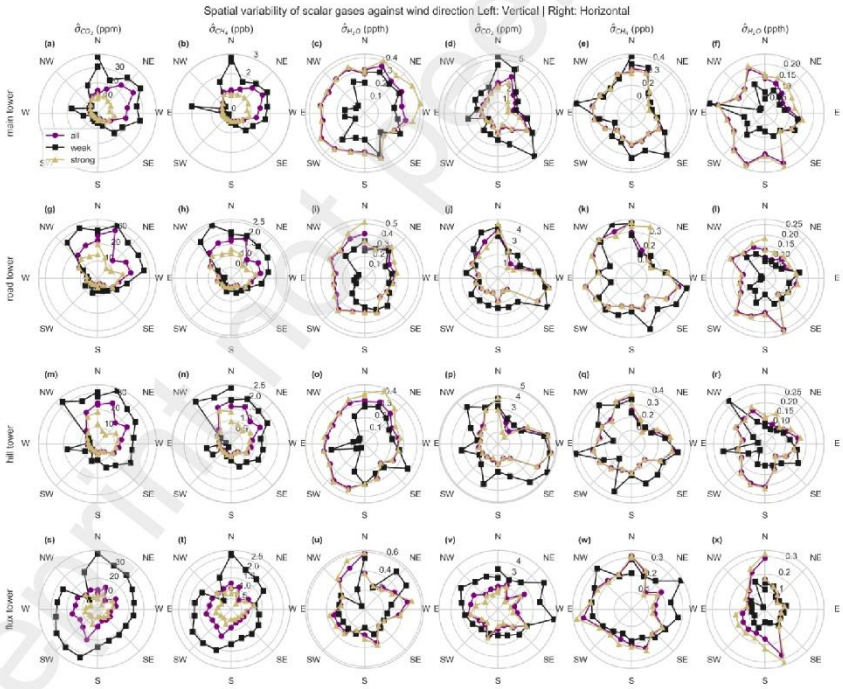

754

755 **Figure A 4. Wind direction dependence of spatial variability in CO_2, CH_4, and H_2O mixing ratios in**
756 **sub-canopy (first three rows), and above canopy (last row) in vertical (left) and horizontal (right)**
757 **directions.**

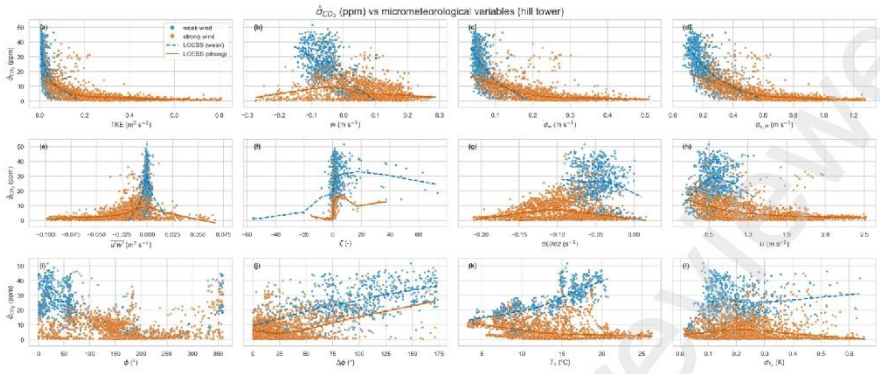

Figure A5. Variation of micrometeorological variables with vertical vertical $\hat{\sigma}_{CO_2}$ at the hill tower under weak- and strong-wind regimes, with regime-specific Locally Estimated Scatterplot Smoothing (LOESS) fits.

References

Acevedo, O.C., Moraes, O.L., Degrazia, G.A., Fitzjarrald, D.R., Manzi, A.O., Campos, J.G., 2009. Is friction velocity the most appropriate scale for correcting nocturnal carbon dioxide fluxes? Agric. For. Meteorol. 149, 1–10.

Arcomano, T., Szunyogh, I., Pathak, J., Wikner, A., Hunt, B.R., Ott, E., 2020. A machine learning-based global atmospheric forecast model. Geophys. Res. Lett. 47, e2020GL087776.

Belcher, S., Finnigan, J., Harman, I., 2008. Flows through forest canopies in complex terrain. Ecol. Appl. 18, 1436–1453.

Bonan, G.B., 2008. Forests and climate change: forcings, feedbacks, and the climate benefits of forests. science 320, 1444–1449.

Borken, W., Davidson, E.A., Savage, K., Sundquist, E.T., Steudler, P., 2006. Effect of summer throughfall exclusion, summer drought, and winter snow cover on methane fluxes in a temperate forest soil. Soil Biol. Biochem. 38, 1388–1395. https://doi.org/10.1016/j.soilbio.2005.10.011

Botía, S., Gerbig, C., Marshall, J., Lavric, J.V., Walter, D., Pöhlker, C., Holanda, B., Fisch, G., de Araújo, A.C., Sá, M.O., Teixeira, P.R., Resende, A.F., Dias-Junior, C.Q., van Asperen, H., Oliveira, P.S., Stefanello, M., Acevedo, O.C., 2020. Understanding nighttime methane signals at the Amazon Tall Tower Observatory (ATTO). Atmospheric Chem. Phys. 20, 6583–6606. https://doi.org/10.5194/acp-20-6583-2020

Breiman, L., 2001. Random forests. Mach. Learn. 45, 5–32.

des Tombe, B., Schilperoort, B., Bakker, M., 2020. Estimation of Temperature and Associated Uncertainty from Fiber-Optic Raman-Spectrum Distributed Temperature Sensing. Sensors 20, 2235. https://doi.org/10.3390/s20082235

Dupont, S., Irvine, M.R., Bonnefond, J.-M., Lamaud, E., Brunet, Y., 2012. Turbulent structures in a pine forest with a deep and sparse trunk space: stand and edge regions. Bound.-Layer Meteorol. 143, 309–336.

Dutaur, L., Verchot, L.V., 2007. A global inventory of the soil CH4 sink. Glob. Biogeochem. Cycles 21. https://doi.org/10.1029/2006GB002734

Feigenwinter, C., Mölder, M., Lindroth, A., Aubinet, M., 2010. Spatiotemporal evolution of CO2 concentration, temperature, and wind field during stable nights at the Norunda forest site. Agric. For. Meteorol. 150, 692–701.

Feng, H., Guo, J., Han, M., Wang, W., Peng, C., Jin, J., Song, X., Yu, S., 2020. A review of the mechanisms and controlling factors of methane dynamics in forest ecosystems. For. Ecol. Manag. 455, 117702.

Foken, T., 2017. Energy and Matter Fluxes of a Spruce Forest Ecosystem. Springer.

Freundorfer, A., Lapo, K., Schneider, J., Thomas, C.K., 2021. Distributed Sensing of Wind Direction Using Fiber-Optic Cables. https://doi.org/10.1175/JTECH-D-21-0019.1

Freundorfer, A., Rehberg, I., Law, B.E., Thomas, C., 2019. Forest wind regimes and their implications on cross-canopy coupling. Agric. For. Meteorol. 279, 107696.

Girach, I.A., Ponmalar, M., Murugan, S., Rahman, P.A., Babu, S.S., Ramachandran, R., 2022. Applicability of Machine Learning Model to Simulate Atmospheric CO_2 Variability. IEEE Trans. Geosci. Remote Sens. 60, 1–6.

Harazono, Y., Iwata, H., Sakabe, A., Ueyama, M., Takahashi, K., Nagano, H., Nakai, T., Kosugi, Y., 2015. Effects of water vapor dilution on trace gas flux, and practical correction methods. J. Agric. Meteorol. 71, 65–76. https://doi.org/10.2480/agrmet.D-14-00003

Jain, A.K., 2010. Data clustering: 50 years beyond K-means. Pattern Recognit. Lett. 31, 651–666.

Kanani-Sühring, F., Raasch, S., 2015. Spatial variability of scalar concentrations and fluxes downstream of a clearing-to-forest transition: a large-eddy simulation study. Bound.-Layer Meteorol. 155, 1–27.

Krebs, L., Burri, S., Feigenwinter, I., Gharun, M., Meier, P., Buchmann, N., 2024. Forest-floor respiration, N2O fluxes, and CH4 fluxes in a subalpine spruce forest: drivers and annual budgets. Biogeosciences 21, 2005–2028. https://doi.org/10.5194/bg-21-2005-2024

Lapo, K., Freundorfer, A., 2020. Klapo/Pyfocs v0. 5. Zenodo Genève Switz.

Liang, J., Zhang, L., Wang, Y., Cao, X., Zhang, Q., Wang, H., Zhang, B., 2014. Turbulence regimes and the validity of similarity theory in the stable boundary layer over complex terrain of the Loess Plateau, China. J. Geophys. Res. Atmospheres 119, 6009–6021. https://doi.org/10.1002/2014JD021510

Mahrt, L., Sun, J., Stauffer, D., 2015. Dependence of Turbulent Velocities on Wind Speed and Stratification. Bound.-Layer Meteorol. 155, 55–71. https://doi.org/10.1007/s10546-014-9992-5

Ni, X., Groffman, P.M., 2018. Declines in methane uptake in forest soils. Proc. Natl. Acad. Sci. 115, 8587–8590. https://doi.org/10.1073/pnas.1807377115

Oliveira, P.E., Acevedo, O.C., Sörgel, M., Tsokankunku, A., Wolff, S., Araújo, A.C., Souza, R.A., Sá, M.O., Manzi, A.O., Andreae, M.O., 2018. Nighttime wind and scalar variability within and above an Amazonian canopy. Atmospheric Chem. Phys. 18, 3083–3099.

Pedregosa, F., Varoquaux, G., Gramfort, A., Michel, V., Thirion, B., Grisel, O., Blondel, M., Prettenhofer, P., Weiss, R., Dubourg, V., others, 2011. Scikit-learn: Machine learning in Python. J. Mach. Learn. Res. 12, 2825–2830.

Pettitt, A.N., 1979. A non-parametric approach to the change-point problem. J. R. Stat. Soc. Ser. C Appl. Stat. 28, 126–135.

Querino, C. a. S., Smeets, C.J.P.P., Vigano, I., Holzinger, R., Moura, V., Gatti, L.V., Martinewski, A., Manzi, A.O., de Araújo, A.C., Röckmann, T., 2011. Methane flux, vertical gradient and mixing ratio measurements in a tropical forest. Atmospheric Chem. Phys. 11, 7943–7953. https://doi.org/10.5194/acp-11-7943-2011

Raupach, M.R., 1989. Applying Lagrangian fluid mechanics to infer scalar source distributions from concentration profiles in plant canopies. Agric. For. Meteorol., Biometeorology 47, 85–108. https://doi.org/10.1016/0168-1923(89)90089-0

Raupach, M.R., Finnigan, J.J., Brunet, Y., 1996. Coherent Eddies and Turbulence in Vegetation Canopies: The Mixing-Layer Analogy, in: Garratt, J.R., Taylor, P.A. (Eds.), Boundary-Layer Meteorology 25th Anniversary Volume, 1970–1995: Invited Reviews and Selected Contributions to Recognise Ted Munn's Contribution as Editor over the Past 25 Years. Springer Netherlands, Dordrecht, pp. 351–382. https://doi.org/10.1007/978-94-017-0944-6_15

Rodrigues, A., Sardinha, R.A., Pita, G., 2021. Aerodynamic Characterization of the Surface Layer, in: Rodrigues, A., Sardinha, R.A., Pita, G. (Eds.), Fundamental Principles of Environmental Physics. Springer International Publishing, Cham, pp. 13–32. https://doi.org/10.1007/978-3-030-69025-0_2

Ruehr, N.K., Knohl, A., Buchmann, N., 2010. Environmental variables controlling soil respiration on diurnal, seasonal and annual time-scales in a mixed mountain forest in Switzerland. Biogeochemistry 98, 153–170. https://doi.org/10.1007/s10533-009-9383-z

Schilperoort, B., Coenders-Gerrits, M., Jiménez Rodríguez, C., van der Tol, C., Van De Wiel, B., Savenije, H., 2020. Decoupling of a Douglas fir canopy: a look into the subcanopy with continuous vertical temperature profiles. Biogeosciences Discuss. 2020, 1–25.

Serafimovich, A., Thomas, C., Foken, T., 2011. Vertical and horizontal transport of energy and matter by coherent motions in a tall spruce canopy. Bound.-Layer Meteorol. 140, 429–451.

Shen, Q., Gao, G., Fu, B., Lü, Y., 2015. Responses of shelterbelt stand transpiration to drought and groundwater variations in an arid inland river basin of Northwest China. J. Hydrol. 531, 738–748. https://doi.org/10.1016/j.jhydrol.2015.10.053

Song, J., Gkatzelis, G.I., Tillmann, R., Brüggemann, N., Leisner, T., Saathoff, H., 2024. Characterization of biogenic volatile organic compounds and their oxidation products in a stressed spruce-dominated forest close to a biogas power plant. Atmospheric Chem. Phys. 24, 13199–13217. https://doi.org/10.5194/acp-24-13199-2024

Stiegler, C., June, T., Markwitz, C., Camarretta, N., Ali, A.A., Knohl, A., 2023. Wind regimes above and below a dense oil palm canopy: Detection of decoupling and its implications on CO2 flux estimates. Agric. For. Meteorol. 341, 109668. https://doi.org/10.1016/j.agrformet.2023.109668

881 Sun, J., Mahrt, L., Banta, R.M., Pichugina, Y.L., 2012. Turbulence regimes and
882 turbulence intermittency in the stable boundary layer during CASES-99. J Atmos
883 Sci 69, 338–351.
884 Sundqvist, E., Mölder, M., Crill, P., Kljun, N., Lindroth, A., 2015. Methane exchange in
885 a boreal forest estimated by gradient method. Tellus B Chem. Phys. Meteorol. 67.
886 https://doi.org/10.3402/tellusb.v67.26688
887 Thomas, C., Foken, T., 2007a. Organised Motion in a Tall Spruce Canopy: Temporal
888 Scales, Structure Spacing and Terrain Effects. Bound.-Layer Meteorol. 122, 123–
889 147. https://doi.org/10.1007/s10546-006-9087-z
890 Thomas, C., Foken, T., 2007b. Flux contribution of coherent structures and its
891 implications for the exchange of energy and matter in a tall spruce canopy.
892 Bound.-Layer Meteorol. 123, 317–337.
893 Thomas, C.K., 2011. Variability of sub-canopy flow, temperature, and horizontal
894 advection in moderately complex terrain. Bound.-Layer Meteorol. 139, 61–81.
895 Thomas, C.K., Huss, J.-M., Abdoli, M., Huttarsch, T., Schneider, J., 2022. Solid-Phase
896 Reference Baths for Fiber-Optic Distributed Sensing. Sensors 22, 4244.
897 Thomas, C.K., Law, B.E., Irvine, J., Martin, J.G., Pettijohn, J.C., Davis, K.J., 2009.
898 Seasonal hydrology explains interannual and seasonal variation in carbon and
899 water exchange in a semiarid mature ponderosa pine forest in central Oregon. J.
900 Geophys. Res. Biogeosciences 114.
901 Thomas, C.K., Martin, J.G., Law, B.E., Davis, K., 2013. Toward biologically meaningful
902 net carbon exchange estimates for tall, dense canopies: Multi-level eddy
903 covariance observations and canopy coupling regimes in a mature Douglas-fir
904 forest in Oregon. Agric. For. Meteorol. 173, 14–27.
905 Van de Giesen, N., Steele-Dunne, S.C., Jansen, J., Hoes, O., Hausner, M.B., Tyler, S.,
906 Selker, J., 2012. Double-ended calibration of fiber-optic Raman spectra
907 distributed temperature sensing data. Sensors 12, 5471–5485.
908 van Ramshorst, J.G.V., Coenders-Gerrits, M., Schilperoort, B., van de Wiel, B.J.H., Izett,
909 J.G., Selker, J.S., Higgins, C.W., Savenije, H.H.G., van de Giesen, N.C., 2020.
910 Revisiting wind speed measurements using actively heated fiber optics: a wind
911 tunnel study. Atmospheric Meas. Tech. 13, 5423–5439.
912 https://doi.org/10.5194/amt-13-5423-2020
913 Vickers, D., Thomas, C.K., 2014. Observations of the scale-dependent turbulence and
914 evaluation of the flux–gradient relationship for sensible heat for a closed Douglas-
915 fir canopy in very weak wind conditions. Atmos Chem Phys 14, 9665–9676.
916 Wilson, K.B., Meyers, T.P., 2001. The spatial variability of energy and carbon dioxide
917 fluxes at the floor of a deciduous forest. Bound.-Layer Meteorol. 98, 443–473.
918

Contribution to the Publications

This section specifies my contributions to the publications listed in chapter two.

Paper I: Toward quantifying turbulent vertical airflow and sensible heat flux in tall forest canopies using fiber-optic distributed temperature sensing

Authors: Mohammad Abdoli, Karl Lapo, Johann Schneider, Johannes Olesch, and Christoph K. Thomas
Status: Accepted and published in Atmospheric Measurement Techniques Discussions

Own Contribution: I was responsible for 85% of the data processing, 85% of the data analysis and figure generation, 80% of the result interpretation, and 85% of the manuscript writing.
Johann Schneider and Johannes Olesch supported the installation and maintenance of the experimental setup. Christoph K. Thomas introduced me to the processing of eddy covariance fluxes and contributed substantially to the manuscript revision and deepening of the discussion. Karl Lapo provided support with the processing of the FODS data.

Paper II: Improving turbulent airflow direction measurements for fiber-optic distributed sensing using numerical simulations

Authors: Mohammad Abdoli, Reza Pirkhoshghiyafeh, and Christoph K. Thomas
Status: Accepted and published in Atmospheric Measurement Techniques

Own Contribution: I was responsible for 85% of development of the study concept, 85% of the numerical simulations, 85% of data analysis, and figure preparation, as well as 85% of the manuscript writing and interpretation of results. Reza Pirkhoshghiyafeh supported the implementation of the initial simulation setup and solving the model errors in initial phase. Christoph K. Thomas contributed to the scientific framing, provided detailed feedback on manuscript drafts, and helped refine the discussion.

Paper III: Dynamic stability and canopy structure drive Spatio-Temporal Variability of Greenhouse Gases in the sub-canopy of a Temperate Spruce Forest

Authors: Mohammad Abdoli, Karl Lapo, and Christoph K. Thomas
Status: Submitted to Agricultural and Forest Meteorology (MS No.: AGRFORMET-D-25-02734)
Own Contribution: I was responsible for approximately 80% of the overall work, including co-conceptualization, 90% of the data curation, analysis, visualization, and original draft writing. I also led 80% of the methodological design and investigation efforts. Field data collection and validation were carried out in collaboration with Karl Lapo, who contributed to measurement support and feedback on methodology. Christoph K. Thomas co-developed the conceptual framework and contributed through scientific supervision, methodological refinement, and critical revision of the manuscript. Elena Nitzler supported us during the scalar gas measurement campaign.

(Eidesstattliche) Versicherungen und Erklärungen

(§ 9 Satz 2 Nr. 3 PromO BayNAT)

Hiermit versichere ich eidesstattlich, dass ich die Arbeit selbstständig verfasst und keine anderen als die von mir angegebenen Quellen und Hilfsmittel benutzt habe (vgl. Art. 97 Abs. 1 Satz 8 BayHIG).

(§ 9 Satz 2 Nr. 3 PromO BayNAT)

Hiermit erkläre ich, dass ich die Dissertation nicht bereits zur Erlangung eines akademischen Grades eingereicht habe und dass ich nicht bereits diese oder eine gleichartige Doktorprüfung endgültig nicht bestanden habe.

(§ 9 Satz 2 Nr. 4 PromO BayNAT)

Hiermit erkläre ich, dass ich Hilfe von gewerblichen Promotionsberatern bzw. -vermittlern oder ähnlichen Dienstleistern weder bisher in Anspruch genommen habe noch künftig in Anspruch nehmen werde.

(§ 9 Satz 2 Nr. 7 PromO BayNAT)

Hiermit erkläre ich mein Einverständnis, dass die elektronische Fassung meiner Dissertation unter Wahrung meiner Urheberrechte und des Datenschutzes einer gesonderten Überprüfung unterzogen werden kann.

(§ 9 Satz 2 Nr. 8 PromO BayNAT)

Hiermit erkläre ich mein Einverständnis, dass bei Verdacht wissenschaftlichen Fehlverhaltens Ermittlungen durch universitätsinterne Organe der wissenschaftlichen Selbstkontrolle stattfinden können.

…….
Ort, Datum, Unterschrift